Quantum chemical characterization of the interaction of probe molecules with metal oxide supports and transition metal clusters

Zur Erlangung des akademischen Grades einer

DOKTORIN DER NATURWISSENSCHAFTEN

(Dr. rer. nat.)

von der KIT-Fakultät für Chemie und Biowissenschaften

des Karlsruher Instituts für Technologie (KIT)

genehmigte

DISSERTATION

von

M.Sc. Siddhi Gojare

1. Referentin: Prof Dr. Karin Fink
2. Referent: Prof. Dr. Felix Studt
Tag der mündlichen Prüfung: 07.05.2025

Abstract

Metal-oxide-supported transition metal nanoparticles are important heterogeneous catalysts that are widely used in many industry-relevant chemical reactions and in the removal of toxic gases from automobile exhausts. Compared to nanoparticles, metal nanoclusters and recently developed single-atom catalysts (SAC) have proven in some cases advantageous over nanoparticles due to their characteristic geometric properties and efficient use of transition metals. Moreover, there are still major issues in understanding the factors affecting the catalytic activity of such catalysts like the shape of the nanoclusters, interfacial metal-surface interaction, and the influence of support and its terminations towards the binding of small molecules. The present thesis is a theoretical investigation of these individual components, Pt nanoclusters, metal-oxide surface, and the metal-oxide interface.

The first part of the thesis is devoted to the study of anionic platinum-deuteride clusters ($Pt_nD_{2n}^-$. n=6-13) in the gas phase using density functional theory along with spin-orbit coupling. The results showed that the spin-orbit coupling effects affect the relative stability of the isomers in a small energy range. These isomers are mainly stabilized due to the interaction with the deuterium atoms. Smaller clusters like $Pt_6D_{12}^-$ were mostly amorphous with asymmetric structures. Over an increase in the cluster size until $Pt_{13}D_{26}^-$, the cluster geometry evolved to higher symmetry with higher Pt coordination and a high number of deuterium atoms positioned at Pt-Pt bridges leading to a multi-center bond character.

Whereas the major chemical reactions take place on the surface atoms of the nanoclusters, the metal-oxide support also contributes to the catalytic activity via surface relaxation and consecutive charge transfer to the adsorbates. Thus, the interaction of small probe molecules such as CO and CO_2 with the α-Al_2O_3 surface was analyzed using the embedded cluster model approach. The results showed molecular binding at the water- free surface and weaker interaction with the fully hydroxylated surfaces. Various possible molecular binding modes and their relative stability were studied.

To mimic the Pt SAC system, a single Pt atom was placed on these clusters. The analysis showed a strong Pt binding on the O^{2-} site on a water-free surface along with strong surface deformation while it was weakly bound on a fully hydroxylated surface. The consecutive Pt/Al_2O_3 interaction with the CO molecule was investigated.

The present work contributes to a basic understanding by explicitly studying the individual components to envision their effect on the catalytic activity of the respective catalyst at different levels of theory.

Zusammenfassung

Metalloxid-gestützte Übergangsmetall-Nanopartikel sind wichtige heterogene Katalysatoren, die in vielen industrierelevanten chemischen Reaktionen und bei der Beseitigung von giftigen Gasen aus Autoabgasen weit verbreitet sind. Im Vergleich zu Nanopartikeln haben sich Metall-Nanocluster und kürzlich entwickelte Katalysatoren aus einzelnen Atomen (SACs) aufgrund ihrer charakteristischen geometrischen Eigenschaften und der effizienten Nutzung von Übergangsmetallen in einigen Fällen als vorteilhaft erwiesen. Darüber hinaus gibt es immer noch große Probleme beim Verständnis der Faktoren, die die katalytische Aktivität solcher Katalysatoren beeinflussen, wie z. B. die Form der Nanocluster, die Grenzflächenwechselwirkung zwischen Metall und Oberfläche und der Einfluss des Trägers auf die Adsorption kleiner Moleküle. Die vorliegende Arbeit ist eine theoretische Untersuchung dieser einzelnen Komponenten, der Pt-Nanocluster, der Metalloxid-Oberfläche und der Platin-Metalloxid-Grenzfläche.

Der erste Teil der Arbeit ist der Untersuchung von anionischen, deuterierten Platinclustern ($Pt_nD_{2n}^-$. n=6-13) in der Gasphase unter Verwendung von Dichtefunktionaltheorie mit Rücksicht auf die Spin- Bahn-Kopplung gewidmet. Die Ergebnisse zeigten, dass die Spin-Bahn-Kopplungseffekte die relative Stabilität der Isomere ähnlicher Energie beeinflussen. Diese Cluster werden hauptsächlich durch die Wechselwirkung mit den Deuteriumatomen stabilisiert. Kleinere Cluster wie $Pt_6D_{12}^-$ sind meist amorph mit asymmetrischen Strukturen. Mit zunehmender Clustergröße bis zu $Pt_{13}D_{26}^-$ entwickelt sich die Clustergeometrie zu einer höheren Symmetrie mit höherer Pt-Koordination und einer großen Anzahl von Deuteriumatomen, die an Pt-Pt-Brücken positioniert sind, was zu Mehrzentrenbindungen führt.

Während die wichtigsten chemischen Reaktionen an den Oberflächenatomen der Nanocluster ablaufen, trägt auch der Metalloxidträger durch Oberflächenrelaxation und anschließenden Ladungstransfer auf die Adsorbate zur katalytischen Aktivität bei. Daher wurde die Wechselwirkung von kleinen Sondenmolekülen wie CO und CO_2 mit der α-Al_2O_3- Oberfläche mit einem eingetteten Clustermodell analysiert. Die Ergebnisse zeigten eine molekulare Bindung an der wasserfreien Oberfläche und eine schwächere Wechselwirkung mit vollständig hydroxylierten Oberflächen. Es wurden verschiedene mögliche molekulare Bindungsmodi und ihre relative Stabilität untersucht.

Um das Pt-SAC-System zu imitieren, wurde ein einzelnes Pt-Atom auf diesen Oberflächen platziert. Die Analyse zeigt eine starke Pt-Bindung auf einem O^{2-}-Ion auf einer wasserfreien Oberfläche zusammen mit einer starken Oberflächendeformation, während

es auf einer vollständig hydroxylierten Oberfläche nur schwach gebunden ist. Daraufhin wurde die anschließende Pt/Al_2O_3-Wechselwirkung mit dem CO-Molekül untersucht.

Die vorliegende Arbeit trägt zu einem grundlegenden Verständnis bei, indem die einzelnen Komponenten explizit untersucht werden, um ihre Auswirkungen auf die katalytische Aktivität des jeweiligen Katalysators auf verschiedenen Theorieniveaus zu veranschaulichen.

Contents

Abstract i

Zusammenfassung iii

1. Introduction 1

2. Theoretical background 3
2.1. Basic Quantum Chemistry . . . 3
2.2. Møller Plesset Perturbation Theory . . . 4
2.3. Density functional theory . . . 6
2.3.1. Hohenberg-Kohn theorem . . . 6
2.3.2. Kohn-Sham Approach . . . 6
2.3.3. Exchange-correlation functionals . . . 8
2.4. Density of States . . . 11
2.5. Relativistic two-component method . . . 11
2.6. Embedded cluster method . . . 14
2.7. Nuclear-Independent Chemical Shift (NICS) . . . 16
2.8. Nudged Elastic Band (NEB) method . . . 17

3. Study of anionic platinum clusters in gas phase 21
Introduction . . . 21
Computational details . . . 24
3.1. $Pt_nD_{2n}^-$ clusters . . . 24
3.1.1. $Pt_6D_{12}^-$ clusters . . . 25
3.1.2. $Pt_7D_{14}^-$ clusters . . . 27
3.1.3. $Pt_8D_{16}^-$ clusters . . . 27
3.1.4. $Pt_9D_{18}^-$ clusters . . . 29
3.1.5. $Pt_{10}D_{20}^-$ clusters . . . 30
3.1.6. $Pt_{11}D_{22}^-$ clusters . . . 31
3.1.7. $Pt_{13}D_x^-$, x=24,25,26 clusters . . . 33
3.1.8. Discussion . . . 35
3.1.9. Conclusion . . . 36
3.2. $Pt_{12}D_{24}^-$ clusters . . . 38
3.2.1. Computational details . . . 38
3.2.2. Results and Discussion . . . 38
3.2.3. Conclusion . . . 50

4. Alumina surface **51**
Introduction . . . 51
Computational details . . . 55
4.1. CO adsorption on α-Al_2O_3 surface . . . 57
4.1.1. Experiment . . . 57
4.1.2. Results and discussion . . . 59
4.1.3. Conclusion . . . 71
4.2. CO_2 adsorption on α-Al_2O_3 surface . . . 72
4.2.1. Experiment . . . 72
4.2.2. Computational details . . . 73
4.2.3. Results and Discussion . . . 73
4.2.4. Conclusion . . . 83
4.3. CO adsorption on Pt/α-Al_2O_3 surface . . . 85
4.3.1. Computational details . . . 85
4.3.2. Results and Discussion . . . 85
4.3.3. Conclusion . . . 95

5. Summary and conclusion **96**

A. Appendix **99**
A.1. Appendix for Chapter 3.1 . . . 99
A.2. Appendix for Chapter 3.2 . . . 111

Bibliography **113**

Acronyms and Abbreviations **121**

Permissions to Print **123**

List of Publications **123**

Acknowledgments **125**

Declaration **126**

1. Introduction

Catalysis is an important field of study in chemistry as 85%-90% of industrial processes utilize at least one catalytic step to generate fine chemicals, polymers, in oil refining, and for environmental issues such as the removal of CO from car exhausts [1–3]. The main advantages of using a catalyst are the reduction of the activation energy of a chemical reaction, to enhance the selectivity for a desirable product in the case of a multi-product reaction and to avoid the formation of unwanted by-products. Small metal nanoparticles deposited on a metal-oxide support are an important field of research for the heterogeneous catalyst design with the primary goal of obtaining a well-stabilized system with highly dispersed metal nanoparticles ensuring high catalytic efficiency [1, 2].

Among the various heterogeneous catalysts, Pt metal nanoparticles deposited on Al_2O_3 metal-oxide support are applied widely in industry. Relevant chemical reactions such as the CO oxidation [4, 5], NO oxidation [6], propene hydrogenation [7], alkane hydrogenation, and the treatment of toxic pollutants such as CO_2 emitted from the exhausts of automobiles and industries [8, 9]. One of the challenges in the utilization of noble metals such as Pt is its high price and low availability. Therefore, to tackle the leading high demand, instead of Pt nanoparticles, nanoclusters or single atoms are employed in the catalysts [10, 11]. These nanoclusters and single atoms showcase a large surface area-volume ratio, additional active sites, high catalytic efficiency, and the presence of low-coordinated surface atoms which can facilitate the efficient adsorption of the molecules. On the other hand, aluminum oxide is used as a support in the heterogeneous catalysis because of its characteristic properties, such as good mechanical robustness, high inertness, natural abundance, and presence of the ionic Lewis acid-base sites [12]. It is also known that supports like Al_2O_3 are prone to react with surrounding water via dissociating the H_2O molecule and forming hydroxyl terminations on the surface altering the surface behavior [13]. The presence of Al_2O_3 in the catalyst is not just to anchor the nanoclusters but also to further interact with the adsorbed molecules and nanoclusters via charge transfer and surface reconstruction. This is the key factor affecting the catalytic reactivity of the system [14–16]. However, the overall catalytic efficiency of Pt/Al_2O_3 is seen to be influenced by the degree of dispersion of metal nanoclusters, their morphology, their tendency to aggregate to form bigger nanoparticles [17], and their interaction with both metal support and surface terminations at the interface [18–22]. The metal support interaction (MSI) can also induce the restructuring of the supported metal particles exposing new active sites on the surface for anchoring the adsorbate molecules [23]. Therefore, it is important to study the three components

forming a catalytic system individually, 1) Pt nanoclusters, 2) surface behavior of Al_2O_3, and 3) Pt interaction with the support and later with the adsorbed molecule. However, experimentally determining each factor and its influence on the catalytic yield is quite challenging. Thus, a theoretical investigation is needed to determine all the underlying key factors at the atomic scale. In the following thesis, a quantum chemical analysis of the anionic platinum nanoclusters in the gaseous phase, the surface behavior of α-Al_2O_3 upon adsorption of small probe molecules such as CO and CO_2 and the adsorption of a single Pt atom on α-Al_2O_3 and its interaction with the CO molecule are investigated.

The thesis is organized as follows: Chapter 2 gives an overview of the theoretical background of the quantum chemical methods used for the structure determination of Pt nanoclusters and surface behavior of the α-Al_2O_3. This includes a description of the basics of density functional theory and Møller Plesset perturbation theory (MP2) along with the treatment of relativistic effects and the embedded cluster model. Additional concepts employed for determining the electronic properties of the system are also described.

Chapter 3 focuses on the DFT computations carried out on different cluster sizes of anionic deuterated Pt nanoclusters ($Pt_nD_{2n}^-$ (n=6-13)) in the gas phase. In Chapter 3.1, a study of the structure evolution of Pt nanoclusters ($Pt_nD_{2n}^-$ (n=6-13)) upon deuteration is discussed. By combining the data of DFT calculations with the experimental TIED data, it was possible to assign the geometrical structure of the respective cluster size. The influence of the spin orbit coupling effects on the cluster structures and their stability is also discussed. Chapter 3.2 exclusively describes different factors that can affect the structure and electronic properties of the cuboctahedral cage structure of $Pt_{12}D_{24}^-$. The influence of deuterium adsorption on the surface of the Pt cluster and its interaction with the neighboring Pt atoms on the structure stability is discussed. Finally, the transformation pathway between different isomers is investigated.

In Chapter 4, the surface behavior of an α-Al_2O_3 surface is investigated using an embedded cluster model and DFT. In Chapters 4.1 and 4.2, the interaction of CO and CO_2 as a probe molecule on the α-Al_2O_3 surface is investigated. The surface relaxations and alteration of the electronic properties at the molecule-metal interface depending on the variation in the degree of surface hydroxylations are investigated. The results obtained from the computations are directly compared with the experimental IRRAS data. Chapter 4.3 contains the analysis of single Pt atom adsorption on the α-Al_2O_3 surface depending on the degree of surface hydroxylation. Further insights on the factors that can influence the Pt aggregation on the surface are provided. Additionally, the CO interaction with a Pt/α-Al_2O_3 catalytic system is examined.

Finally, Chapter 5 summarizes the most important findings of this thesis.

2. Theoretical background

This chapter gives an overview of all the employed quantum chemical methods and their applications used for the analysis of structural and electronic properties of the catalytic system of interest. The structure analysis in the case of anionic platinum clusters such as ground state geometries, cluster reconstructions, and the reaction pathways were carried out using Density Functional Theory (DFT). The α-Al_2O_3 surface relaxation and its interfacial interactions with the small molecules were analyzed using embedded cluster models within density functional theory (DFT). For heavy elements such as platinum, the spin-orbit coupling effect are important to gain precise insight into the reconstructions and energetic ordering between the isomers and is taken into account by performing relativistic two-component calculations. The theoretical background of these methods is provided in Chapter 2.3. Chapter 2.4 provides information on the embedded cluster model used for incorporation of long-range electrostatic interactions on the local behavior of ionic α-Al_2O_3 surface as well as the consecutive interaction with small probe molecules, such as CO and CO_2.

2.1. Basic Quantum Chemistry

The electronic time-independent Schrodinger equation for stationary systems is defined as:

$$\hat{H}|\psi(\vec{r}_i, \vec{R}_A)\rangle = E|\psi(\vec{r}_i, \vec{R}_A)\rangle, \tag{1}$$

where $|\psi(\vec{r}_i, \vec{R}_A)\rangle$ is an electronic wave function dependent on the electron coordinates r and nuclear coordinates R. Within the Born-Oppenheimer approximation, the coupling between nuclei and electronic motion is neglected and therefore total wave function can be decomposed into electronic wavefunction $|\psi(\vec{r}_i, \sigma_i, \vec{R}_A)\rangle$ (σ_i is the spin of the electron) depending on nuclear positions as parameters and nuclear wavefunctions $|\chi(\vec{R}_A)\rangle$. The Hamiltonian $\hat{H}$ in eq. 1 contains all the interactions present between the electrons and the nuclei and its form is well-defined. The many-body wave function $|\psi\rangle$ can be defined in the form of Slater determinants introduced in the Hartree-Fock (HF) method to introduce the antisymmetry for the electronic wavefunction. However, in a many-body system, electron-electron interactions have to be addressed. The primary approach to address the electronic exchange interactions is given within the HF method. The two assumptions made in this method are [24]:

1. The electronic wave function can be described with one single Slater determinant.

2. The effective HF potential describes the interaction of one electron with an average field generated by all other electrons.

However, the approximation introduced in the HF method leads to two major problems. The one-electron approximation does not take Coulomb correlation between the electrons into consideration. Electron's movement depend on the immediate neighboring electron positions due to the repulsion and thus the use of an average field is not adequate. This inadequacy can lead for example to incorrect predictions for the conduction of electrons in the solids [25].

2.2. Møller Plesset Perturbation Theory

Electron Correlation means that electrons in a system are influenced by other electrons in their vicinity. This interaction is neglected in single electron approximation techniques such as the HF method. Thus, post Hartree Fock methods such as Møller Plesset Perturbation Theory (MPPT) [26] are used to further take into account the electronic correlation effect. The Ref. [24, 27] are used as a reference for the following section.

The basis for MPPT is the unperturbed Hamilton operator $\hat{H}^{(0)}$, which is the sum of the one-electron Fock operators $\hat{f}$:

$$\hat{H}^{(0)} = \sum_{i=1}^{n} \hat{f}(i) \tag{2}$$

with

$$\hat{f}(i) = -\frac{1}{2}\nabla_i^2 - \sum_A \frac{Z_a}{r_{iA}} + \sum_{j=1}^{n} [\hat{J}_j(i) - \hat{K}_j(i)] \tag{3}$$

where the $\hat{J}_j$ is the Coulomb operator and $\hat{K}_j$ is the exchange operator. Thus,

$$\hat{H}^{(0)}\Phi_0 = E_0^{(0)}\Phi_0 \tag{4}$$

The zeroth order (unperturbed) wave functions Φ_0 are the eigenfunctions of the HF unperturbed Hamiltonian $\hat{H}^{(0)}$ and the zeroth order energy $E_0^{(0)}$ is just a sum of MO energies $E_0^{(0)} = \sum_{i=1}^{N} \epsilon_i$. The perturbation $\hat{H}'$ is defined as the difference between the true molecular electronic Hamiltonian $\hat{H}$ and $\hat{H}^0$,

$$\hat{H}' = \hat{H} - \hat{H}^{(0)} = \hat{V}_{ee} - 2\langle \hat{V}_{ee} \rangle \tag{5}$$

The perturbation, $\hat{H}'$ is thus the difference between the true interelectronic repulsions and the Hartree-Fock interelectronic potential (i.e. an average potential). In HF method, the orbital energy is an energy calculated for one electron in the field of all electrons and also consists of the electronic repulsion due to the other electrons in its vicinity.

This leads to double counting of the electron-electron repulsion and is corrected in the first-order correction (denoted as $E_0^{(1)}$).

$$E_0^{(1)} = \langle \Phi_0 | \hat{H}^{'} | \Phi_0 \rangle = \langle \hat{V}_{ee} \rangle - 2\langle \hat{V}_{ee} \rangle = -\langle \hat{V}_{ee} \rangle \tag{6}$$

The first-order correction to the zeroth order energy is

$$\begin{aligned} E_0^{(0)} + E_0^{(1)} = \langle \psi_0^{(0)} | \hat{H}^{(0)} | \psi_0^{(0)} \rangle + \langle \Phi_0 | \hat{H}^{'} | \Phi_0 \rangle = \langle \Phi_0 | \hat{H}^{(0)} + \hat{H}^{'} | \Phi_0 \rangle \\ = \langle \Phi_0 | \hat{H} | \Phi_0 \rangle \end{aligned} \tag{7}$$

$$E_0^{(0)} + E_0^{(1)} = E_{HF} \tag{8}$$

As $\langle \Phi_0 | \hat{H} | \Phi_0 \rangle$ is the energy expectation values for the HF wavefunction Φ_0, the energy at first-order is equal to the HF energy E_{HF}.

The second-order correction to the energy, which is the first contribution to the correlation energy beyond the HF level, involves a sum over doubly excited determinants. These are generated by exciting two electrons from occupied orbitals i and j to the virtual orbitals a and b with the restriction over the summation in which each excited state is counted only once.

$$E_0^{(2)} = \sum_{i<j}^{occ} \sum_{a<b}^{vir} \frac{\langle \Phi_0 | \hat{H}' | \Phi_{ij}^{ab} \rangle \langle \Phi_{ij}^{ab} | \hat{H}' | \Phi_0 \rangle}{E_0 - E_{ij}^{ab}} \tag{9}$$

The matrix elements between the HF and the doubly excited state are given by the two electron integrals over the MOs. Thus, the difference between the total energy between the two Slater determinants is the difference in MO energies and the explicit second order Møller-Plesset correction is given as:

$$E_0^{(2)} = \sum_{i<j}^{occ} \sum_{a<b}^{vir} \frac{(\langle \phi_i \phi_j | \phi_a \phi_b \rangle - \langle \phi_i \phi_j | \phi_b \phi_a \rangle)\rangle)^2}{\varepsilon_i + \varepsilon_j - \varepsilon_a - \varepsilon_b} \tag{10}$$

Thus, the molecular energy in MP2 is computed as:

$$E_0^{(0)} + E_0^{(1)} + E_0^{(2)} = E_{HF} + E_0^{(2)} \tag{11}$$

The advantage of employing MP2 method is that it is an economical method which accounts for 80-90 % of the electron correlation energy of a large system. In this thesis, MP2 is used for computing the geometries of the CO/α-Al_2O_3 system, CO binding energies and vibrational frequencies.

2.3. Density functional theory

Solving the many-body problem by approximating the many-body wavefunction as done in the HF method is computationally demanding due to the presence of the coordinates of all electrons which are $3N$ (N = number of electrons) variables. This problem is drastically simplified in Density Functional Theory (DFT) when the electronic system is described in terms of the electron density $\rho(\vec{r})$, which is a function of only three variables (x, y, z). The Ref. [28] is used as a reference for the following section.

2.3.1. Hohenberg-Kohn theorem

The foundation of the DFT method is provided by the following two theorems laid out by Hohenberg and Kohn [29].

1. The external potential $v(\vec{r})$ is a unique functional of the electron density $\rho(\vec{r})$. As a result, the total ground-state energy E of any many-electron system is also a unique functional of $\rho(\vec{r})$, that is, E=$E[\rho]$.

$$E_0[\rho_0] = T[\rho_0] + E_{ee}[\rho_0] + \int \rho_0(\vec{r}) V_{ne} d\vec{r} = F_{HK}[\rho_0] + \int \rho_0(\vec{r}) V_{ne} d\vec{r} \tag{12}$$

where $F_{HK}[\rho_0]$ is a *Hohenberg-Kohn functional* and is independent of the external potential. However, this universal functional consisting of kinetic energy $T[\rho]$ and the electron-electron interaction $E_{ee}[\rho]$ is unknown. It is a major challenge in DFT research to find reasonable expressions for this unknown functional.

2. The exact functional $E[\rho]$ for the total energy has a minimum equal to the ground-state energy at the true ground-state density.

$$E_0 \leq E[\tilde{\rho}] = \int \tilde{\rho}(\vec{r}) V_{ne} d\vec{r} + F_{HK}[\tilde{\rho}], \tag{13}$$

where $\tilde{\rho}$ is the trial density which satisfies the boundary conditions as $\tilde{\rho} \geq 0$, $\int \tilde{\rho}\, \mathrm{d}\vec{r}$ = N.

2.3.2. Kohn-Sham Approach

In the Kohn-Sham approach [30], Kohn and Sham introduced a non-interacting reference system built from a set of atomic orbitals (that is one electron wave functions). The connection of this artificial non-interacting system with the interacting system of interest was established by choosing the effective potential such that the density obtained from the summation of the one-electron orbitals (Kohn-Sham orbitals $\varphi(\vec{r})$) equals the ground state density of the system consisting of interacting electrons.

For the non-interacting system, an effective local potential V_s is introduced. The Hamiltonian of that system is $\hat{H}_s$. As there are no interactions between the electrons, the exact solution for the ground state can be represented as a Slater determinant [28].

$$\hat{H}_s = -\frac{1}{2}\sum_i^N \nabla_i^2 + \sum_i^N V_s(\vec{r}_i) \tag{14}$$

The corresponding Kohn-Sham orbitals, φ_i are determined through the KS equations,

$$\hat{f}^{KS}\varphi_i = \varepsilon_i\varphi_i \tag{15}$$

where $\hat{f}^{KS}$ is the one-electron Kohn-Sham operator and defined as:

$$\hat{f}^{KS} = -\frac{1}{2}\nabla^2 + V_s(\vec{r}) \tag{16}$$

The major part of the kinetic energy is computed for non-interacting fermions as in the Hartree-Fock approach,

$$T_s[\rho(\vec{r})] = -\frac{1}{2}\sum_i^N \langle\varphi_i|\nabla^2|\varphi_i\rangle \tag{17}$$

The non-interacting kinetic energy does not account for the true kinetic energy of the interacting system. Therefore, the following separation of the functional $F[\rho]$ is introduced:

$$F[\rho(\vec{r})] = T_S[\rho(\vec{r})] + J[\rho(\vec{r})] + E_{XC}[\rho(\vec{r})], \tag{18}$$

Here, $T_S[\rho(\vec{r})]$ is the exact kinetic energy of the non-interacting system with the same density as the interacting system. The $J[\rho(\vec{r})]$ denotes the Coulomb repulsion, and E_{XC} is the exchange-correlation energy defined as,

$$E_{XC}[\rho] = (T[\rho] - T_S[\rho]) + E_{ncl}[\rho] \tag{19}$$

where the residual part of the kinetic energy is added to the non-classical electrostatic contributions $E_{ncl}[\rho]$. With this approach, the maximum information of the system is computed accurately and a small remaining part can be determined approximately.

The electronic density in terms of KS orbitals is given as:

$$\rho_s = \sum_i^N |\varphi_i(\vec{r})|^2 \tag{20}$$

The expression for the energy of the interacting system with a dependence on orbitals in the Kohn-Sham approach is given as:

$$\begin{aligned} E[\rho(\vec{r})] &= T_S[\rho] + J[\rho] + E_{XC}[\rho] + E_{Ne}[\rho] \\ &= -\frac{1}{2}\sum_{i}^{N}\langle\varphi_i|\nabla^2|\varphi_i\rangle + \frac{1}{2}\sum_{i}^{N}\sum_{j}^{N}\iint |\varphi_i(\vec{r_1})|^2\frac{1}{r_{12}}|\varphi_j(\vec{r_2})|^2 d\vec{r_1}d\vec{r_2} \\ &\quad - \sum_{i}^{N}\sum_{A}^{M}\int \frac{Z_A}{r_{1A}}|\varphi_i(\vec{r_1})|^2 d\vec{r_1} + E_{XC}[\rho(\vec{r})] \end{aligned} \tag{21}$$

The first term in eq. 21 describes the kinetic energy of the non-interacting electrons, the second term accounts for the Coulomb repulsion, the third term is the nuclear-electron interaction. The fourth term accounts for the exchange-correlation term containing all the unknown entities such as the residual part of the kinetic energy emerging from the electron interactions and all non-classical corrections to the electron-electron repulsion energy. Furthermore, nuclear repulsion is also included by adding internuclear repulsion V_{NN} to the total energy.

Thus, the electron density can be used in the energy expression (eq. 21) in terms of non-interacting orbitals and can be subjected to the variational principle with respect to independent variation in the orbitals. The resulting expression eq. 22 shows that the effective potential V_s, is needed to correct the orbitals of the non-interacting reference system, exactly equal to the sum of nucler potential, classical Coulomb potential, and the potential generated by E_{XC}.

$$\left(-\frac{1}{2}\nabla^2 + \left[\int \frac{\rho(\vec{r})}{r_{12}}dr_2 + V_{XC}(\vec{r_1}) - \sum_{A}^{M}\frac{Z_A}{r_{1A}}\right]\right)\varphi_i = \left(-\frac{1}{2}\nabla^2 + V_S(\vec{r})\right)\varphi_i = \varepsilon_i\varphi_i \tag{22}$$

The term in the bracket corresponds to V_S in the KS one electron operator. The V_{XC} potential is given as the functional derivative of E_{XC} with respect to ρ,

$$V_{XC} = \frac{\delta E_{XC}}{\delta\rho} \tag{23}$$

Thus the KS equations are solved iteratively. However, for the unknown exact form of V_{XC}, some approximations are introduced.

2.3.3. Exchange-correlation functionals

As described previously, the exchange-correlation functional $E_{XC}[\rho]$ is unknown and therefore explicit approximations have to be introduced. The quality of the results obtained using DFT solely depends on the accuracy of the chosen approximation for $E_{XC}[\rho]$. Therefore, it is important to choose a suitable functional based on the system and properties of interest.

2.3.3.1. Local Density Approximation

The central idea of this model system is the hypothetical uniform electron gas in which electrons move on a positive background charge distribution such that the whole ensemble is charge-neutral. The simple form of the E_{XC} is

$$\mathrm{E}_{\mathrm{XC}}^{\mathrm{LDA}}[\rho] = \int \rho(\vec{r})\varepsilon_{XC}(\rho(\vec{r}))d\vec{r} \tag{24}$$

where, $\varepsilon_{XC}(\rho(\vec{r}))$ is the exchange-correlation energy per particle of a uniform electron gas of density $\rho(\vec{r})$. This energy per particle is weighted with the probability $\rho(\vec{r})$ such that an electron is present at a particular position in space. This is why it is called Local Density Approximation. This quantity is further split into exchange and correlation contributions given as:

$$\varepsilon_{XC}(\rho(\vec{r})) = \varepsilon_X(\rho(\vec{r})) + \varepsilon_C(\rho(\vec{r})) \tag{25}$$

The exchange part $\varepsilon_X(\rho(\vec{r}))$ is defined by the exchange energy of an electron in a uniform electron gas of a particular density, given as:

$$\varepsilon_X = -\frac{3}{4}\sqrt[3]{\frac{3\rho(\vec{r})}{\pi}} \tag{26}$$

However, the explicit expression for ε_C is unknown. Therefore, various analytical expressions for ε_C are reported based on the highly accurate quantum Monte Carlo simulations of the homogeneous electron gas. The most recent and accurate representation of ε_c is given by Perdew and Wang. Simple metals such as sodium can be well described using the straightforward approach of LDA. However, the systems consisting of varying density such as complex solids are not described well.

In the cases consisting of unequal spin α and β densities, often LDA is replaced by the *Local Spin Density Approximation* (LSDA) where the sum of individual densities is raised to $\frac{4}{3}$ power

$$E_X^{LSDA}[\rho] = -2^{\frac{1}{3}} \int (\rho_\alpha^{\frac{4}{3}} + \rho_\beta^{\frac{4}{3}})d\vec{r} \tag{27}$$

LSDA approach is an improvement over the LDA, however, LSDA approximation leads to an underestimation of the exchange energy by ≈10% for a molecular system, resulting in an error larger than the whole correlation energy. This can also result in artificial stabilization of the high spin states. The electron correlation is also overestimated by a factor of 2, leading to an overestimation of the bond strengths by ≈100 KJ/mol. However, the accuracy achieved using LSDA approximation is close to the Hartree-Fock method. LSDA approximation can be applied for the metal systems where the reasonable approximation for slowly varying density is sufficient [24].

2.3.3.2. Generalized gradient approximation

To account for the inhomogeneity of the true density and address the limitations of LDA, the GGA is not only taking $\rho(\vec{r})$ into account but also uses the gradient of the charge $\nabla\rho(\vec{r})$. It is expressed as:

$$E_{XC}^{GGA}[\rho] = \int f(\rho(\vec{r}), \nabla\rho(\vec{r}))d\vec{r}, \tag{28}$$

There are several semi-empirical functionals containing parameters that are calibrated against reference values. E_{XC}^{GGA} is often split into exchange and correlation contributions and approximations are applied individually to each of the terms. In this thesis, PBE functional [31] was used for studying Al_2O_3 surface.

GGA functional are further improved in accuracy by adding non-interacting positive kinetic energy density $\tau(\vec{r})$. These functionals are called as meta-GGA functionals. Their general form is

$$E_{XC}^{mGGA} = \int f(\rho(\vec{r}), \nabla\rho(\vec{r}), \tau(\vec{r}))d\vec{r} \tag{29}$$

$$\tau(\vec{r}) = \frac{1}{2}\sum_{i=1}^{N} |\nabla\phi_i(\vec{r})|^2 \tag{30}$$

where $\phi_i(\vec{r})$ are the KS orbitals. These functionals are the semilocal approximations where $\tau(\vec{r})$ depends on the gradient of the orbitals at point $\vec{r}$. These kind of functionals consists of no empirical parameters and are suitable for describing different chemical bonds such as covalent, metallic or weak bonds in solids and molecules compared to LDA and GGA functionals. In this thesis, TPSS meta-GGA exchange-correlation functional [32] is used for describing $Pt_nD_{2n}^-$ clusters.

2.3.3.3. Hybrid functionals

It is usually the case that the exchange contributions are significantly larger compared to correlation contributions. In GGA functionals, both exchange and correlation parts are approximated which can result in an error of 5-7 kcal/mol. This is overcome in an approach where a certain amount of exact exchange energy is incorporated. These approaches are referred to as hybrid functionals since they represent a hybrid between pure density functionals for exchange contributions and exact Hartree-Fock exchange. The most widely used hybrid functional nowadays and also used in this thesis is B3LYP [33, 34]. It is expressed as:

$$E_{XC}^{B3LYP} = (1-a_0)E_X^{LSDA} + a_0E_X^{HF} + a_xE_X^{B88} + a_cE_C^{LYP} + (1-a_c)E_C^{VWN} \tag{31}$$

In the B3LYP functional, the exchange energy contains terms for HF exchange along with B88 [35] and LSDA and the LYP [34] as well as VWN [36] functionals for the electron-electron correlation. The parameters a_0=0.2, a_x=0.72, a_c=0.81 determine the mixing of individual functionals and were fitted to the experimental atomization energies.

2.4. Density of States

The Density of States (DOS) is a useful quantity in electronic structure studies. It is defined as the number of states per unit energy range per unit volume of the system [37].

$$\rho(\varepsilon) = \frac{1}{V}\sum_{i=1}^{\infty}\delta(\varepsilon - \varepsilon_i) \tag{32}$$

where the sum extends over all eigenstates of the KS Hamiltonian.

2.5. Relativistic two-component method

In quantum chemistry, the computation of the electronic structure of atoms and molecules and the corresponding prediction of their properties can be achieved by solving the electronic Schrödinger equation given in eq. 1 which describes the electrons in the field of the nuclei in a non-relativistic way. It describes the properties of light atoms and molecules well. However, it is not an appropriate model when going down in the periodic table towards the heavy elements, where relativistic effects have a significant influence. Electrons of low l values, especially s electrons penetrate the atomic core and experience a relativistic retardation effect near the highly charged nuclei giving rise to shell contraction. This leads to them screening the nuclear charge better. Therefore, the electrons in shells with higher l values $l\geq 2$ are further away from the nucleus and experience a smaller effective nuclear charge and they expand.

The relativistic one-electron Dirac equation in a potential $\hat{V}_R(r)$ is written as [38],

$$\hat{H}\psi = (\beta c^2 + \hat{V}_R(r) + c\vec{\alpha}\cdot\vec{p})\psi = E\psi, \tag{33}$$

where c denotes the velocity of light, $\vec{p}$ is the momentum and $\hat{V}_R$ is the Coulomb potential describing electron-nuclear interactions. The elements (α_x, α_y, α_z) of vector $\vec{\alpha}$ as well as β are 4×4 matrices.

According to Dirac's theory, these matrices should fulfill the following two conditions,

$$\alpha_i^2 = \beta^2 = I_4 \tag{34}$$

and

$$\alpha_i\alpha_j + \alpha_j\alpha_i = \alpha_i\beta + \beta\alpha_i = O_4, i \neq j, \tag{35}$$

where, I_4 and O_4 are the 4×4 identity and zero matrices respectively. The matrices $\vec{\alpha}_i$ and β can be written as,

$$\vec{\alpha}_i = \begin{pmatrix} 0 & \vec{\sigma}_i \\ \vec{\sigma}_i & 0 \end{pmatrix}, \beta = \begin{pmatrix} \hat{I}_2 & 0 \\ 0 & -\hat{I}_2 \end{pmatrix} \tag{36}$$

The $\vec{\sigma}_i$ are the two-dimensional Pauli spin matrices,

$$\sigma_x = \begin{pmatrix} 0 & 1 \\ 1 & 0 \end{pmatrix}, \sigma_y = \begin{pmatrix} 0 & -i \\ i & 0 \end{pmatrix}, \sigma_z = \begin{pmatrix} 1 & 0 \\ 0 & -1 \end{pmatrix} \tag{37}$$

The Dirac Hamiltonian $\hat{H}$ becomes,

$$\hat{H}_D = \begin{pmatrix} (\hat{V} + c^2)I_2 & c\vec{\sigma} \cdot \vec{p} \\ c\vec{\sigma} \cdot \vec{p} & (\hat{V} - c^2)I_2 \end{pmatrix} \tag{38}$$

I_2 is the 2×2 identity matrix. This leads to the eigenvalue equation

$$\begin{pmatrix} \hat{V}I_2 & c\vec{\sigma} \cdot \vec{p} \\ c\vec{\sigma} \cdot \vec{p} & (\hat{V} - 2c^2)I_2 \end{pmatrix} \begin{pmatrix} \psi^L(\vec{r}) \\ \psi^S(\vec{r}) \end{pmatrix} = \epsilon \begin{pmatrix} \psi^L(\vec{r}) \\ \psi^S(\vec{r}) \end{pmatrix} \tag{39}$$

This is the four-component form of the Dirac equation and describes the behavior of both electrons and positrons. The adjusted Dirac energy ϵ is,

$$\epsilon = E - c^2 \tag{40}$$

The resulting wavefunction can be divided into large and small component,

$$\psi(\vec{r}) = \begin{pmatrix} \psi^L(\vec{r}) \\ \psi^S(\vec{r}) \end{pmatrix} \tag{41}$$

Solving a four-component Dirac equation is tedious due to the presence of positronic states. These states have negligible influence on the stability and molecular structure and thus are of no chemical importance. Consequently, it is helpful to decouple the positronic and electronic states. This is done by a unitary transformation of the Dirac Hamiltonian,

$$\hat{H} = \mathcal{U}^\dagger \hat{H}_D \mathcal{U} = \begin{pmatrix} h_+ & 0 \\ 0 & h_- \end{pmatrix}. \tag{42}$$

This makes the Dirac Hamiltonian $\hat{H}_D$ block diagonal with respect to the large and small components. While h_+ and h_- are the two- component Hamiltonians that act on electronic and positronic states respectively. Thus, transforming the four-component Dirac wavefunction into a two-component wavefunction consisting only of the electronic part

$$\mathcal{U}^\dagger \begin{pmatrix} \psi^L(r) \\ \psi^S(r) \end{pmatrix} = \begin{pmatrix} \phi+ \\ 0 \end{pmatrix} \tag{43}$$

where $\phi+$ is an eigenfunction of the two- component Hamiltonian h_+. This all-electron formulation is used for example in the Douglas-Kroll-Hess-approach (DKH) [39] or zeroth-order regular approximation (ZORA) [40].

Another economical way of determining relativistic effects is by modeling the core electrons with effective core potentials (ECP) [41]. They are fitted to relativistic all-electron calculations. The usage of scaler relativistic ECPs leads to a one-electron term which is added to the Hamiltonian matrix. An extension to the spin-orbit interaction is accounted for by employing the complex orbitals called spinors. The quasi- relativistic 'valence only' Hamiltonian consisting of SO effects via ECPs is defined as,

$$\hat{H} = \sum_i [\sigma_0 \hat{h}^0(i) + \vec{\sigma} \cdot \vec{h}_{SO}(i)] + \hat{V}_{ee} + \hat{V}_{NN} \tag{44}$$

where $\hat{V}_{ee}$ and $\hat{V}_{NN}$ are the repulsive interaction between the electrons and nuclei respectively, $\hat{h}^0$ is the sum of the non-relativistic kinetic energy, electronic attraction under the effective nuclear charges and the scalar relativistic part of the core potentials, σ_0 is the 2×2 unity matrix. $\vec{\sigma} \cdot \vec{h}_{SO}$ accounts the electron spins and the orbital momenta, and the $\vec{h}_{SO}$ is defined as the product of orbital momentum and parameters fitted to the four component treatment. Due to the presence of $\vec{h}_{SO}$, the electronic spin is no longer a conserved quantity and the eigenfunctions of the Hamiltonian are complex. Thus DFT wavefunction is constructed from complex two-component single particle-functions, called as spinors $\psi_k(\vec{x})$,

$$\psi_k(\vec{x}) = \begin{pmatrix} \psi_k^{\alpha}(\vec{r}) \\ \psi_k^{\beta}(\vec{r}) \end{pmatrix} \tag{45}$$

The single-particle density matrix in the spin space is given as,

$$\gamma(\vec{x}, \vec{x}') = \sum_{k=1}^{N} \psi_k(\vec{x}) \psi_k^{\dagger}(\vec{x}') = \begin{pmatrix} \gamma^{\alpha\alpha}(\vec{r}, \vec{r}') & \gamma^{\alpha\beta}(\vec{r}, \vec{r}') \\ \gamma^{\beta\alpha}(\vec{r}, \vec{r}') & \gamma^{\beta\beta}(\vec{r}, \vec{r}') \end{pmatrix} \tag{46}$$

The particle number density matrix then can be obtained from the trace of $\gamma(\vec{x}, \vec{x}')$,

$$n(\vec{r}, \vec{r}') = tr[\gamma(\vec{x}, \vec{x}')] = \gamma^{\alpha\alpha}(\vec{r}, \vec{r}') + \gamma^{\beta\beta}(\vec{r}, \vec{r}') \tag{47}$$

From this, the particle density of the system can be obtained by integrating over the symmetric part $r = r'$. The spin vector density matrix $\vec{m}(r, r')$ can be obtained from the trace of the product of $\gamma(\vec{x}, \vec{x}')$ and the Pauli matrices (given in eq. 37),

$$\vec{m}(\vec{r}, \vec{r}') = tr[\vec{\sigma}\gamma(\vec{x}, \vec{x}')] = \begin{pmatrix} \gamma^{\alpha\beta}(\vec{r}, \vec{r}') + \gamma^{\beta\alpha}(\vec{r}, \vec{r}') \\ i[\gamma^{\alpha\beta}(\vec{r}, \vec{r}') - \gamma^{\beta\alpha}(\vec{r}, \vec{r}')] \\ \gamma^{\alpha\alpha}(\vec{r}, \vec{r}') + \gamma^{\beta\beta}(\vec{r}, \vec{r}') \end{pmatrix} = \begin{pmatrix} m_x(\vec{r}, \vec{r}') \\ m_y(\vec{r}, \vec{r}') \\ m_z(\vec{r}, \vec{r}') \end{pmatrix} \tag{48}$$

yielding the spin expectation value,

$$\frac{1}{2} \int \vec{m}(r) dr = \langle \vec{S} \rangle \tag{49}$$

Thus, the SO contribution to the energy is,

$$E_{SO}[\vec{m}(\vec{r},\vec{r}')] = \int [\hat{h}_{SO} \cdot \vec{m}(\vec{r},\vec{r}')]_{r=r'} dr \tag{50}$$

In addition, the Coulomb energy is given as a functional of the particle number density,

$$E_J[n(\vec{r})] = \frac{1}{2} \iint \frac{n(\vec{r})n(\vec{r}')}{|\vec{r}-\vec{r}'|} dr dr' \tag{51}$$

and the Coulomb operator is a real quantity and independent of the spin, defined as,

$$\hat{J}[n(\vec{r})] = \sigma_0 \int \frac{n(\vec{r}')}{|\vec{r}-\vec{r}'|} dr' = \begin{pmatrix} \hat{J} & 0 \\ 0 & \hat{J} \end{pmatrix} \tag{52}$$

The exchange-correlation energy for the two-component DFT formalism is a functional of the eigenvalues $\rho_{\pm}(\vec{r})$ of the single-particle density matrix $\gamma(x)$ in the space of spin states,

$$\rho_{\pm}(\vec{r}) = \frac{1}{2}[n(\vec{r}) \pm m(\vec{r})] \tag{53}$$

$$E_{XC} = E_{XC}[\rho_{\pm}(\vec{r})] = E_{XC}[n(\vec{r}), m(\vec{r})] = \int F_{XC}(n(\vec{r}), |\vec{\nabla} n(\vec{r})|, m(\vec{r}), |\vec{\nabla} m(\vec{r})|, ...) dr \tag{54}$$

and is a functional of the particle number density and the absolute value of the spin vector density. In this thesis, spin-orbit coupling effects were employed for the study of anionic platinum deuteride clusters.

2.6. Embedded cluster method

Nowadays, most calculations on surface reactions are DFT calculations with periodic boundary conditions. An alternative approach is the embedded cluster model [42, 43]. The advantage of the embedded cluster model is that the local part of the system can be treated quantum mechanically at various levels of theory. The whole system in the embedded cluster model is divided into three parts: a) the core part which is treated quantum mechanically, b) an intermediate layer in which cations are replaced by effective core potentials (ECPs) and c) the outer environment is an array of point charges mimicking the crystal structure. The replacement of the cations with the ECPs at the periphery is necessary in order to avoid artificial fluctuation in the electron density (Figure 1).

However, to analyze the various properties of the ionic crystals such as internal electrostatic potential, the calculation of the lattice sum is essential. However, for a large array of point charges such as in the embedded cluster model, determining the Coulomb potential is quite challenging due to its long-range nature. Thus, to determine the Madelung constant of the ionic crystal, the direct summation technique of Evjen type

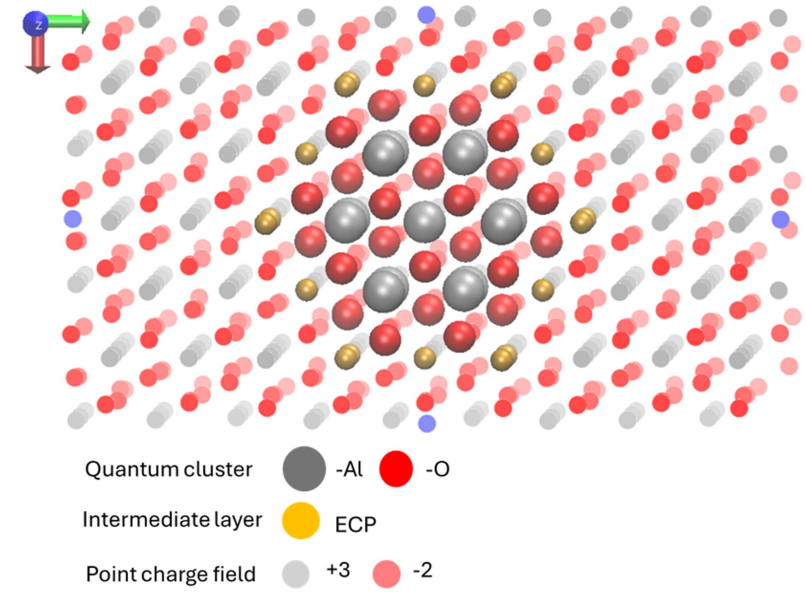

Figure 1.: Schematic of an embedded cluster model of the α-Al_2O_3 surface.

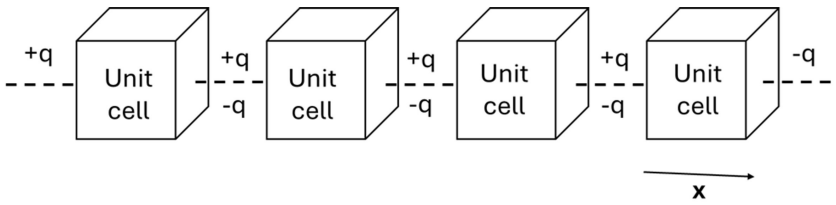

Figure 2.: Schematic of the fractional point charges at the border of unit cell to annihilate the dipole of a unit cell.

[42] can be used. In this technique, the dipole moment is minimized in the unit cell by distributing the corner and face atoms over all equivalent symmetry points, facilitating the convergence of the lattice sums. Furthermore, this technique is extended by placing additional artificial point charges to eliminate the lowest multipole moments at the border of the unit cells extended to a large point charge field [43–45].

The Figure 2 and 1 (blue circles) show the addition of two charges (+q, -q) at the boundary of each unit cell to eliminate the dipole moment. After extending the unit cell in x and y direction to form the large point charge field, the fractional charges at the inner boundaries of the extended unit cell cancel out and only charges at the outer boundaries remain. The advantage of this approach is that the multipole moments are small and are not influenced by the size of the point charge field. The Coulomb potential also converges fast.

2.7. Nuclear-Independent Chemical Shift (NICS)

The nucleus-independent chemical shift method [46] is used to examine and quantify a system's aromaticity. In this method, the response of the aromatic system to an external magnetic field is quantified as an aromatic character. However, the aromaticity is evaluated indirectly by determining the chemical shift at a particular location in space thereby indicating the strength of the induced magnetic field at this particular location. The strength of the induced magnetic field is measured by placing a probe molecule (with no basis function and nucleus) at several locations around the system to gain a good understanding about the degree of (local) aromaticity [47]. The negative isotropic magnetic shielding function at a selected position in space is called nucleus-independent chemical shift (NICS). The NICS > 0 denotes a paratropic current (antiaromaticity) while NICS < 0 indicates a diatropic current (aromaticity).

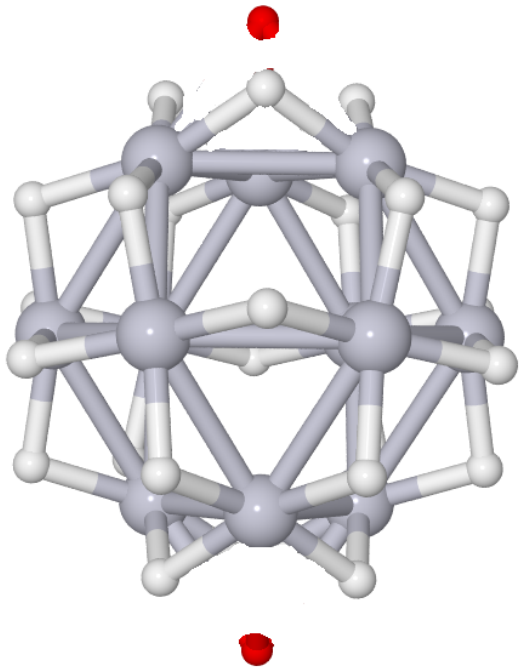

Figure 3.: Schematic of the NICS probe atom (red) placement around a platinum cluster

Chemical shielding constants are calculated using the Gauge-Including Atomic Orbitals (GIAO) within DFT. However, due to the presence of an external magnetic field, the exchange-correlation DFT functional depends on the electron density as well as on current density $j(\vec{r})$ [48].

$$E_{XC}[\rho(\vec{r})] \rightarrow E_{XC}[\rho(\vec{r}), j(\vec{r})] \tag{55}$$

The dependence on the current density is unknown and therefore the shielding constants are calculated using commonly used exchange-correlation energy functionals which depend on the electron density and its derivatives.

$$E_{XC}[\rho(\vec{r}), j(\vec{r})] \approx E_{XC}[\rho(\vec{r})] \tag{56}$$

This is called the "uncoupled density functional" formalism. Within this formalism the chemical shielding tensors for a closed-shell system is defined by a sum of partial chemical shifts arising from occupied molecular orbitals (MOs) Ψ_i given as [46] (The upper indices in the parentheses of the wavefunction denote the order of perturbation),

$$\begin{aligned}\vec{\sigma} = \frac{1}{2c^2}\sum_{k}^{occ}\left\langle \Psi_k^{(0)}\left|\frac{\vec{r}\vec{r}_N I - \vec{r}_N \otimes \vec{r}}{|\vec{r}-\vec{R}_N|^3}\right|\Psi_k^{(0)}\right\rangle - \\ \frac{2}{c}\sum_{k}^{occ}\left\langle \Psi_k^{(0)}\left|\frac{\vec{L}_N}{|\vec{r}-\vec{R}_N|^3}\right|\Psi_k^{(1)}\right\rangle\end{aligned} \tag{57}$$

where $\vec{L}_N = \vec{r}_N \times \nabla$, $\vec{r}_N = \vec{r}\text{-}\vec{R}_N$ and I denotes the identity matrix. The first-order perturbed wave function $\Psi_k^{(1)}$ is expanded in terms of excited states of the unperturbed system [47]. In the equation 57, the first term denotes the diamagnetic term while the second denotes the paramagnetic term. The $\vec{r}$ defines the electronic position and $\vec{R}_N$ to the vector position where the NICS value is calculated. The $\vec{L}_N$ is the angular momentum operator. However, the equation 57 corresponds to the common gauge formulation of the NMR shielding tensor where both the diamagnetic and paramagnetic components depend on the gauge origin. The gauge-origin dependence vanishes at an infinite basis-set limit while it is real for a finite basis-set. Thus, the gauge-independent atomic orbitals (GIAO) technique [49] is used for practical calculations.

The classification of NICS value can be done based upon the placement of the probe atom such as NICS(0), NICS (1) and NICS $(r)_\pi$ [50]. The probe atom when placed at the center of the system under study is classified as NICS(0). However, the disadvantage of NICS(0) is the so-called σ-contaminations which arise from the nearby σ bonds of the system which mask the behavior of the π contribution. Therefore, the placement of the NICS probe atom at 1Å above the system plane (denoted as NICS(1)) is recommended to reduce the effects of the σ-contaminations and π contributions are not affected. This position is shown in figure 3 with the red circles.

2.8. Nudged Elastic Band (NEB) method

One important aspect of chemical reactions is the determination of the lowest energy path during the rearrangement of a group of atoms going from one stable configuration

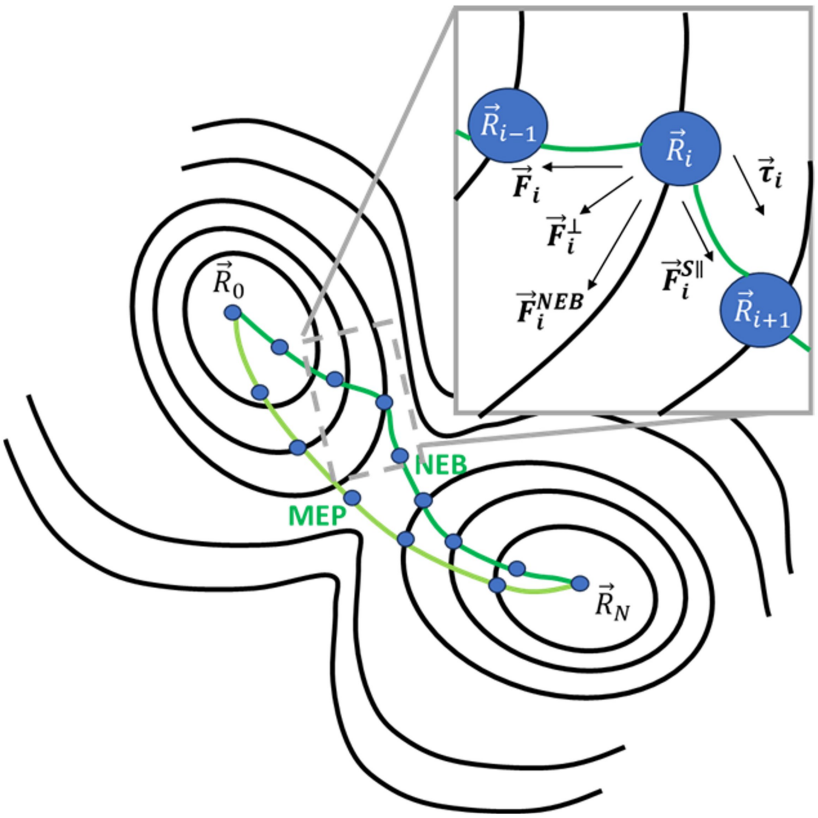

Figure 4.: Illustration of the Nudged Elastic Band (NEB) method.

to another. This is often called the minimum energy path (MEP). This path is frequently used to define the reaction coordinate for molecular transitions or changes in the conformation of the molecules. Maxima in the MEP are saddle points on the potential surface and their corresponding energies are activation energies. Therefore, gathering information regarding the shape of the MEP is of major interest. One of the methods used for determining the lowest energy reaction pathway and activation energy is the Nudged Elastic Band (NEB) method [51, 52]. A set of images of the system between the initial and final states are used for finding the MEP. It is typically in the order of 4-20 between the two fixed points (initial and the final state) like an elastic band. An elastic band with *N+1* images is denoted as $[\vec{R}_0, \vec{R}_1, \vec{R}_2 ..... \vec{R}_N]$ where the endpoints $\vec{R}_0$ and $\vec{R}_N$ are fixed corresponding to the initial and final states. The intermediate *N-1* images are adjusted by the optimization algorithm. The net force on a specific state is determined by the sum of three forces, a parallel spring force connected to neighboring states ($\vec{F}_i^s \mid_{\parallel}$), a perpendicular force induced by the potential energy surface (denoted as true force, $\vec{F}_i^s \mid_{\perp}$) and the unprojected forces (Figure 4).

A spring force is added between the images to ensure continuity in the path. This spring force does not interfere with the elastic band convergence to the MEP and also

ensures that the true force does not affect the distribution of the images. The tangent at a particular image $\vec{R}_i$ is estimated from the adjacent images along the path, $\vec{R}_{i+1}$ and $\vec{R}_{i-1}$. It is estimated by bisecting the unit vectors, defined as [51],

$$\vec{\tau}_i = \frac{\vec{R}_i - \vec{R}_{i-1}}{|\vec{R}_i - \vec{R}_{i-1}|} + \frac{\vec{R}_{i+1} - \vec{R}_i}{|\vec{R}_{i+1} - \vec{R}_i|} \tag{58}$$

and normalizing, $\vec{\tau}=\frac{\vec{\tau}}{|\vec{\tau}|}$. This ensures the adjacent images are equispaced even in the regions of large curvature. The total force acting on the image is equal to the sum of the spring force along the tangent and the true force perpendicular to the tangent. This projection of force is called "nudging" and is given as

$$\vec{F}_i = \vec{F}_i^s \mid_{\parallel} -\nabla E(\vec{R}_i) \mid_{\perp}, \tag{59}$$

The true force is given as

$$\nabla E(\vec{R}_i) \mid_{\perp} = \nabla E(\vec{R}_i) - \nabla E(\vec{R}_i).\vec{\tau}_i, \tag{60}$$

In above equations, E denotes the energy of the system, which is a function of all the atomic coordinates and $\vec{\tau}_i$ is the normalized local tangent at image $\vec{R}_i$. The spring force as

$$\vec{F}_i^s \mid_{\parallel} = k[(\vec{R}_{i+1} - \vec{R}_i) - (\vec{R}_i - \vec{R}_{i-1})].\vec{\tau}_i\vec{\tau}_i, \tag{61}$$

The spring forces control only the spacing between the images.

If this projection scheme is not used, the elastic band does not follow the curved MEP due to the spring forces often leading to "corner cutting". The true force acting along the path forces the images to slide away from the high-energy regions and towards the minima, often called the "sliding down" effect. This leads to a decrease in the density of images at the maxima where it's needed to describe the transition state. Often, MEPs contain one or more intermediate minima and the saddle point neighboring to the initial state may not represent the highest saddle point for the transition.

Sometimes, problems may occur while using the NEB method where the elastic band does not converge to the MEP. One reason for this can be the presence of a large spring force parallel to the path compared to the perpendicular force. Another reason can be the use of too many images used in the elastic band. This can lead to the formation of kinks on the elastic band which can oscillate back and forth preventing a smooth convergence of the MEP [53]. This problem is solved by adding a switching function f(ϕ) [53] to the parallel force when the tangent is increased.

$$f(\phi) = \frac{1}{2}(1 + \cos(\pi(\cos\phi))) \tag{62}$$

where f(ϕ) is 0 for a straight path and 1 if adjacent segments of the path form a right angle. Thus, the force on the image $\vec{R}_i$ is then given as

$$\vec{F}_i^{NEB} = \vec{F}_i + f(\phi_i)(\vec{F}_i^s - \vec{F}_i^s.\vec{\tau}_{\parallel}\vec{\tau}_{\parallel}) \tag{63}$$

The use of a switching function tends to pull the elastic band off the MEP at the curved path. Therefore, this approach can lead to an overestimation of the saddle point energy. This issue is solved by using a modified NEB method [52] where only the image with higher energy and the image $\vec{R}_i$ is used in the estimation instead of the adjacent images.

In this study, the NEB method was used to analyze the Pt cluster transformation.

3. Study of anionic platinum clusters in gas phase

Introduction

Precious transition metals are widely applied in nanocatalysts, electronic devices, data storage and functional nanostructured materials [54, 55]. However, these transition metals are a limited resource and quite expensive. Therefore, efforts are made to efficiently use precious metals in the catalysts in the form of nanoclusters or even single atoms supported on various metal-oxide surfaces [56]. In these nanoclusters, the quantum confinement effects and unique atom arrangements lead to their unique size-dependent properties such as a large surface area to volume ratio, good structure-activity relationship, and additional active sites at the surface due to a large fraction of low coordinated surface atoms [57].

Among these transition metals, Pt has a particular affinity towards hydrogen [23] and therefore its nanoclusters are one of the important components in heterogeneous catalyst used for hydrogen evolution reaction and alkane hydrogenation reaction [8, 9]. In such catalytic reactions, hydrogen is omnipresent, and its dissociation and chemisorption on the cluster surface are elementary steps of the process. However, such interactions with the hydrogen induces structural reconstructions of Pt clusters in the gas phase as well as those supported on the metal-oxides [58–60]. The experiment conducted by Bus *et al.* [61] on Pt/Al_2O_3 and Pt/SiO_2 systems using X-ray absorption spectroscopy and electron microscopy found that hydrogen prefers to bind in n-fold sites and can induce structure reconstruction. A Pt-Pt bond length contraction was also noted which made the cluster structure strongly dependent on the hydrogen coverage. Mager-Maury *et al.* [23] found similar effects. They used DFT and molecular dynamics to investigate the behavior of the $Pt/\gamma Al_2O_3$ system with respect to hydrogen coverage. According to their findings, the Pt_{13} cluster favored biplanar morphology in the absence of hydrogen. Upon increased hydrogen coverage, it reformed into the cuboctahedral morphology. Another DFT study carried out by Zhou *et al.* showed that at higher hydrogen coverage, a symmetrical icosahedral Pt_{13} cluster undergoes structural transition to an *fcc*-like structure. Larger Pt_n (n=38-40) clusters studied by Borbon *et al.* [62] reported that decahedron Pt structure transforms into a spherical structure allowing release of the internal strain and elongation of Pt-Pt bond lengths upon hydrogen adsorption. However, in such processes, different interactions play a role such as adsorbate-nanoclusters,

nanocluster-metal oxide support, and adsorbate-metal oxide support which leads to difficulties in understanding underlying contributions to the catalytic activity.

Thus, to understand the peculiar effects of Pt atoms in contrast to the collective effects of metal and surface on catalytic processes, it is necessary to analyze the well-defined and isolated Pt clusters in the gas phase. This can help to deduce the property evolution with respect to an increase in the cluster size. The size of the cluster and their symmetries can be determined experimentally. However, the direct or indirect determination of cluster transformations is non-trivial in the experiment. Due to these limitations, investigations using quantum chemical methods are necessary to accurately predict the cluster structure. In the structural analysis of heavy element nanoclusters such as Pt, structure prediction using a theoretical approach becomes difficult due to the presence of open *d*-shells in these clusters which can lead to several electronic states along with various spin multiplicities and structural geometries [63]. A recent study on bare Pt_n^- (n=6-13) clusters using a combination of trapped ion electron diffraction (TIED) and DFT calculations showed the structural evolution and the significant influence of the relativistic effects on the stability of the clusters [64].

Evolution of the structure in the sub-nanometer clusters such as edges, steps, kinks, and defects can alter the electronic and catalytic properties of a cluster. However, these structural alterations can enhance the catalytic activities taking place on the surface. One of the main issues with these nanoparticles is the significant changes in the catalytic properties observed upon adding or removing a single atom to or from a cluster [65]. For example, Imaoka *et al.* studied the structure-activity relationship of the Pt_{12} and Pt_{13} clusters for the oxygen reduction reaction. Their results showed that the catalytic activity was more than 2-fold on Pt_{12} clusters compared to the very stable icosahedral Pt_{13} cluster. The result also revealed that the activity does not depend on the cluster size but on its geometric structure. The low activity of Pt_{13} was attributed to its so-called magic number atomic configuration. It is evident in the experiments that certain metal clusters exhibit significant stability consisting of a special number of atoms and are predominantly generated compared to other configurations [66]. These special numbers are called geometric "magic numbers". For metal nanoparticles of close-packed metals, the geometric magic numbers generate high symmetric structures such as icosahedral, ino-decahedral and cuboctahedral with I_h, D_{5h} and O_h symmetries. These magic numbers coincide with the shell-closing effect and are generally spherical [66, 67]. Such formation of magic-number nanoclusters are observed in nanoparticles of Au [68], Pt[65, 69], and Ni [70].

We investigated the influence of deuterium exposition on the structural evolution of Pt-deuterides $Pt_nD_{2n}^-$ (n=6-13) in a joint experimental and computational study. The Trapped Ion Electron Diffraction (TIED) experiments were conducted in the group of PD Detlef Schooss. My task was to perform DFT calculations on several guess structures. The structures well-fitting to the TIED data are then assigned by comparing the profile factors calculated for the simulated candidate structure and the experiment.

Before proceeding to the computational details and the obtained results, it is worth mentioning some important details of the TIED technique. The experimental setup of the TIED is described in detail in reference [71]. Here, a short summary of the technique's working principles will be presented. The TIED technique is a mass-selective method employed for determining the cluster structure via diffraction measurements. The electron beam is scattered by the spatial arrangements of the cluster atoms forming scattering patterns and from these, the cluster structure is determined. With the help of a magnetron sputter source, Pt anions were generated. Their deuterides were generated by mixing the deuterium (0.3 vol %) into the sputter gas (He and Ar). The mass distribution of the formed clusters was analyzed using a time-of-flight mass spectrometer. The formed clusters were mass-selected and stored in the quadrupole ion trap. A 40 keV electron beam was passed through the anionic cluster cloud consisting of ca. 10^5 to 10^6 clusters. The scattered electrons were detected during the exposure periods of 20-30 s on a phosphor screen assembly and integrated on an external charge-coupled device (CCD) camera. The reference picture was extracted without cluster ions in the trap. With cluster ions in the trap, several hundred pictures were accumulated. The total scattering function I_{tot}(s) as a function of the electron momentum transfer s was extracted by radially averaging over the sum of these several hundred background corrected diffraction pictures. The atomic scattering intensity I_{at} [72] and an additional unspecific polynomial based background I_{back} was taken into account. The experimental reduced molecular scattering function sM^{exp} (s) = $s(I_{tot} - I_{at} - I_{back}) / I_{at}$ was calculated. The obtained experimental scattering function was then compared with the scattering function (sM^{theo}) calculated for the theoretically obtained candidate structures,

$$sM^{theo}(s) = S_c \sum_{i}^{N} \sum_{j \neq i}^{N} exp\left(- \frac{l_{ij}^2}{2} s^2 \right) |f_i(s)||f_j(s)| cos(\eta_i - \eta_j) \frac{sin(sk_s r_{ij})}{k_s r_{ij}} \qquad (64)$$

In the above equation, N denotes the number of atoms present in the cluster, S_c and k_s are the scaling factors for the amplitudes and distances, η_i and f_i are the phase and scattering amplitude of the elastic scattering factors [72]. r_{ij} is the inter atomic distances while l_{ij} is the mean vibrational amplitude. An averaged single value for every atom-pair type (Pt-Pt, Pt-D, D-D) was used for the latter. However, the scattering amplitude for the Pt is 20 times higher than D [73], thus dominating the scattering function. Therefore, the variation of the deuterium coverage can only be observed indirectly through the changes induced in the Pt core. The theoretical and experimental data was compared via a χ^2-fit by minimizing the weighted differences by variation of S_c, k_s, l_{Pt-Pt}, l_{Pt-D}, l_{D-D} and parameters of I_{back}. The degree of agreement between the experiment and the candidate structures was determined by the weighted profile factor [74] given by

$$R_w = \sqrt{\frac{\sum_k w_k (sM_k^{theo} - sM_k^{exp})^2}{\sum_k w_k (sM_k^{exp})^2}} \qquad (65)$$

The weighting factors denoted as w_k were calculated from the error propagated standard deviation of the experimental data.

Computational details

The initial search for structural models using semiempirical potential energy functions [75–77] within a genetic algorithm [78, 79] was carried out by PD. Detlef Schooss. The best fitting and lower energy isomers were then re-optimized using density functional theory (DFT) in TURBOMOLE (version 7.7) [80, 81] along with the RI-J (resolution of identity for the Coulomb term J) approximation [82, 83]. The cluster structures were optimized using the TPSS exchange-correlation functional [32] along with a def2-TZVP basis set [84]. Previously [64], the TPSS/def2-TZVP level of theory led to a good description of the structural parameters such as bond distances determined from the comparison of simulated and experimental scattering functions, and therefore was used in the present study. The 60 core electrons of the platinum atoms were replaced by the scalar relativistic effective core potential [85]. No symmetry restrictions were imposed on the cluster geometries during the geometry optimization. The effect of dispersion correction was analyzed using DFT-D3 with Becke-Johnson damping [86]. Vibrational frequencies of all the final cluster geometries were analyzed to verify that the structures are local minima.

The effect of spin-orbit coupling (SOC) for heavy elements was considered to obtain an accurate ground state structure [87, 88]. In previous works, the SOC contribution was seen to significantly impact the relative energies and the geometry of the bare Pt_n^- clusters [64]. Therefore, the lower energy structures were re-optimized using the relativistic two-component calculations [41] with TPSS functional and dhf-TZVP-2c basis set [89]. For details regarding the fitting procedure of the structures refer to Ref.[90]. All the low-energy and stable isomers presented here had a doublet or singlet spin state. In all the schematics shown in this Chapter, the grey color denotes Pt and white denotes deuterium atoms.

3.1. $Pt_nD_{2n}^-$ clusters

Various cluster sizes of $Pt_nD_{2n}^-$ ranging from n=6-13 were studied and compared to the experimental TIED data. For each cluster size, 10-15 cluster structures were analyzed. Only the most relevant and lowest energy structures which fit the experimental data best are described in the following sections. The other higher-lying isomers generated are shown in the Appendix.

3.1.1. $Pt_6D_{12}^-$ clusters

The stochiometry determined experimentally for the $Pt_6D_{12}^-$ cluster size is $Pt_6D_{12.4\pm1.4}$. The lowest energy isomers for $Pt_6D_{12}^-$ determined using TPSS/dhf-TZVP-2c computations are shown in Figure 5. The lowest energy isomer **1** has an incomplete pentagonal bipyramid as its Pt-core. It comprises five bridge-bound deuterium (D) atoms and seven deuterium atoms bound in an on-top position. Isomer **2** is higher in energy by 0.36 eV and has a (distorted) capped quadratic pyramid Pt-core structure. It consists of four bridged and eight on-top positioned deuterium atoms. Isomer **3**, 0.41 eV higher in energy, contains same Pt-core structure motif as **1** but with a different deuterium distribution.

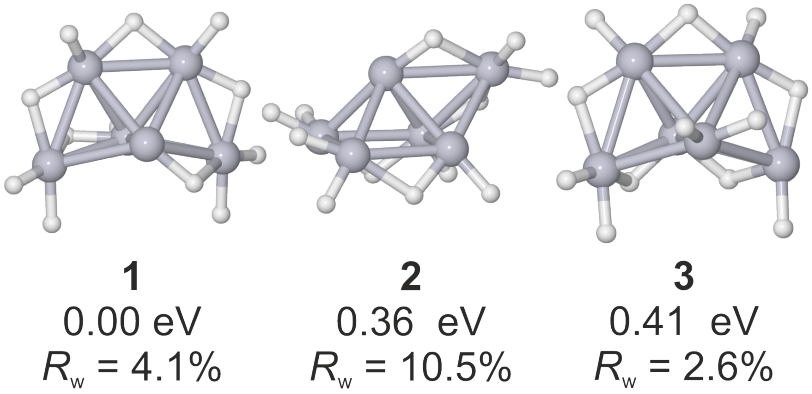

Figure 5.: Lowest energy isomers of $Pt_6D_{12}^-$ with relative energies computed at TPSS/dhf-TZVP-2c and experimental profile factor

Figure 6 shows the measured and calculated scattering functions of all three isomers. The plot supports the computation concerning the core motif. The theoretical scattering function of structure **1** and **3** fits the experimental data well (R_w=4.1 % , 2.6 %). In contrast, isomer **2** has a high R_w value and thus can be ruled out. Additionally, planar isomers (isomers 13-16, shown in the Appendix, Figure A.1.2, Table A.1.2) had a high profile factor compared to more symmetrical isomers showing a clear preference for the latter. However, as mentioned above, TIED is not sensitive to the exact number of deuterium atoms and their distribution on the surface. The symmetric D distribution on isomer **3** led to a more symmetric Pt-core structure (C_{2v}) which fits better to the experimental data. However, the effective symmetrization of the isomer can come from the experimental averaging of a static and dynamic isomer distribution. The contributions from different numbers of deuterium atoms such as $Pt_6D_{11}^-$ and $Pt_6D_{13}^-$ cannot be ruled out due to the large FWHM reported in the experiment. Therefore, additional calculations were carried out for $Pt_6D_{11}^-$ clusters by removing one D atom at a time from $Pt_6D_{12}^-$ isomer **1**. The best fitting $Pt_6D_{11}^-$ shown in Figure 7 (a), has a profile factor of 2.7 %. The higher-lying structures are given in the Appendix (Figure A.1.1, Table A.1.1). The $Pt_6D_{13}^-$ cluster was generated by placing one D atom in an on-top position as seen in Figure 7 (b) and has a R_w value of 4.62 %. The Pt-core of the lowest energy and best fitting $Pt_6D_{11}^-$ and $Pt_6D_{13}^-$ have a similar Pt-core as isomers **1** / **3** of $Pt_6D_{12}^-$ and reasonable profile

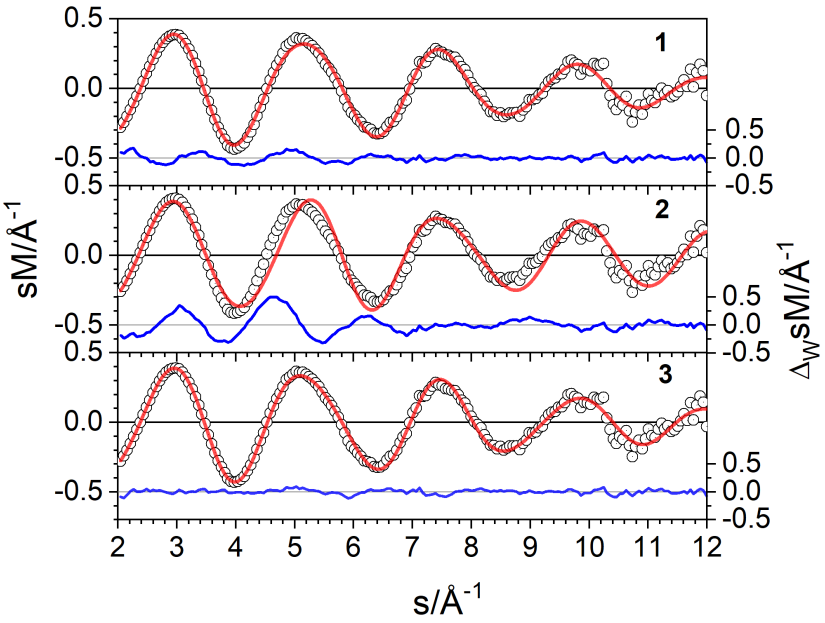

Figure 6.: Comparison of experimental (circles) and simulated (red line) modified molecular scattering intensities sM of $Pt_6D_{12}^-$ for the isomers **1**-**3**. The blue line in each panel shows the weighted residuals [Figure was provided by D. Schooss].

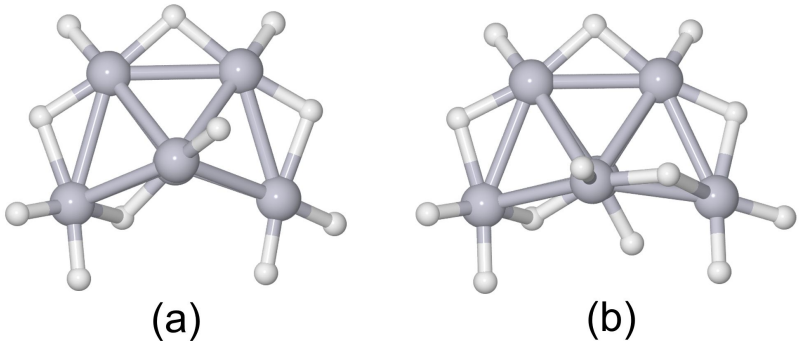

Figure 7.: Lowest energy isomers of (a) $Pt_6D_{11}^-$ with an experimental profile factor of R_w=2.7 %, (b) $Pt_6D_{13}^-$ with an experimental profile factor of R_w=4.62 %. These structures are computed at TPSS/dhf-TZVP-2c level of theory.

factors. Therefore, their contribution to the TIED data cannot be ruled out. However, all structures consisting of Pt-cores different from **1** / **3** can be ruled out.

3.1.2. $Pt_7D_{14}^-$ clusters

The experimentally determined stochiometry for a Pt_7 core is $Pt_7D_{14.2\pm0.5}$. The lowest energy structures of $Pt_7D_{14}^-$, optimized using TPSS/dhf-TZVP-2c are shown in Figure 8. The Pt-core structure of isomer **1** is a double-capped square pyramid comprising five bridge-positioned D atoms. Isomer **2** is higher in energy by 0.41 eV compared to **1**. The Pt-core structure of **2** is a pentagonal bipyramid (*pbp*) consisting of five bridge and on-top positioned D atoms along the perimeter of the isomer. Isomer **3** contains a distorted capped square pyramid Pt-core with a higher relative energy of 0.5 eV. Isomers having the same Pt-core structure of isomer **1** and **2** with variation in D distributions are also generated. However, they are higher in energy (>0.3 eV). The structures and their relative stabilities are given in Appendix (Figure A.1.3, Table A.1.3).

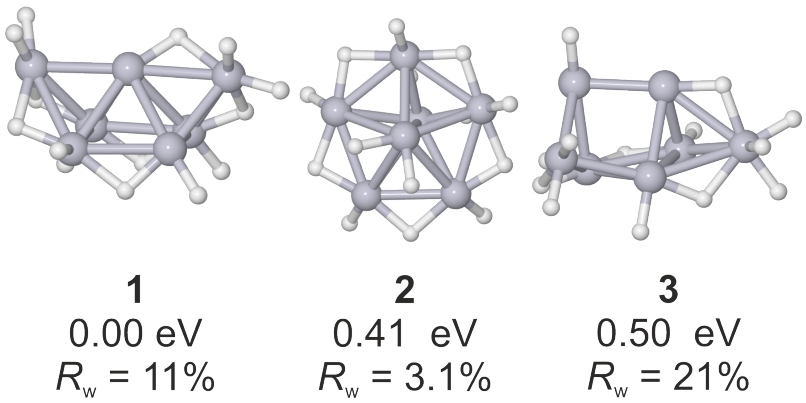

Figure 8.: Lowest energy isomers of $Pt_7D_{14}^-$ with relative energies computed at TPSS/dhf-TZVP-2c and the experimental profile factor

The comparison of experimental and simulated scattering data is shown in Figure 9. Isomer **1** can be ruled out while *pbp* Pt-core structure of **2** fits well to the TIED data with R_w=3.1 %. Other core structures can be ruled out. The higher-lying isomers of **2** (shown in Appendix section Table A.1.3) also have similar profile factors and thus can contribute to the TIED data. This probability cannot be ruled out experimentally. While isomer **3** can be neglected due to its high-profile factor.

3.1.3. $Pt_8D_{16}^-$ clusters

The experimentally determined stoichiometry for Pt_8-core was $Pt_8D_{15.8\pm0.6}$ and $Pt_8D_{16}^-$ was chosen as stochiometry for the candidate structures. As seen in Figure 10, isomer **2** contains a Pt-core of a distorted hexagonal bipyramid while Pt-core of **3** can be described as a capped *pbp*. The global minimum structure of isomer **1** has a Pt-core which is a distorted version of either isomer **2** or **3**, the latter are higher in energy by 0.19 and 0.29 eV respectively. The deuterium distribution of isomers **1**, **2** and **3** contain 6, 8, and 7 bridge positioned D atoms, respectively.

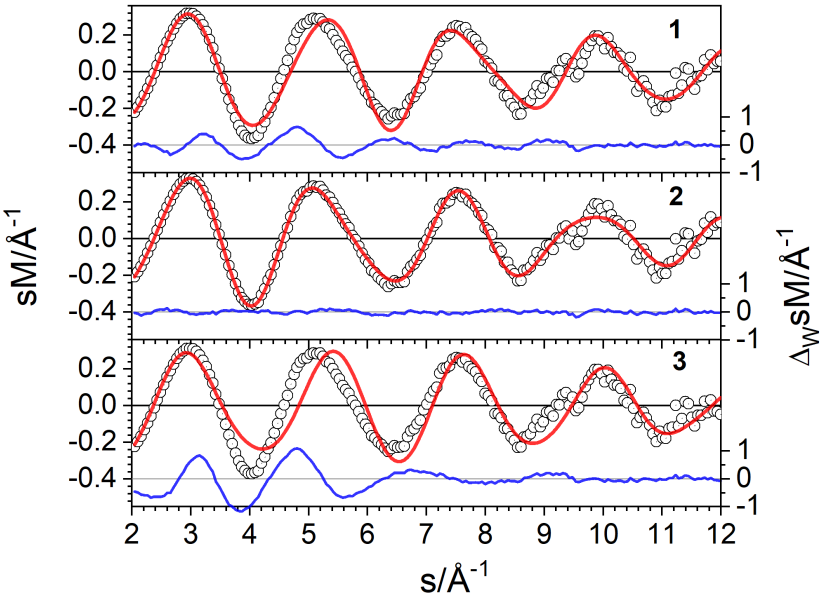

Figure 9.: Comparison of experimental (circles) and simulated (red line) modified molecular scattering intensities sM of $Pt_7D_{14}^-$ for the isomers **1**-**3**. The blue line in each panel shows the weighted residuals [Figure was provided by D. Schooss].

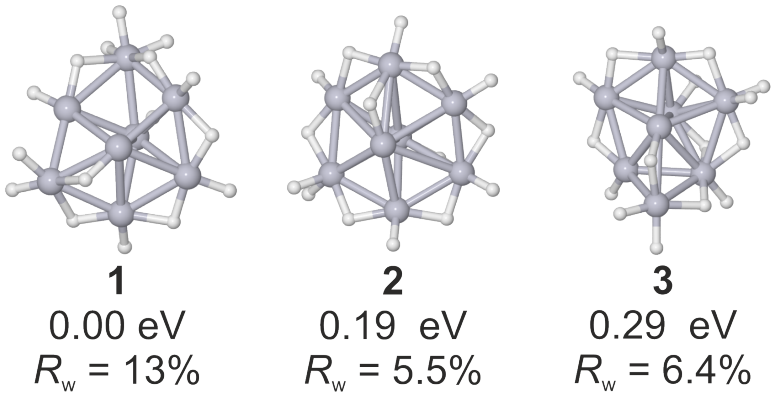

Figure 10.: Lowest energy isomers of $Pt_8D_{16}^-$ with relative energies computed at TPSS/dhf-TZVP-2c and experimental profile factor

The experimental and simulated scattering functions of all three isomers shown in Figure 11 reveal that isomer **2** with a profile factor of R_w=5.5 % fits best with the TIED data. Isomer **3** shows the second best match with R_w=6.4 %. The lowest energy isomer **1** can be ignored due to the high profile factor. The mixture of isomer **2** (70%) and **3** improved the profile factor to 4.7 %. Additionally, isomers generated with different Pt-core structures and D configurations have higher relative energies and profile factors and therefore are neglected (shown in Appendix Figure A.1.4, Table A.1.4).

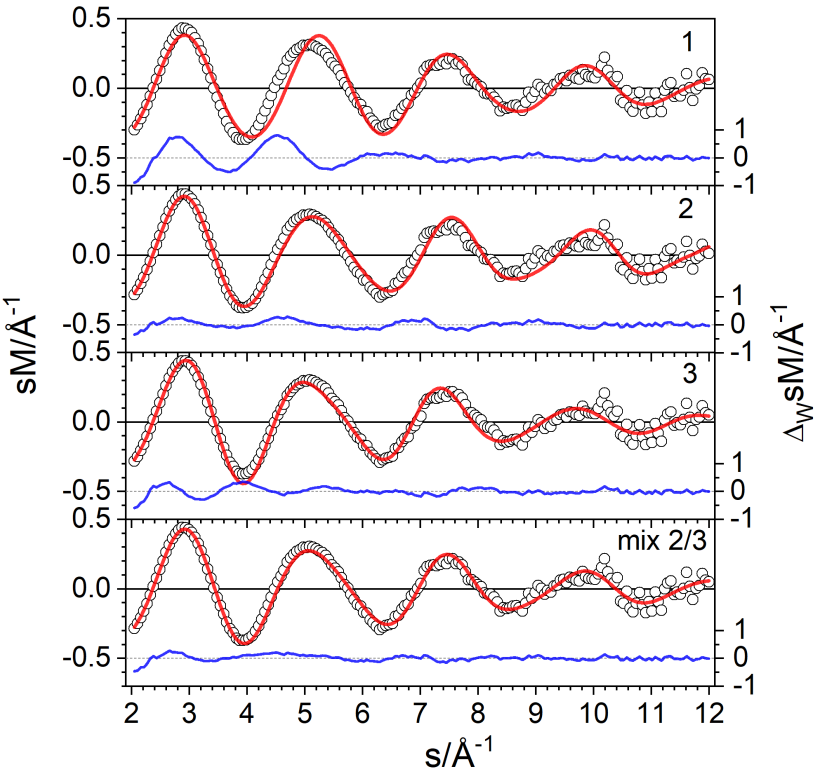

Figure 11.: Comparison of experimental (circles) and simulated (red line) modified molecular scattering intensities sM of $Pt_8D_{16}^-$ for the isomers 1-3. The blue line in each panel shows the weighted residuals [Figure was provided by D. Schooss].

3.1.4. $Pt_9D_{18}^-$ clusters

The experimentally determined stochiometry for a Pt_9 core is $Pt_9D_{18.0\pm0.3}$. Therefore, the corresponding $Pt_9D_{18}^-$ stoichiometry was chosen for the candidate structures. Two low energy isomers computed at TPSS/dhf-TZVP-2c level of theory are shown in Figure 12. The global minimum isomer **1** is a C_{2v} cupola with a bent seven atom hexagonal base covered by a Pt-dimer above. It comprises of eight Pt atoms at edge consisting of one on-top D atom each and nine shared D bridges. One D atom remaining is present in the hollow site at the base. Other investigated deuterium distributions are higher in energy (> 0.3 eV) (shown in Appendix Figure A.1.5, Table A.1.5). Isomer **2** is higher in energy by 0.41 eV and is a distorted version of **1** in which one of the Pt-Pt bonds of the hexagonal base is opened forming a capping triangle.

Comparing the experimental and simulated scattering functions (Figure 13) show that structure **1** fits well with the TIED data. There is a possibility of contributions from other deuterium distributions. The higher lying isomer **2** gives a better fit due to its lower profile factor compared to isomer **1**.

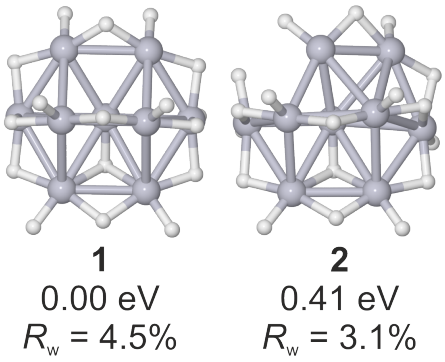

Figure 12.: Lowest energy isomers of $Pt_9D_{18}^-$ with relative energies computed at TPSS/dhf-TZVP-2c and the experimental profile factor

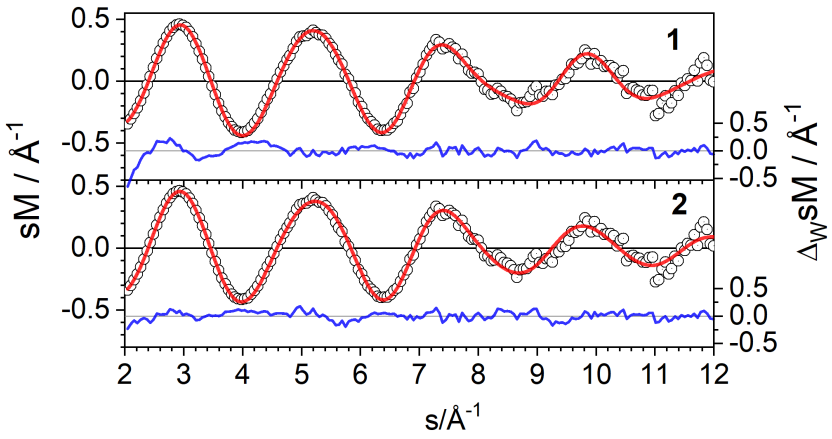

Figure 13.: Comparison of experimental (circles) and simulated (red line) modified molecular scattering intensities sM of $Pt_9D_{18}^-$ for the isomers 1-2. The blue line in each panel shows the weighted residuals [Figure was provided by D. Schooss].

3.1.5. $Pt_{10}D_{20}^-$ clusters

The stochimetry for the Pt_{10} core determined experimentally is $Pt_{10}D_{19.7\pm0.2}$ corresponding $Pt_{10}D_{20}^-$ as the most probable stochiometry for the candidate structure. Figure 14 shows two isomers of $Pt_{10}D_{20}^-$. The low energy isomer **1** contains a C_{3v}-symmetric core and forms a triangular cupola and is a hemisphere of a 13 atom cuboctahedron. Isomer **1** has 14 bridging D atoms and 6 on-top D atoms. The next higher-lying isomers consisting of the same core structure but varying D distributions start at 0.16 eV compared to **1** (shown in Appendix section Figure A.1.6, Table A.1.6). The next higher-lying isomer with a different Pt-core structure is isomer **2**. It is a bicapped cube and has 12 bridged and 8 on-top D atoms.

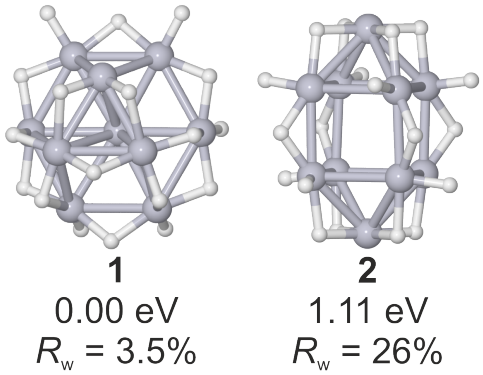

Figure 14.: Lowest energy isomers of $Pt_{10}D_{20}^-$ with relative energies computed at TPSS/dhf-TZVP-2c and the experimental profile factors

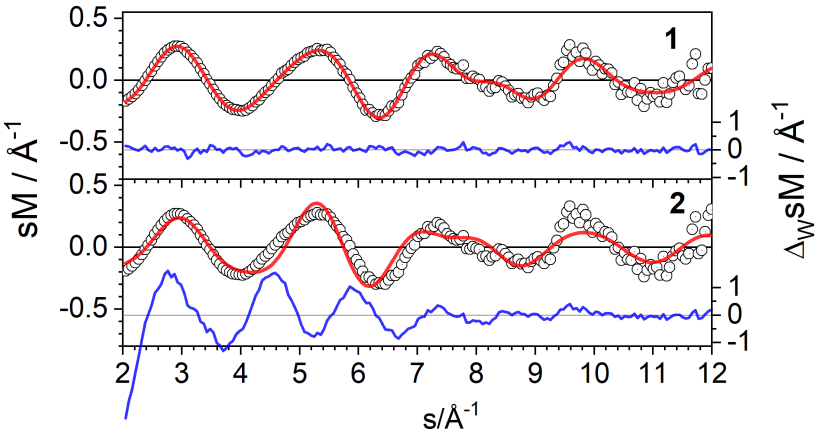

Figure 15.: Comparison of experimental (circles) and simulated (red line) modified molecular scattering intensities sM of $Pt_{10}D_{20}^-$ for the isomers 1 and 2. The blue line in each panel shows the weighted residuals [Figure was provided by D. Schooss].

The comparison of experimental and simulated scattering functions shows that the scattering function of the trigonal cupola **1** fits well with the TIED data. Contributions from isomers with the same core structure with different deuterium distributions cannot be ruled out (please refer to Appendix section Table A.1.6). Due to the high profile factor of isomer **2**, it can be neglected. Thus, the core structure of **1** is assigned to $Pt_{10}D_{20}^-$.

3.1.6. $Pt_{11}D_{22}^-$ clusters

The stoichiometry determined experimentally for a Pt_{11} core structure is $Pt_{11}D_{21.8\pm0.6}$. Figure 16 shows the lowest energy structures for $Pt_{11}D_{22}^-$. The Pt-core of isomer **1** is a tri-capped cube and is related to $Pt_{10}D_{20}^-$ **2** structure where one Pt-atom is added to the open cube facet. It consists of all D atoms in bridge positions along the edges of the Pt

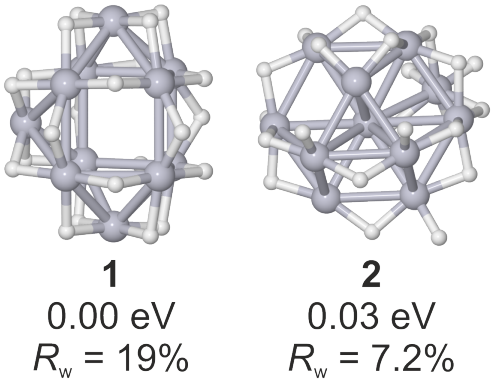

Figure 16.: Lowest energy isomers of $Pt_{11}D_{22}^-$ with relative energies computed at TPSS/dhf-TZVP-2c and experimental profile factors.

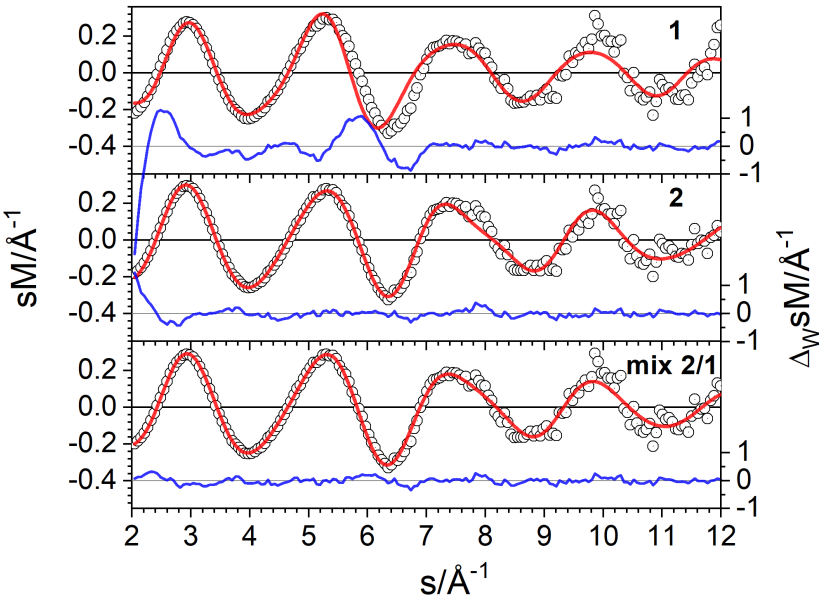

Figure 17.: Comparison of experimental (circles) and simulated (red line) modified molecular scattering intensities sM of $Pt_{11}D_{22}^-$ for the isomers 1-3. The blue line in each panel shows the weighted residuals [Figure was provided by D. Schooss].

core. The Pt-core of isomer **2** is generated by the addition of one Pt-atom to the base of $Pt_{10}D_{20}^-$ structure **1**. It consists of 14 bridge-bound D atoms and 8 on-top bound D atoms. Both the isomers are isoenergetic within the TPSS/dhf-TZVP-2c error.

The best fit to the TIED data is obtained for isomer **2** consisting of capped trigonal cupola with a profile factor of R_w=7.2 %. Isomer **1** has a higher profile factor and can be ruled out. However, there is a probability of its small contribution to the probed ensemble as the mixture fit of **2** with ≈23% of **1** leads to a significant decrease in the

profile factor to R_w=4.3 %. Additionally, the relative energies and profile factors for the higher-lying $Pt_{11}D_{22}^-$ isomers are given in Appendix (Figure A.1.7, Table A.1.7).

The analysis of $Pt_{12}D_{24}^-$ isomers is described in-detail in Chapter 3.2.

3.1.7. $Pt_{13}D_x^-$, x=24,25,26 clusters

The deuterium coverage determined experimentally for the Pt_{13} core is $Pt_{13}D_{24.6\pm0.8}$. Additional to the most probable stochiometry for the candidate structure, $Pt_{13}D_{25}^-$, computations with 24 and 26 D atoms were also performed to investigate if these structures have a contribution to the TIED data. The $Pt_{13}D_{24}^-$ structure contains a cuboctahedral cage structure with all deuterium atoms bound in the bridge position with additional Pt atom filling the empty void of the cage structure (Figure 18).

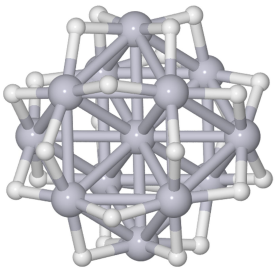

Figure 18.: $Pt_{13}D_{24}^-$ cluster consisting of all bridge positioned deuterium atoms and computed at at TPSS/dhf-TZVP-2c.

To construct the higher coverage structures, $Pt_{13}D_{25}^-$ and $Pt_{13}D_{26}^-$ with additional deuterium coverage, the D atoms had to be positioned in an on-top configuration. This leads to different isomers of which only the stable ones are shown. Three isomers of $Pt_{13}D_{26}^-$ are shown in Figure 19. Isomer **1** is the lowest energy structure consisting of 23 bridge and 3 on-top D atoms with a profile factor of 4.5 %. However, isomer **2** which features a different deuterium configuration has a lower profile factor of R_w=3.7%. It is 0.42 eV higher in energy with 21 bridge and 5 on-top D atoms. Other core motifs such as anti-cuboctahedron of isomer **3** are also generated but can be ruled out due to higher relative energy and profile factor. Additionally, structures of $Pt_{13}D_{26}^-$ isomer and their profile factors are given in Appendix (Figure A.1.8, Table A.1.8).

Various $Pt_{13}D_{25}^-$ isomers were generated by removing one deuterium atom at a time from $Pt_{13}D_{26}^-$ isomers **2** and **3**. $Pt_{13}D_{25}^-$ isomers **1** and **2** show a cuboctahedral motif while isomer **3** has a anti-cuboctahedral motif (shown in Figure 21). The profile factor of the lowest energy isomer **1** is 4.52 % and that of isomer **2** is further lowered to 3.5 % (Figure 21) but is higher in energy by 0.52 eV compared to **1**. Isomer **3** is higher in energy by 0.56 eV and also has a higher profile factor of 7 % and therefore can be ruled out. There

are several isoenergetic isomers to **1** present in a small energy gap showing that the removal of one deuterium atom does not reflect significant changes in their relative energies (see in Appendix Table A.1.9). However, these isomers can be ignored due to their high profile factor.

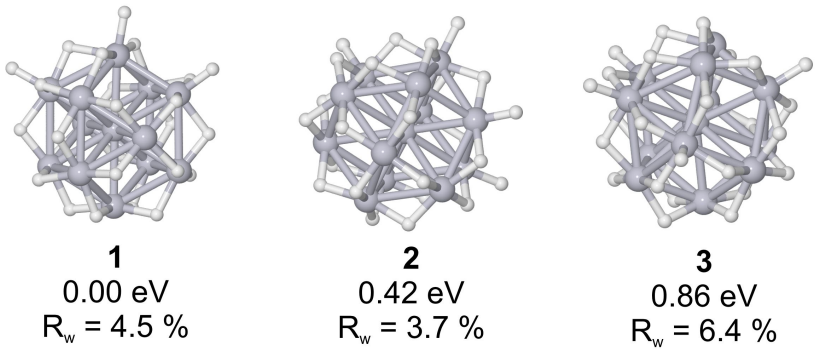

Figure 19.: Lowest energy isomers of $Pt_{13}D_{26}^-$ with relative energies computed at TPSS/dhf-TZVP-2c and experimental profile factors.

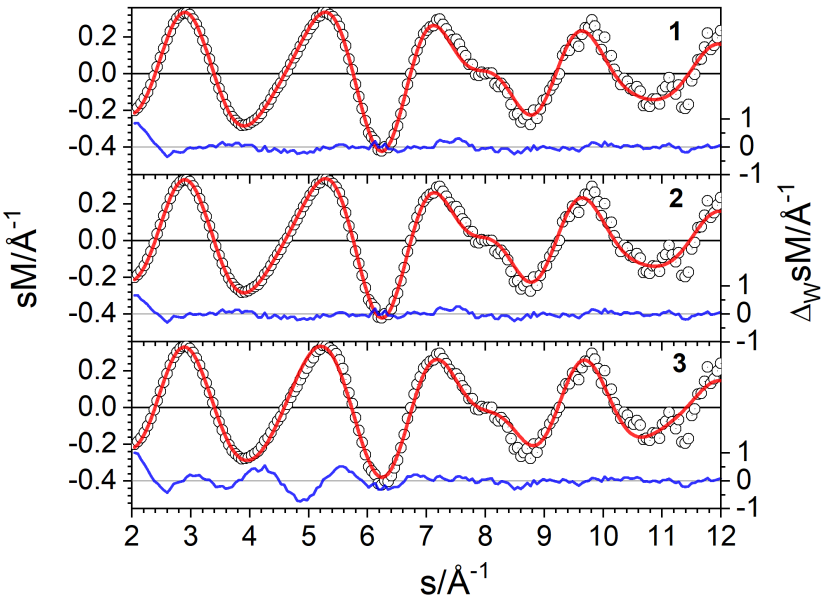

Figure 20.: Comparison of experimental (circles) and simulated (red line) modified molecular scattering intensities sM of $Pt_{13}D_{26}^-$ for the isomers 1-3. The blue line in each panel shows the weighted residuals [Figure was provided by D. Schooss].

As mentioned previously, TIED cannot determine the position of the deuterium atoms on the cluster surface, and is indirectly detected by the change in the Pt core structure, therefore the exact number of deuterium atoms is an estimate of ±1 D atom of the total number of indirectly detected D atoms. Also, deuterium atoms are mobile on the surface

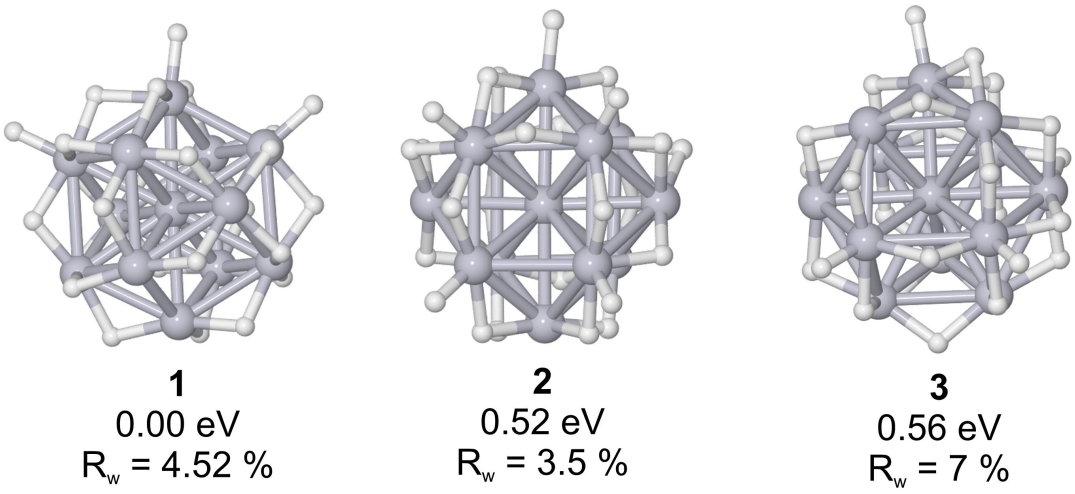

Figure 21.: Lowest energy isomers of $Pt_{13}D_{25}^-$ with relative energies computed at TPSS/dhf-TZVP-2c and experimental profile factors.

and are non-trivial to detect on the time scale of a few seconds also cannot detect the meta-stable intermediates. Therefore, the probable contribution of other $Pt_{13}D_{24}^-$ and $Pt_{13}D_{25}^-$ clusters to the TIED data cannot be ignored. Thus, the isomers containing other than cuboctahedral structure of Pt core can be neglected.

3.1.8. Discussion

Figure 22 shows a summary of all the structure motifs assigned to the respective cluster size of $Pt_nH_{2n}^-$ (n=6-13). It is worthwhile to perform a comprehensive comparison between bare Pt_n^- (given in ref. [64]) with $Pt_nD_{2n}^-$ structures to further deduce the evolution of the cluster structure while taking into account the impact of deuterium adsorption on the Pt-core structure. Starting with the Pt_6 core structure, the lowest energy isomer of bare Pt_6^- structure is observed to be planar along with D_{3h} symmetry. Upon deuterium interaction, the Pt_6 core transforms into a 3D incomplete pentagonal bipyramid (*pbp*) motif showing that Pt core atoms prefer higher coordination with deuterium adsorption. The best fitting bare Pt_7^- isomer to TIED data is a quasi-planar distorted hexagon with D_{3d} symmetry while it prefers a pentagonal bipyramid (*pbp*) core structure when in contact with the deuterium atoms. Furthermore, the bare Pt_8^- isomer is seen to prefer a 3D motif consisting of connected trigonal and square pyramids while $Pt_8D_{16}^-$ favors a mixture of a distorted hexagonal bipyramid and *pbp*. Thus, the local minima of Pt_6^-, Pt_7^- and Pt_8^- consisted of amorphous-like structures which evolved into 3D structures upon deuterium adsorption. It can be seen in ref. [64] that the Pt-core structures from Pt_9^- formed a 3D structure consisting of a tetrahedral structure which persisted until Pt_{13}^- motif. However, these Pt-core motifs transformed into higher symmetries upon

interaction with deuterium atoms. The development of spherical geometries starts from the $Pt_{11}D_{22}^-$ structure consisting of a spherical triangular cupola with a C3*v* core structure until the stable cuboctahedral structure of $Pt_{13}D_{26}^-$. The structural analysis of these motifs also showed a clear preference for bridged-positioned deuterium atoms compared to the on-top bound ones [90] (This is discussed in detail in Chapter 3.2) . The spin-states were also seen to be quenched from higher spin states seen in bare Pt_n^- [64] to the doublet or singlet spin state in $Pt_nD_{2n}^-$ isomers. Along with the above-mentioned low-energy best-fitting isomers, various other isoenergetic and mixtures of neighboring motifs with different deuterium configuration were also found contributing to the TIED data, indicating the dynamicity of the deuterium shell. However, TIED cannot determine the deuterium positions on the surface. The structural motifs predicted at TPSS/dhf-TZVP-2c level of theory predict the best-fitting and experimentally found core structure except for the $Pt_7D_{14}^-$ ensemble where the best-fitting *pbp* isomer is 0.41 eV higher in energy compared to the predicted ground state isomer.

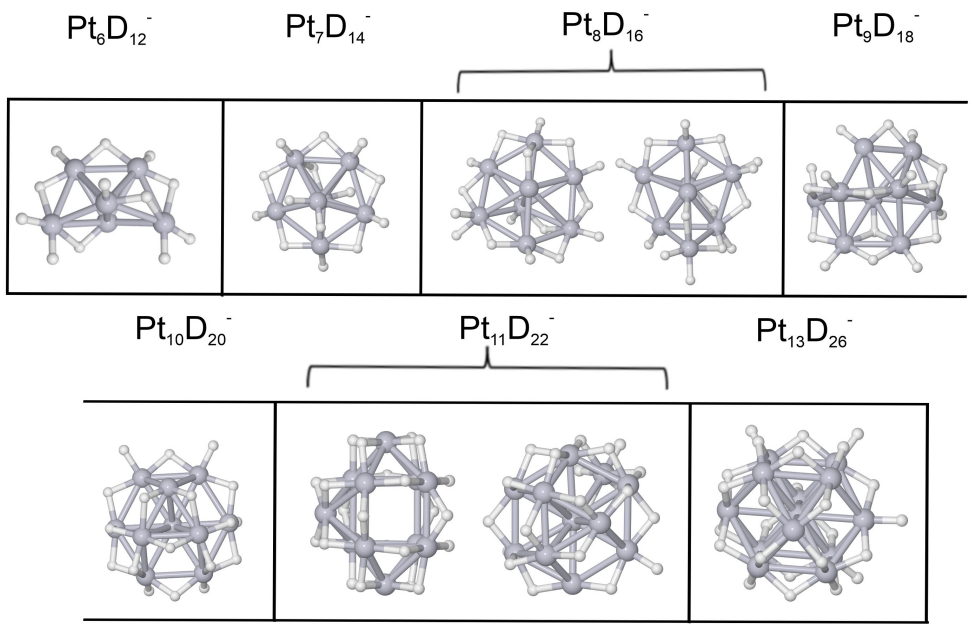

Figure 22.: Assigned structures for $PtnD_2n^-$ (n=6-13), mixtures of two isomers were necessary to fit the TIED data.

3.1.9. Conclusion

Various sizes of anionic $Pt_nD_{2n}^-$ (n=6-13) clusters were investigated using density functional theory with the inclusion of spin-orbit coupling. The computed structures were further compared with the trapped ion electron diffraction (TIED) data using the weighted

profile factor. The results showed that deuterium adsorption significantly influences the Pt-core structures. As the Pt cluster size increases from $Pt_6D_{12}^-$ towards $Pt_{13}D_{26}^-$, it is observed that the number of bridge-bound deuterium atoms increases concurrently, developing into a more spherical geometry. The results also showed that the symmetry of the clusters gradually increased with the cluster size from the distorted structures at $Pt_6D_{12}^-$ configuration towards spherical triangular cupola for $Pt_{10}D_{20}^-$ towards the cuboctahedral structure of $Pt_{13}D_{26}^-$ configuration. This clearly shows the preference of the Pt core atoms for a high coordination number. Contributions from other local minimum structures to the TIED data cannot be ruled out.

3.2. $Pt_{12}D_{24}^-$ clusters

Among platinum deuterides $Pt_{(6-13)}H_{(12-26)}^-$, $Pt_{12}H_{24}^-$ clusters are a special cluster configuration. In the TIED experiment, the generation of a stable cuboctahedral cage structure was predominantly seen. The previous study carried out on bare Pt_{12}^- clusters [64] showed that it preferred a doubly truncated trigonal bipyramid configuration. Thus, in this study, an in-detail theoretical investigation was carried out to examine the influence of deuterium exposition of Pt_{12}^- on its structure in the gas phase and unravel the possible reasons for the high stability of the $Pt_{12}H_{24}^-$ cluster. We also studied the cluster's characteristic properties such as structure, bonding character, effect of spin-orbit coupling, and electronic properties that can influence cluster stability. Finally, the influence of the cluster magic number was checked.

3.2.1. Computational details

A thorough examination of the structural and electronic characteristics of the three best-fitting cluster structures for $Pt_{12}D_{24}^-$ isomers was conducted. The relative energies reported in this chapter were corrected by the zero- point energies. The Gibbs free energy correction to the DFT energy was calculated at T=120 K and 0.44 mbar. The Nudged elastic band (NEB) method [52] was used for determining the reaction pathway and corresponding activation barriers. The d-band center of all surface Pt atoms of the three isomers was calculated using the Mulliken population analysis of the *d*-orbitals ($n_\alpha(\epsilon)$) using the following formula:

$$\epsilon_d = \frac{\sum_\alpha \sum_\epsilon \epsilon n_\alpha(\epsilon)}{\sum_\alpha \sum_\epsilon n_\alpha(\epsilon)}, \tag{66}$$

where ϵ is the molecular orbital energy and α sums over the selected surface Pt atoms. The charge and nature of the chemical bonds were assessed using natural orbital population analysis [91] and Wiberg bond indices [92]. The presence of spherical aromaticity was determined using the Nucleus Independent Chemical shift (NICS) value [93]. The Fermi level in the Density of States plot was chosen at the energy of the highest occupied orbital. The orbital energies were broadened by Gaussians (0.272 eV FWHM).

3.2.2. Results and Discussion

3.2.2.1. Structural analysis

Three distinct Pt core structures were chosen for additional deuterium configuration optimization based on the comparison of simulated and experimental scattering data. The effect of spin-orbit coupling (SOC) contributions on the cluster geometry and on their

relative energies was analyzed. Figure 23 shows the three best-fitting cluster structures optimized using a relativistic two-component method with the TPSS functional and dhf-TZVP-2c basis set.

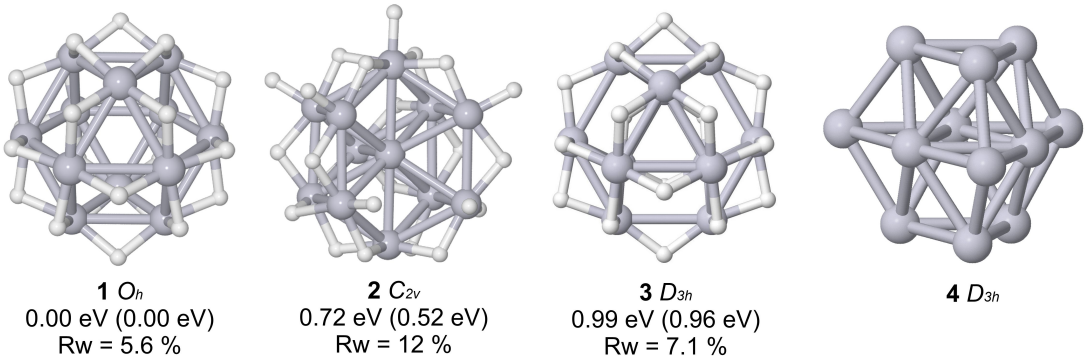

Figure 23.: Computed structures of $Pt_{12}D_{24}^{-}$ isomers **1**-**3** with the approximate point group symmetry for the Pt-core, relative energy for TPSS/def2-TZVP (2C-TPSS/dhf-TZVP-2c), and experimental profile factors. Structure **4** shows the bare cluster Pt_{12}^{-} taken from ref. [64] (Reproduced from S. Gojare *et al.* [90] (2024), *ChemPhysChem* under the terms of the CC-BY license).

Among them, the most stable cluster structure is structure **1**. It is a cuboctahedral cage structure. All 24 deuterium atoms occupy the bridge position making 24 Pt-D-Pt bonds and forming O_h symmetry. The configurations consisting of on-top positioned D atoms are stable as well. However, they are higher in energy (> 1.1 eV) as seen in Figure 24.

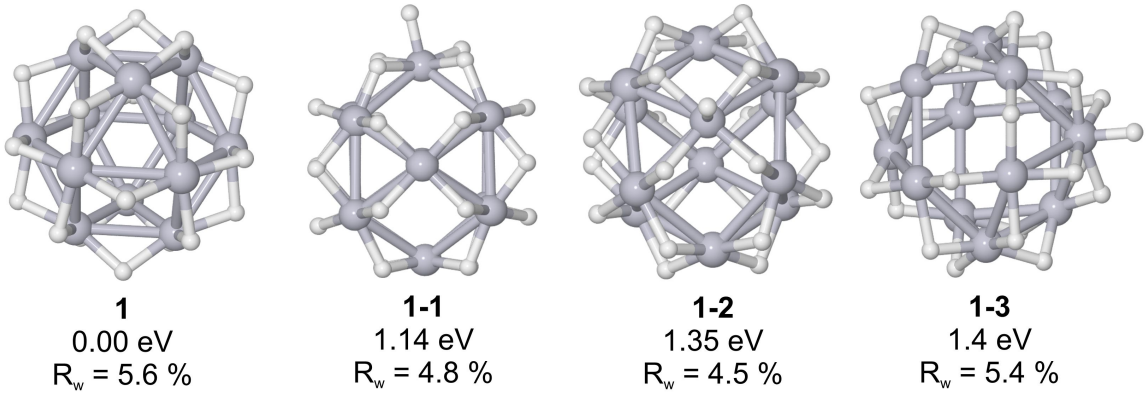

Figure 24.: Relative energies (eV) and profile factors (R_w (%) computed for higher lying isomers generated from isomer **1** with one on-top positioned deuterium atom. All computations carried out with TPSS/def2-TZVP.

The isomer **2** is 0.72 eV higher in energy compared to **1**. Its Pt-core structure is an incomplete cuboctahedron with one Pt atom missing from the cuboctahedral shell, thus forming a C_{2v} symmetry for the Pt-core. Several deuterium configurations with different distributions of bridge and on-top bound deuterium atoms were found which were close in energy (see Table A.2.1 and Figure A.2.1 in Appendix section). The most stable and lowest energy structure within this ensemble is shown in Figure 23. This structure consists of 18 bridge and 6 on-top bound deuterium atoms.

Isomer **3** is also a spherical cage similar to **1** but one of the bottom triangles is rotated by 60° making it an anti-cuboctahedral cage structure with approximate D_{3h} symmetry. All deuterium atoms are bound in bridge positions similar to isomer **1**. The relative energy of isomer **3** is 0.99 eV. Different deuterium configurations of **3** with on-top bound deuteriums were generated. However, these led to a significant core reconstruction. Thus, the configuration with all D atoms bound in the bridge position is the stable one found.

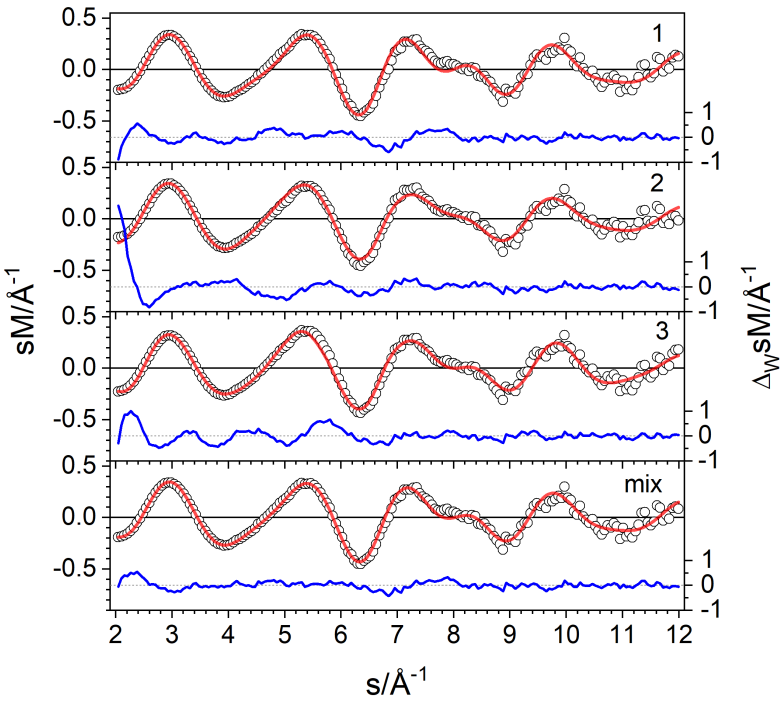

Figure 25.: Comparison of experimental (circles) and simulated (redline) modified molecular scattering intensities *sM* of $Pt_{12}D_{24}^-$ for the isomers **1**-**3** and a mixture of 80% isomer **1** and 20% isomer **2**. The blue line in each panel shows the weighted residuals (Reproduced from S. Gojare *et al.* [90] (2024), *ChemPhysChem* under the terms of the CC-BY license).

Structurally, the Pt cores of isomer **1** and **2** belong to the same motif as a variation in occupation of different positions of a 13-atom cuboctahedron. In the isomer **3** structure, the layer order is modified from fcc to hcp stacking compared to **1**. Thus, their molecular scattering functions are expected to be similar. However, Figure 25 shows that the molecular scattering function of isomer **1** fits well with a profile factor of R_w = 5.6 % to the TIED experiment. Other D configurations of isomer **1** consisting of mixed bridge and on-top bound D atoms show lower profile factors but can be excluded due to their high relative energies (Figure 24). The R_w values of isomers **2** and **3** are significantly higher, 12 % and 7.1 % respectively. The difference in R_w values of **1** and **2** is due to the specific deviation in the electron momentum transfer (**s**) range caused by the cage structure of **1** in the experiment. This is amplified by the large statistical weighting in this region (blue line in Figure 25). Thus, isomer **1** is the primary contributor of the ensemble probed in the experiment. However, a small contribution from isomer **2** cannot be ruled out as the mixture of 80 % **1** and 20 % **2** reduces the R_w value to 4.3 % (Figure 25). Due to the different close-lying deuterium configurations of isomer **2**, those lead to similar results in the mixture fits.

The influence of different charges on the cluster structure were examined by reoptimizing the neutral $Pt_{12}D_{24}$, cationic $Pt_{12}D_{24}^{+}$ and dianionic $Pt_{12}D_{24}^{2-}$ isomers (Table 1). The results show that the charge does not affect the structural changes. However, the energetic order is affected where isomer **1** is still the most stable structure for neutral and dianionic clusters. Isomer **2** is the lowest energy structure within cationic structures.

Table 1.: Comparison of relative energy *E* (TPSS/def2-TZVP) for different charge states of isomer **1**-**3**. All values are zero point energy corrected (values in the brackets denote the relative contribution of ZPE) (Reproduced from S. Gojare *et al.* [90] (2024), *ChemPhysChem* under the terms of the CC-BY license).

Isomer	$Pt_{12}D_{24}^{-}$ (*E*/eV)	$Pt_{12}D_{24}$ (*E*/eV)	$Pt_{12}D_{24}^{+}$ (*E*/eV)	$Pt_{12}D_{24}^{2-}$ (*E*/eV)
1	0	0	0.44 (-0.005)	0
2	0.72 (-0.052)	0.31 (0.03)	0	1.2 (-0.144)
3	0.99 (-0.072)	1.05 (-0.08)	1.41 (-0.118)	0.94 (-0.063)

The SOC effect on the anionic $Pt_{12}D_{24}^{-}$ clusters shows that SOC decreases the relative energy differences while the energetic order remains the same. The bond length between Pt atoms of isomer **1** decreased from 2.716 to 2.702 Å after SOC was included. This is in agreement with previous studies [23, 94, 95]. The relative energy differences of the isomers are not considerably affected by taking into account the finite experimental temperature or the dispersion corrections (Table 2).

Table 2.: Comparison of the relative energies of isomers **1**-**3** for TPSS/def2-TZVP, 2C-TPSS/dhf-TZVP-2c, the dispersion corrections, and relative of the relative difference of zero point energy and free Gibbs energy (G). The contribution of the relative zero point energy is given in parentheses (Reproduced from S. Gojare *et al.* [90] (2024), *ChemPhysChem* under the terms of the CC-BY license).

Isomer	TPSS/def2-TZVP	2C-TPSS/dhf-TZVP-2c	disp. corr. /eV (2C)	*G*/eV (2C)
1	0	0	-5.03	0
2	0.72 (-0.052)	0.52 (-0.053)	-5.05	0.003
3	0.99 (-0.071)	0.96 (-0.018)	-5.00	-0.006

The different close-lying deuterium configurations of isomer **2** indicate the dynamical nature of the deuterium shell. The mobility of the deuterium atoms can be analyzed through the activation barriers connected to their binding mode. The activation barriers were calculated using the nudged elastic band (NEB) method. The activation barriers calculated for different configurations are in the range of 0.5 eV. A sequential rearrangement of deuterium atoms on the surface of isomer **2** can induce the transformation to isomer **1**. The reaction pathway is shown in Figure 26. For this isomer transformation, six consecutive steps are required coupling the deuterium mobility and the core isomerization. An overall activation barrier of 1.4 eV is calculated. These results demonstrate that at the experimental condition, an isomerization in the structure ensemble of **2** is possible. But the dynamic interconversion between isomer **1** and **2** is not possible. The inclusion of SOC contributions does not affect the activation barrier.

The reason for the stability of the cuboctahedral cage structure is further analyzed energetically by dividing the structure into two parts: (i) the Pt core structures, (ii) the respective deuterium shell and determining their respective contributions. To examine the contribution of the Pt-core structure, all the deuterium atoms were removed from the surface and the energy (single point) of the core structure (Pt_{12}^-) was recalculated. The results show that the core structure of isomer **2** is the most stable configuration due to the high mean Pt coordination number (CN=5.16) while the coordination number of the cage structure of isomer **1** and **3** is just CN=4.00. This leads to a destabilization of 0.43 and 1.16 eV for the cage structures **1** and **3**. The bare Pt_{12}^- core structure reported here of isomers **1**-**3** are however not the stable configurations as can be seen in ref. [64].

The contribution of the deuterium shell is evaluated by the mean and maximum adsorption energy using the following equations 68 , and 67:

$$E_{ads}^{mean} = \frac{1}{24}\left(E_{Pt_{12}D_{24}^-} - E_{Pt_{12}^-} - 12E_{D_2}\right), \tag{67}$$

$$E_{ads}^{max} = E_{Pt_{12}D_{24}^-} - E_{Pt_{12}D_{23}^-} - \frac{1}{2}E_{D_2}. \tag{68}$$

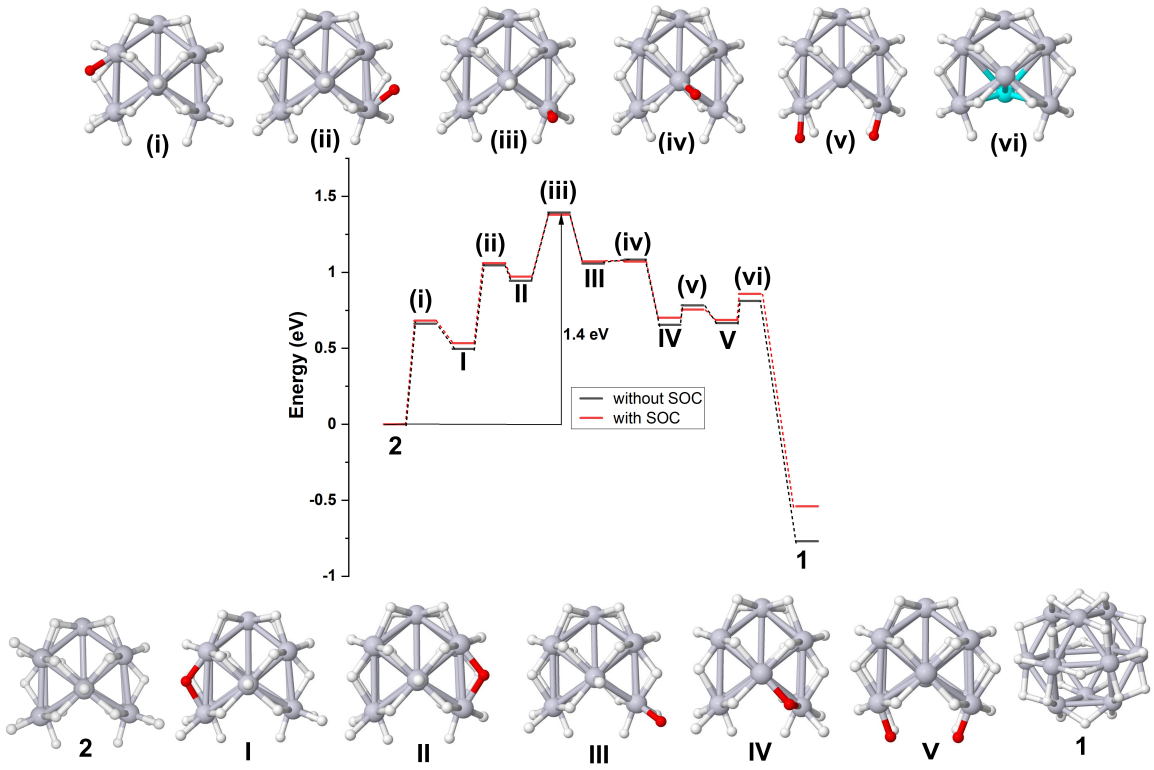

Figure 26.: A reaction pathway describing the conversion of isomer **2** to **1** with and without the inclusion of spin-orbit coupling effect. The deuterium atoms in red and the platinum atom in cyan color denote the ones whose positions are changed. Note that electronic energies are given relative to isomer **2** (Reproduced from S. Gojare *et al.* [90] (2024), *ChemPhysChem* under the terms of the CC-BY license).

Table 3.: Deuterium adsorption energies (eV) (Reproduced from S. Gojare *et al.* [90] (2024), *ChemPhysChem* under the terms of the CC-BY license).

Isomer	$E_{ads}{}^{mean}$	E_{ads}	
		Bridge	On-top
1	-0.50	-1.20	-
2	-0.48	-1.22 - -0.33	-0.55 - -0.23
3	-0.46	* (led to structure reconstruction)	-

The $E(Pt_{12}^{-})$ is the energy of a stable isomer obtained from Ref. [64]. The highest mean adsorption energy per deuterium atom is calculated for isomer **1** and accompanied by **2** and **3** showing their relative stability (Table 3). The mean adsorption energies reported for Pt surfaces are also in the same energy range. Depending on the surface structure, hollow sites are favorable [96].

The maximum adsorption energy per D atom in different binding position is given in Table 4. It is clear that the D atom bound in the bridge position on isomer **1** has a high adsorption energy of 1.2 eV. The adsorption energies calculated for D atoms on the surface of isomer **2** are site dependent (for an overview see Table 4).

However, the energy ranges of both D atom positions show that the on-top bound D atom is less stable compared to bridge bound one. The configuration consisting of D atoms bound in a hollow site at the central Pt atom of isomer **2** is possible, however, it results in even lower adsorption energy compared to the on-top site.

Table 4.: Calculated adsorption energies (electronic energies) of differently bound deuterium atoms of isomer 2 ($Pt_{12}D_{24}^- \rightarrow Pt_{12}D_{23}^-$+0.5$D_2$) at TPSS/def2-TZVP level of theory. For positions, see Fig. 27 (Reproduced from S. Gojare *et al.* [90] (2024), *ChemPhysChem* under the terms of the CC-BY license).

Bridge D_x atom	Adsorption energy (eV)	On-top D_x atom	Adsorption energy (eV)
1	1.22	19	0.55
2	1.19	20	0.47
3	1.14	21	0.43
4	1.07	22	0.42
5	0.98	23	0.26
6	0.92	24	0.23
7	0.91		
8	0.8		
9	0.79		
10	0.72		
11	0.71		
12	0.7		
13	0.64		
14	0.61		
15	0.47		
16	0.38		
17	0.37		
18	0.33		

A previous study on bare Pt_n^- clusters concluded that isomer **4** (shown in Figure 23) is the most stable structure in the cluster family of Pt_{12}^-. It can be observed that the structural motif of the Pt core of isomers **3** and **4** is the same. While isomer **1** differs from **4** by a rotation of a capping triangle. Thus, a study is carried out to see whether isomer **1** and **3** are formed from **4** after their interaction with deuterium atoms (Figure 28). The sequential addition of the deuteriums to the bare Pt_{12}^- surface is not possible

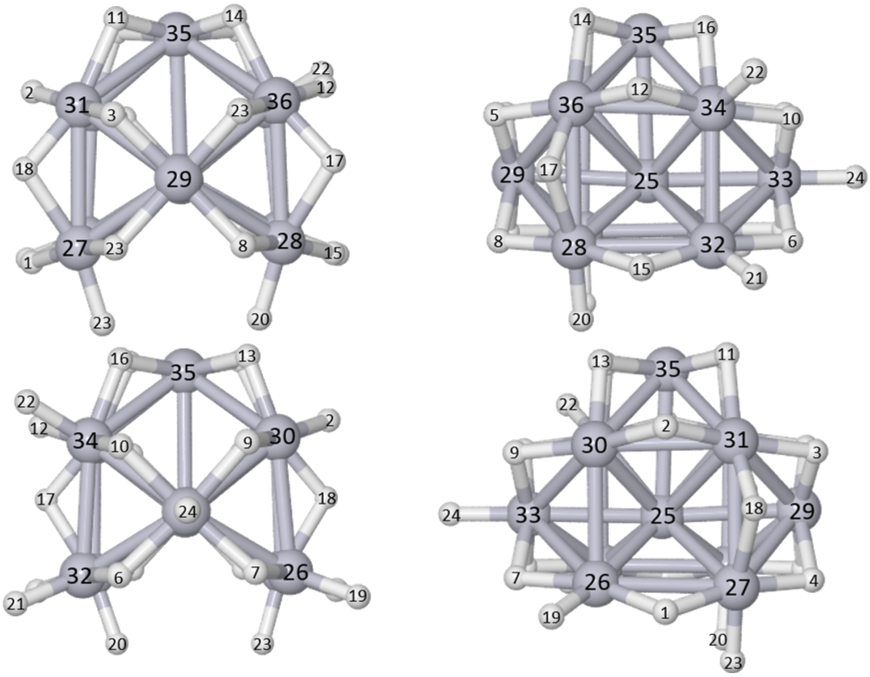

Figure 27.: Different views of isomer **2** (Reproduced from S. Gojare *et al.* [90] (2024), *ChemPhysChem* under the terms of the CC-BY license).

due to significant reconstruction of the Pt core. Therefore, the desorption energy of deuterium atoms was calculated by removing the deuteriums in sets of three atoms. This maintains the 3-fold symmetric structure of the core. At each step, the structure is re-optimized to test, if the core structure changes. For isomer **1**, the energy required to remove the first two sets of atoms amounted to -2.55 and -1.56 eV per deuterium atom respectively, showing the high structure stability. The Pt-core structure at these two steps did not change. The desorption energy for the next set of atoms is reduced to -1.19 eV per deuterium atom showing a weakening in the bond strength. During this particular step, the Pt-core motif changes from *abc* to *aba* (denoted as $Pt_{12}D_{18}^{-}$ $(1)_{[aba*]}$) similar to isomer **3** and **4** indicating that a minimum of 18 D atoms are required to maintain the cuboctahedral cage structure. The energy required for further removal of nine D atoms amounts to -0.97 eV per atom and the last six D atoms require -0.83 eV per D atom showing the sequential weakening of the Pt-D bonds. As seen in the figure 28, core reconstruction is one of the important steps when considering the formation of **1** from **4**. Similar calculations were carried out on isomer **3**. The removal of a set of three-D atoms sequentially constituted to -1.4, -0.75, -0.55, -0.51, and -0.54 eV per D atom. Removing the last six atoms required a desorption energy of -0.57 per atom at each step. From these desorption energies, it is clear that D atoms bound in bridge positions on isomer **1** are more stable than on isomer **2** showing a clear preference for isomer **1**. Please note that the energies reported here may vary depending upon the order of the atom removal other than described here.

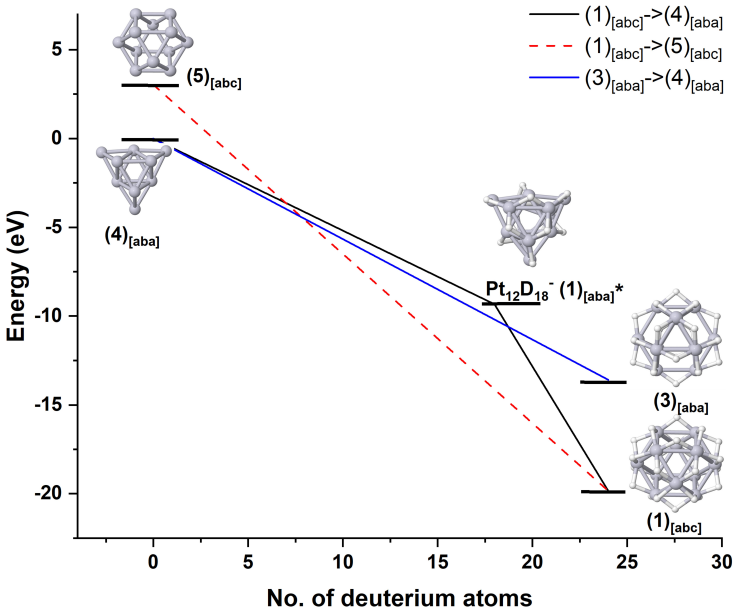

Figure 28.: The plot describing the energy required to convert $Pt_{12}D_{24}^{-}$ to bare Pt_{12}^{-} cluster.

3.2.2.2. Electronic properties

Apart from the structural analysis, electronic interactions of D atoms with the Pt cluster were also analyzed. The differences between the adsorption energies of the D atoms bound in two binding modes were studied using the charges present on the Pt and D atoms of all the isomers. Considering the bare Pt_{12}^{-}, the negative charge is predominantly present on the apex Pt atoms due to their low coordination number (Table 5).

Table 5.: Calculated charges using natural population analysis of isomers (Reproduced from S. Gojare *et al.* [90] (2024), *ChemPhysChem* under the terms of the CC-BY license).

Isomer	Number	Atom	Charge
4	1-3	Pt	-0.197
	4-9	Pt	-0.065
	10-12	Pt	-0.008
1	all	Pt	0.126
	all	D	-0.105

Considering isomer **1**, the total charge on the core is reversed to $\approx$+1.5$|e|$. While in isomer **2**, a strong hydridic character of -0.1$|e|$ per D atom is seen in the bridge position and in the on-top position of -0.05$|e|$ [23] (Table 6). These charges indicate a strong

interaction between the bridge-bound D and the Pt core. This phenomenon can be explained through a multi-center bond character. Natural population analysis, as well as the Wiberg index analysis (Wiberg index of 0.82 for each Pt-D bond), indicate a 3c-2e bond for each Pt-D-Pt bridge. These stabilize the whole cage structure of isomer **1** (and isomer **3**). The 3c-2e bond character for Pt-D-Pt in **1** and 2c-2e bond character for a Pt-D bond in **2** is visualized as Boys localized orbitals in Figure 29.

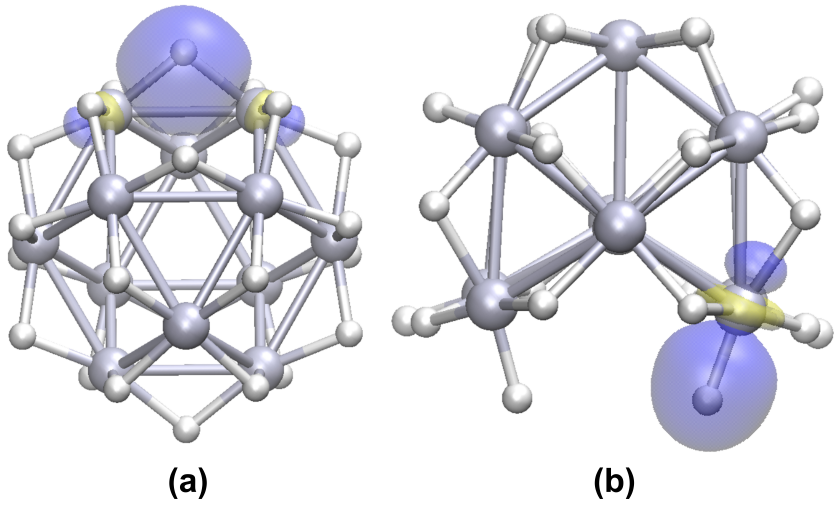

Figure 29.: (a) Three center - two electron bonds between Pt-D-Pt of isomer **1**, (b) two center-two electron bonds between Pt-D of isomer **2** obtained by Boys localization (Reproduced from S. Gojare *et al.* [90] (2024), *ChemPhysChem* under the terms of the CC-BY license).

The density of states computed for the Pt *5d*, and H *1s* orbitals of isomers **1**-**3** are shown in Figure 30. In all plots, *5d* orbital of Pt contribute significantly to the valence band close to the Fermi level. The D*1s* contributions near the Fermi level are present in the case of isomer **2** and are negligible for the cage structures. The contribution of Pt-*5d* orbitals is also determined using the *d*-band center concept. According to the *d*-band center rule of Hammer and Norskov [97], the interaction with the deuterium atoms is stronger when the metal *d* states are located near the Fermi level. For isomer **1** and **3**, it is located at -2.04 eV and -2.26 eV respectively. Thus, the favorable electronic structure is the reason for the high mean deuterium binding energy in isomer **1** which separates it from **3** even though they both have all D atoms in the bridge position.

The structure of anionic $Pt_{12}D_{24}^{-}$ is an open shell system. The cage structures show a large band gap when the total DOS plot is considered. The band gaps calculated for isomer **1**-**3** are 1.99, 0.84, and 1.71 eV. Due to the odd number of electrons, a gap state is present for all isomers in the minority spin channel in unrestricted DFT calculations.

Table 6.: Calculated charges on each atom of isomer **2** using natural orbital population analysis (For positions see Figure 27).

Number	Atom	Charge	D site
1	D	-0.104	bridge
2	D	-0.092	bridge
3	D	-0.107	bridge
4	D	-0.111	bridge
5	D	-0.1	bridge
6	D	-0.081	bridge
7	D	-0.068	bridge
8	D	-0.108	bridge
9	D	-0.077	bridge
10	D	-0.043	bridge
11	D	-0.116	bridge
12	D	-0.076	bridge
13	D	-0.105	bridge
14	D	-0.113	bridge
15	D	-0.103	bridge
16	D	-0.069	bridge
17	D	-0.127	bridge
18	D	-0.115	bridge
19	D	-0.042	on-top
20	D	-0.04	on-top
21	D	-0.048	on-top
22	D	-0.032	on-top
23	D	-0.068	on-top
24	D	-0.044	on-top
25	Pt	-0.388	
26	Pt	0.094	
27	Pt	0.043	
28	Pt	0.131	
29	Pt	0.155	
30	Pt	0.209	
31	Pt	0.089	
32	Pt	0.122	
33	Pt	0.156	
34	Pt	0.217	
35	Pt	0.081	
36	Pt	0.078	

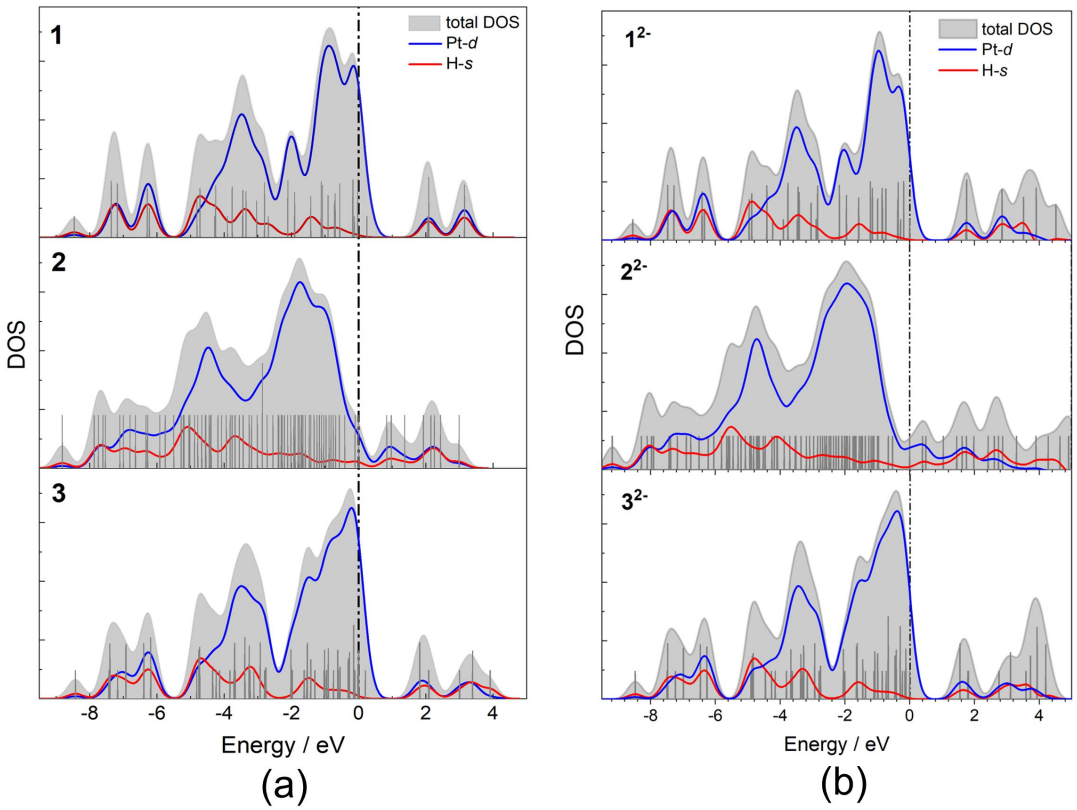

Figure 30.: Density of States plot (DOS) of (a) $Pt_{12}D_{24}^{-}$ isomers **1**-**3**, (b) $Pt_{12}D_{24}^{2-}$ isomers **1**-**3** . The total density is shown in gray, the contributions from the Pt-*5d* and H-*1s* are marked in blue and red. The Fermi level is indicated as a dashed vertical line (Reproduced from S. Gojare *et al.* [90] (2024), *ChemPhysChem* under the terms of the CC-BY license).

These states are present at 0.25, 0.56, 0.2 eV for isomers **1**-**3**. When close shell structures of $Pt_{12}D_{24}^{2-}$ are considered, the band gaps slightly change to 1.73, 0.4, and 1.56 eV for isomers **1**-**3** (Figure 30). The large band gaps show an electronically closed shell configuration, for example seen in the spherical jellium free electron gas model for a simple cluster [98]. A likewise model exists for a free electron gas on a spherical shell known as the Hirsch rule [99] for spherical (π) aromaticity.

The spherical shell in **1** consists of all the Pt atoms. Assumption of transfer of a full electron to a D atom and disregarding the *sd* hybridization, the total number of Pt-*5d* electrons in the valence shell for $Pt_{12}D_{24}^{2-}$ amounts to 98 which satisfies the shell closure condition $n = 2(N+1)^2$ for N=6. The valence shell of $Pt_{12}D_{24}^{-}$ consists of 97 electrons representing near electronic shell closure. For both clusters, spherical aromaticity was analyzed using the Nucleus Independent Chemical Shift (NICS) value. It was calculated at the clusters C_3 axes at a distance of 1 Å above the top deuterium plane to avoid any contamination of the σ-electrons [100]. The NICS value calculated for isomer **1** and $\mathbf{1}^{2-}$ was -5.67 ppm and -6.55 ppm showing a sizeable aromaticity in both clusters. Further

structural analysis of isomer **1** showed that all Pt-Pt bond lengths are equal to 2.71 Å. Such a bond equalization indicates all metal aromaticity which enables the stabilization of the cage structure [101]. Such a stabilization character is missing in isomer **3** due to the distribution of Pt-Pt bond lengths present in the structure. This explains the energy difference between isomers **1** and **3**. In the case of isomer **2**, when some of the bridge-bound D atoms are changed to on-top ones, an increase in mean Pt-Pt bond length to 2.77 Å is seen.

3.2.3. Conclusion

A thorough investigation was carried out using density functional theory to determine the fundamental reasons behind the stability of the cuboctahedral cage structure of $Pt_{12}D_{24}^-$ **1**. According to the fitted experimental profile factor and the computational results, **1** was the best fitting and the lowest energy isomer among the ensemble. The high stability of the cage structure is quite contradictory to the results of bare Pt clusters where metal atoms prefer high coordination numbers. However, in **1**, the number of Pt-Pt bonds are lower compared to the isomer **2**. The two important factors, the number and type of Pt-D bonds, were predominant in these two clusters. The structural analysis of **1** showed that bridge-positioned deuterium atoms interact strongly with the neighboring Pt atoms through multi-center bonds leading to significant charge transfer and binding energy, making the electronic structure quite stable. The mean Pt-Pt bond distance was slightly increased compared to the compact bare Pt_{12}^- cluster **4**.

The experimental scattering data also indicates a small contribution of isomer **2** from the ensemble. In contrast to the most stable isomer **1**, isomer **2** is quite a dynamic structure. The low activation barriers of the different deuterium configurations also indicate that an isomer transformations can take place easily and in combination with the free fcc pocket at the Pt core, it is possibly a more reactive structure. The void at the cuboctahedral cage in structure **1** can be filled by an additional Pt atom to form a highly symmetrical $Pt_{13}H_{24}^-$ O_h cluster as suggested by Mager-Maury et al. [23] and the TIED experiment.

4. Alumina surface

Introduction

Aluminum oxide is a ceramic material extensively used in microelectronics, laser optics, and in heterogeneous catalysis because of its characteristic properties, such as good mechanical robustness, high inertness, natural abundance and presence of the ionic Lewis acid-base sites [12]. In catalysis, it is used as a support for transition metals in many important catalytic processes such as methane oxidation [102], ethylene epoxidation [103], methane reforming reaction [104], catalytic removal of hydrogen sulfide from gas streams [105] and propane dehydrogenation [106]. From these studies, it is seen that alumina as a support is not really that inert in nature but contributes to the catalytic reaction via electron transfer followed by surface relaxations [19]. However, the surrounding environmental conditions can also hamper the surface structure of the support. Structurally, alumina consists of different crystallographic phases that depend on the employed experimental procedures. Among them, the low-temperature transition phase γ-Al_2O_3 surface, is widely utilized in the above mentioned catalytic process due to its characteristic properties. Corundum α-alumina, although less catalytically active, is used as a model system to understand the surface behavior of the support and its interaction with the adsorbates via fundamental properties such as surface relaxation, reconstructions, and electronic structure [107].

Corundum α-Al_2O_3 consists of two types of terminations Al- and O-terminations and several experimental [108] and theoretical investigations [109–111] have been carried out to determine the energetically stable surface termination. The investigations have concluded that Al-termination of α-Al_2O_3 is stable and has a low surface energy due to its non-polar nature and significant inward layer relaxation (≈63 %). It is also seen that the α-Al_2O_3 surface is prone to readily react with water, forming surface hydroxyl groups with negligible activation barrier. The presence of surface hydroxyl groups [112–114] on corundum was found to occur even at high temperatures of 1100 °C [108]. The results showed a clear preference for the water adsorption in dissociated form with adsorption energy of 1.3 eV [114]. The water dissociated in 1-2 configuration (OH^- bound to surface Al and H^+ bound to immediate neighboring surface oxygen) was found to be stable resulting from significant surface relaxation. The water dissociated in 1-4 configuration (OH^- bound to surface Al and H^+ bound to next neighboring surface oxygen) was another stable configuration found [13, 115].

The investigation concerning the interactions of small molecules with the metal-oxide surfaces is important in the fields of heterogeneous catalysis and corrosion. In the past, the surface behavior of Al-terminated α-Al_2O_3 has been widely studied using the adsorption of small molecules such as HCl [116], CO [14, 15, 115], CO_2 [117], H_2O [13, 112, 114, 118] and methanol [119]. Among these molecules, adsorption and interaction of CO on α-Al_2O_3 is of particular interest in the studies of surfaces. The surface modifications can be easily probed with respect to the variation in the characteristic properties of the CO molecule. The theoretical analysis conducted by Casarin *et al.* [15] regarding CO adsorption on an Al_8O_{12} cluster model using DFT with the BP functional showed that CO mainly interacts with the Lewis acid site via the C-down orientation having an adsorption energy of -13.36 kcal/mol and a C-O stretching frequency blue-shifted by 44 cm^{-1} compared to the free molecule. Further, the chemisorption of the CO molecule led to charge transfer from CO $\rightarrow$ Al^{3+} site affecting the σ-C orbital population. Rohmann *et. al.* [14] studied the adsorption of the CO molecule and vibrational frequencies with respect to the CO coverage on the α-Al_2O_3 surface using plane wave DFT and the PBE functional. The results indicated that the adsorption energy of the CO molecule was 0.52 eV for θ=0.25 coverage and decreased to 0.42 eV at θ=1. The vibrational frequency shift in all cases was blue-shifted compared to the gas phase CO and the shift decreased from 56 cm^{-1} for θ=0.25 to 30 cm^{-1} for θ=1. This change in the adsorption energy and vibrational frequencies resulted from the surface relaxation upon CO adsorption. They further studied the interaction of the CO molecule with the obtained pre-hydroxylated α-Al_2O_3 surface [115]. The highest adsorption of CO E_a=0.57 eV was calculated for θ_{CO}=0.25 and θ_{water}=0.25 and it decreased with increase in the pre-hydroxylation.

Additionally, studies focusing on CO_2 interaction on α-Al_2O_3 have also gained importance. Due to the increase in CO_2 emissions from industries and automobiles, extensive efforts are channelized to utilize the unlimited source of CO_2 to transform it into valuable chemicals. Some of the viable routes in industry are the selective hydrogenation of CO_2 to make methanol, methane and different organic carbonates [20, 22, 120–122]. The key step in these processes is the C-O bond dissociation to form new molecules. However, CO_2 is thermodynamically quite stable and therefore dissociation of the molecule requires novel catalysts which can activate it upon adsorption on the surface. Influence of surface terminations such as OH groups on the CO_2 conversions cannot be ruled out. Studies have shown that different CO_2 species such as carbonates, bicarbonates, carboxylates as well as bent CO_2 species are formed upon interacting with the surface hydroxyl groups [123]. Casarin *et. al.* studied the interaction of CO_2 with both hydroxylated as well as partially reduced α-Al_2O_3 surfaces experimentally and theoretically. They pointed out that formation of surface bicarbonate is the most stable configuration while CO_2 dissociates in the presence of surface oxygen vacancy on partially reduced α-Al_2O_3 surface [117]. Another theoretical study carried out by Liu *et. al* on adsorption and decomposition of CO_2 on the γ-Al_2O_3 (1 0 0) surface showed that CO_2 adsorbs on the perfect defect free γ-Al_2O_3 surface in different configurations such as linear, monodentate, bidendate, tridentate and with a bent bridge geometry via charge transfer from acid sites to the molecule. On such vacancy-free surfaces it is seen that CO_2 attaches via

weak physisorption without any molecular decomposition [124]. There are also reports showing that surface hydroxyl groups interact with the adsorbed CO_2 on supported transition metal particles and influence the distribution of the final products formed during the catalytic process along with stabilization of the system [20–22, 125].

Various catalytic reactions such as CO oxidation and CO_2 hydrogenation mainly take place on the metal-oxide supported transition-metal nanoparticles due to their structural integrity, and alteration of electronic properties at the metal-oxide interface leading to high catalytic activity [126, 127]. However, these catalytic reactions occur on the catalyst surface and prominently at the low-coordinated active sites facilitating a strong interaction with the adsorbate molecules. Thus, the subsurface or the core atoms in the nanoparticles introduce an additional cost of the material resource. While these noble metals are a limited resource, efforts are directed towards minimizing the size of the transition-metal nanoparticles. This motivated the development of single-atom catalysts (SAC) consisting of highly dispersed single metal atoms on the support to ensure that all atoms are accessible for the surface catalytic processes [17, 128–131]. Additionally to the sustainable usage of noble metals, SACs are relatively homogeneous under-coordinated active sites leading to improved catalytic activity and optimum resource utilization [132]. However, the challenge faced with the usage of SACs is the loss of dispersion in the course of the catalytic process because of the tendency of metal atoms to agglomerate, eventually decreasing the catalytic activity [17, 133]. Therefore, to prevent the formation of metal nanoclusters, the anchoring of the metal atoms to the surface should be strong enough to eventually hinder the agglomeration [134]. There are multiple studies carried out to achieve high metal dispersion by modifying the metal-oxide surfaces [10, 135, 136]. In such a catalytic system, multiple factors are seen to play a role in the binding of metal atoms on the surface such as relaxation of the metal-oxide surface, surface defects, and charge transfer at the interface which alter the reactivity of the whole system. Elucidating these factors experimentally is quite challenging. Thus, with the help of quantum-mechanical methods, these factors can be studied separately and can determine the influence of the individual factors on the catalytic activity.

Single Pt atom in Pt SAC are the building blocks of the larger supported nanoparticles and therefore it is important to determine the structure and electronic properties at the regular surface sites [137–140]. Neyman *et. al* [137] studied the adsorption of various *d*-metal atoms on the MgO (001) surface using an embedded cluster model and DFT with BP86 functional. The results showed that the lowest energy state of the Pt atom had the electronic configuration of d^{10} and is strongly bound to the O^{2-} anion with an adsorption energy of 2.39 eV leading to an upward displacement of neighboring Mg atoms. Rivanenkov *et. al.* [138] studied the adsorption of the Pt atom on the bare Al-terminated α-Al_2O_3 using an embedded cluster model and DFT with BP86 functional. They considered two models, $Pt/Al_{10}O_6$ and $Pt/Al_{23}O_{15}$ in their study. Their results showed that the adsorption energy of the Pt atom is site-dependent and leads to strong adsorbate-induced surface relaxation. The bonding at the Pt/α-Al_2O_3 interface is moderately ionic. While Wang *et. al.* [18] showed that the site-dependent Pt atom adsorption is mainly facilitated

by the charge transfer at the $Pt/Al_{23}O_{15}$ interface where electron transfer takes place from Pt towards the surface facilitating strong interaction.

Pt SACs are developed and applied in various catalytic reactions such as hydrogenation [141], propane dehydrogenation [142], CO oxidation [143] and alcohol decomposition reactions [144]. It has been reported that in such catalytic systems, other than the interaction between the adsorbed Pt atom and the adsorbate, metal-oxide support and its terminations also play a crucial role in facilitating charge transfer helping anchor the reaction intermediates during the reaction. However, this type of interaction is strongly dependent on the nature of the metal and the electronic structure of the support. An experimental study [131] was carried out on the influence of different metal-oxide supports on the CO oxidation reaction on supported single Pt atoms. The results showed that in the absence of -OH surface terminations, the catalytic reactivity of the Pt SACs is affected by the nature of the support. The interaction between Pt and the surface oxygen ions are the active sites for CO oxidation. However, in the presence of the surface-OH groups, the effect of the support is negligible and it acts only as a carrier for the dispersed Pt atoms. In this case, Pt-OH acts as an active site and is a decisive factor for the charge state of the adsorbed Pt atom. However, experimentally the role of Pt-OH interaction in the catalytic activity is experimentally unclear. Another experimental study showed that the presence of surface -OH groups promoted the dispersion of single Pt atoms on the Al_2O_3 surface [145].

As seen in the previous studies, α-Al_2O_3 support and its surface terminations play a key contribution in the catalytic activity besides being an anchor for metal particles and small molecules, therefore it is essential to study theoretically these interactions at different levels of theory. Until now, all the theoretical studies related to CO adsorption on Al-terminated α-Al_2O_3 (0001) surface were carried out by employing wavefunction-based methods and plane-wave DFT using LDA and GGA functionals. It is well known that GGA functionals perform poorly when predicting molecular adsorption energies and activation barriers [146]. Therefore, in the present work, I carried out a systematic study to analyze the local interaction of CO and CO_2 molecules and Pt SAC on three different types of Al-terminated α-Al_2O_3 (0001) surfaces: the bare surface ($\theta[H_2O]$=0), the fully hydroxylated ($\theta[Al(OH)_3]$=1) and one with dissociated H_2O ($\theta[H_2O]$=1). The hybrid functionals, B3LYP and PBE0 along with GGA functional PBE with large def2-TZVPP basis-set was used to analyze quantitative trends. In particular, I focus on the changes of the α-Al_2O_3 (0001) surface such as surface relaxation, and electronic properties. The shift in the vibrational frequency of the small molecules upon the adsorption is also computed depending on the degree of surface hydroxylations. In this study, an embedded cluster model along with the wave function-based MP2 method with a larger basis set is also employed.

This Chapter is divided into the following sections: section **4.1** is based on CO adsorption on α-Al_2O_3 (0001), section **4.2** is based on CO_2 adsorption on α-Al_2O_3 (0001) and section **4.3** describes CO adsorption on the Pt SAC.

Computational details

The theoretical calculations were carried out with TURBOMOLE (version 7.7) [80, 81] based on the structural information obtained in Ref. [147]. Three different terminations from Ref. [147] were considered, the water-free surface ($\theta[H_2O]=0$), fully hydroxylated surface ($\theta[Al(OH)_3]=1$) and dissociated H_2O ($\theta[H_2O]=1$) surface. In all cases only one molecule (CO or CO_2) was adsorbed at the surface, resembling best the low coverage case.

4.0.0.1. Point charge field

The unit cells of all three surfaces used for generating the point charge field were first optimized using periodic DFT and PBE-(D3) level of theory [147] in the group of Dr. Philipp Plessow. Two types of unit cells were generated for each surface (shown in Figure 31): one unit cell with the first four layers optimized (denoted as half relaxed) keeping the rest fixed and the second type of unit cell was fully optimized (denoted as full relaxed).

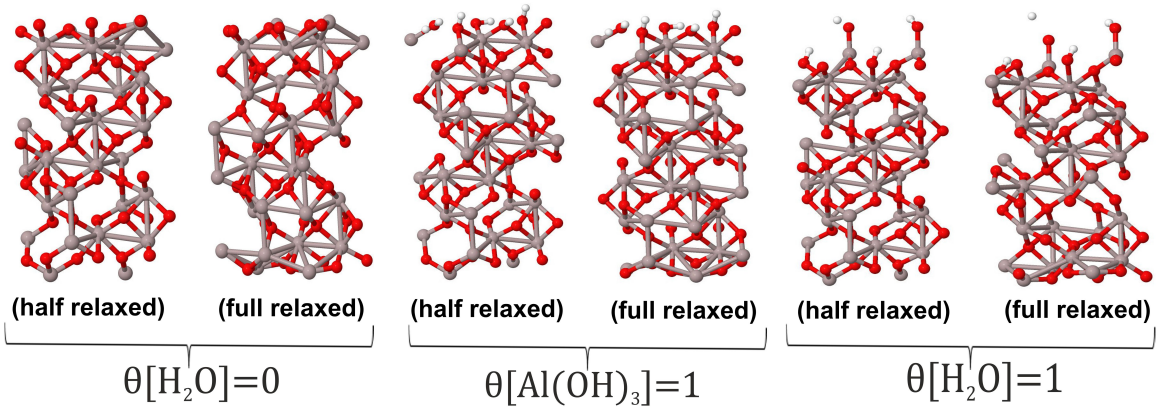

Figure 31.: Unit cells of $\theta[H_2O]=0$, $\theta[Al(OH)_3]=1$, $\theta[H_2O]=1$ surfaces used for generation of the point charge fields (Color scheme: grey-Al, red-O).

The point charges were set up using the Evjen program [148]. The charges used in the point charge field (PCF) were +3 for Al, -2 for O, and +1 for H. In most cases the unit cells from Ref. [147] had a dipole moment, perpendicular to the surface. Only the fully relaxed unit cell (taken from Ref. [147]) of the water-free surface didn't have such a dipole moment. However, the half-relaxed unit cells for $\theta[Al(OH)_3]=1$ and $\theta[H_2O]=1$ had a strong dipole moment. Therefore, additional point charges above the surfaces and away from the adsorption site were placed to compensate for the effect. The half-relaxed unit cells with only upper layers relaxed were used for $\theta[Al(OH)_3]=1$ and $\theta[H_2O]=1$ surface. The desired adsorption site and the nearby atoms of the point charge field were replaced by the quantum cluster (QC).

4.0.0.2. Quantum cluster (QC)

A quantum cluster was defined around the adsorption site under study. The clusters of various sizes and shapes of all three surfaces were generated depending on the desired adsorption site. These clusters were investigated utilizing three different functionals: PBE [31], B3LYP [33], and PBE0 [149] along with def2-SVP and def2-TZVPP basis sets [84]. Initial geometry optimization of the cluster was carried out using a smaller basis set def2-SVP and then re-optimized using def2-TZVPP basis set. The RI-J (resolution of identity for the Coulomb term J) approximation was used [82, 83]. The def2-TZVPP basis set was used for the area of the cluster that was relaxed in the geometry optimization and the rest fixed part was treated with the def2-SVP basis set. Dispersion corrections were incorporated using the D4 model [150]. The surrounding Al^{3+} atoms of these clusters were always kept fixed and treated with effective core potentials (ecp-10 Hay & Wadt) [151] without basis set to avoid the fluctuation of electrons into the PCF. The geometry optimizations were carried out using default TURBOMOLE parameters. To check the reliability of the cluster, different sizes of the clusters were examined. Extent of the top layer relaxation was also checked by using sequential shell relaxation approach (discussed in detail in section 4.1). Two main types of clusters were generated, Al^{3+} and O^{2-} centered clusters depending on the molecular affinity towards the adsorption sites in the particular study. The reported molecule's binding energy for e.g CO binding energy (BE) was calculated as follows,

$$E_{ads} = E_{CO@cluster} - E_{cluster} - E_{CO(g)} \tag{69}$$

$E_{CO@cluster}$ is the energy of the whole system, $E_{cluster}$ denotes the energy of only the cluster and $E_{CO(g)}$ the energy of single CO molecule. All these energies were calculated at different levels of theory. The CO BE was counterpoise corrected to determine the basis set superposition error (BSSE) [152]. The BSSE correction of the whole system was calculated by dividing the system into two fragments: cluster and CO molecule.

$$E^{CP}_{CO@cluster} = E(CO@cluster) + \Delta E[cluster] + \Delta E[CO] \tag{70}$$

$$\Delta E[cluster] = E(Cluster_{[CO@cluster]}) - E_{ghost}(Cluster_{[CO@cluster]}) \tag{71}$$

$$\Delta E[CO] = E(CO_{[CO@cluster]}) - E_{ghost}(CO_{[CO@cluster]}) \tag{72}$$

Equations 71 and 72 are the differences in the energy of the respective fragment with and without the basis sets of the other fragment (defined as ghost) in the full system (CO@cluster). The CO BE was calculated using the difference of the BSSE corrected total energy and the sum of the energies of the cluster and $CO_{(g)}$ molecule.

$$E_{CO} = E^{CP}_{CO@cluster} - (E_{cluster} + E_{CO_{(g)}}) \tag{73}$$

The CO harmonic vibrational frequency was calculated using numerical evaluation with fixed atoms and was scaled using a scale factor (λ_d) defined as:

$$\lambda_d = \frac{{\nu_i}^{exp}}{{\omega_i}^{exp}}, \tag{74}$$

where ν_i^{exp} is the experimental frequency for the CO molecule in the gas phase (2143 cm^{-1}) [153] and ω_i^{exp} is the harmonic vibrational frequency of the $CO_{(g)}$ molecule computed with the corresponding theoretical method. The following scaling factors were used: 1.0071719 for PBE, 0.9691263 for B3LYP, 0.9577354 for PBE0 and 0.9927317 for MP2 method. A similar procedure was followed for the calculation of the CO_2 properties as well.

Additionally, second-order Møller-Plesset perturbation theory (MP2) [26] was also employed to calculate the binding energies and vibrational frequencies for all the surfaces.

4.1. CO adsorption on α-Al_2O_3 surface

4.1.1. Experiment

Recently, the energetically stable and clean Al-terminated α-Al_2O_3 single crystal was studied experimentally using X-ray photoelectron spectroscopy (XPS) along with the polarization-resolved IRRAS technique with CO as a probe molecule (also called the CO surface-ligand IR (CO-SLIR) approach) in the group of Dr. Yuemin Wang (IFG, KIT). The main observation reported in the XPS result was the presence of the characteristic peak at 531.8 eV for the surface hydroxyl groups in addition to the two peaks, 73.8 eV for Al^{3+} and 530.4 eV for O^{2-} (Figure. 32). The concentration of these hydroxyl groups amounted to 17% resulting from its high surface reactivity. This data was further confirmed by the polarization-resolved IRRAS result obtained at the temperature of 70 K and after the exposure of 5 L CO on the α-Al_2O_3 surface (Figure. 33). The IRRAS spectra consisted of two peaks at 2162 and 2173 cm^{-1}. The dominant peak at 2173 cm^{-1} is characteristic of CO bound to the Al^{3+} cations of the surface while the weaker signal at 2162 cm^{-1} was attributed to the CO adsorbed on the acidic hydroxyl groups through OH-CO hydrogen bonding. The temperature-dependent IRRAS results revealed that two distinct CO species with different binding energies are present on the surface. As the temperature of the sample increased from 70 K to 85 K, the IR band at 2162 cm^{-1} disappeared completely showing the weakly bound character of CO molecules. Further increasing the temperature led to the gradual decrease in the intensity of the peak at 2173 cm^{-1} and finally vanishing at the temperature of 100 K. Additionally, the CO

coverage dependence on the temperature was seen through the decrease in the IR band of CO-Al^{3+} followed by the strong blue shift in the CO vibrational frequency from 2173 cm^{-1} (at 70 K) to 2186 cm^{-1}(at 95 K).

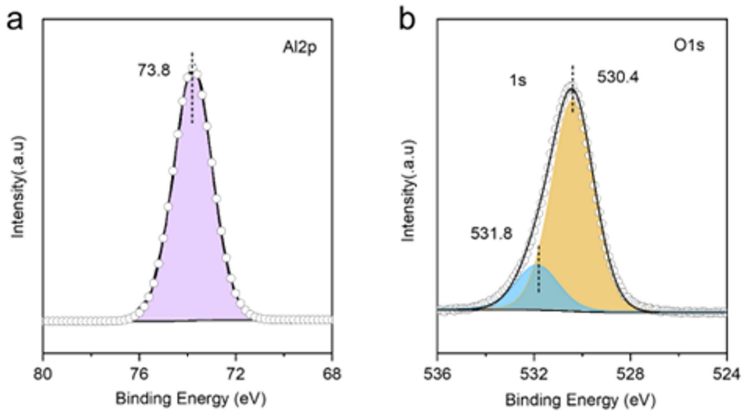

Figure 32.: Grazing-emission XPS characterization of the α-Al_2O_3(0001) surface. (a) Al 2p; (b) O 1s [Figure was provided by Dr. Yuemin Wang](Reproduced from S. Gojare *et al.* [154] (2025), *ChemPhysChem* under the terms of the CC-BY license).

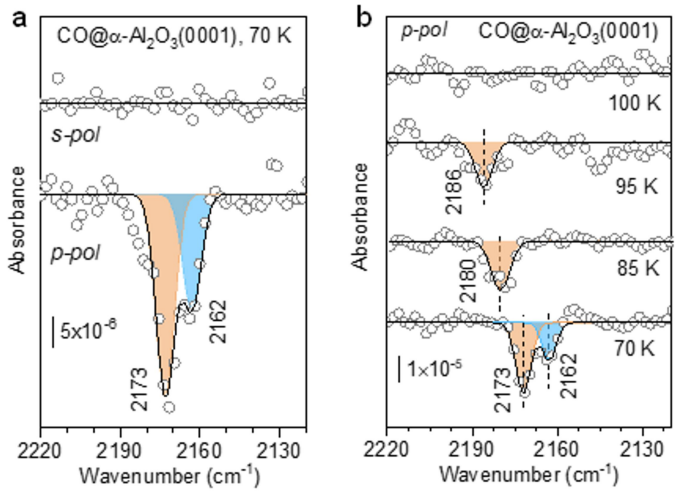

Figure 33.: (a) Polarization-resolved IRRAS data recorded after 5 L CO adsorption on α-Al_2O_3(0001) at 70 K at a grazing incidence angle of 80°. (b) Temperature-dependent IRRAS data obtained after saturation adsorption of CO at 70 K on the α-Al_2O_3(0001) surface then subsequently annealing to indicated temperatures [Figure was provided by Dr. Yuemin Wang] (Reproduced from S. Gojare *et al.* [154] (2025), *ChemPhysChem* under the terms of the CC-BY license).

To further investigate the CO/α -Al_2O_3 system, a theoretical analysis was carried out using the embedded cluster model to validate the experimental results described above.

4.1.2. Results and discussion

4.1.2.1. Size of the quantum cluster

The selection of the appropriate cluster size is one of the important factors that must be considered while using the embedded cluster model. The cluster size should be reasonably large to study the physical and chemical properties of interest. To check the adequate cluster size, the convergence of the CO binding energy (BE) was used as the criteria.

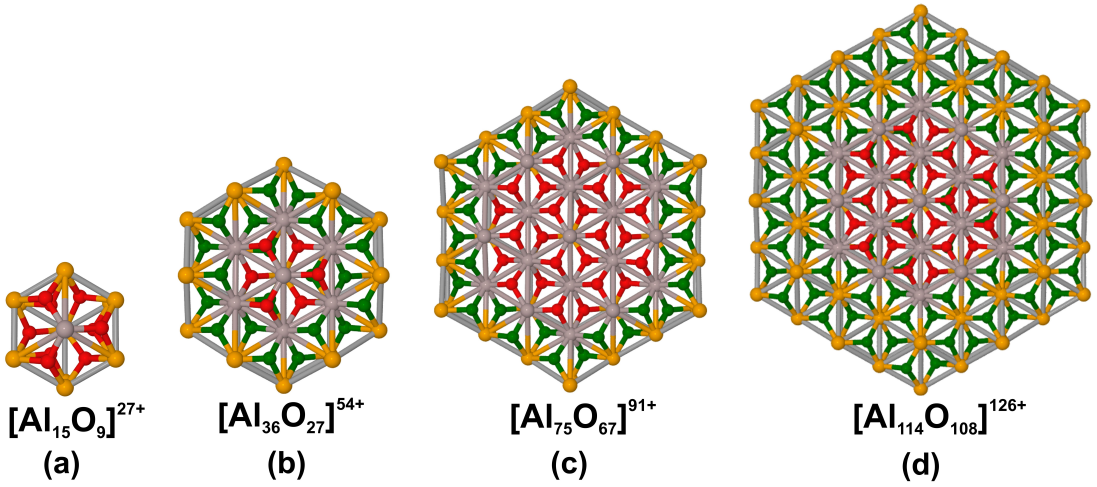

Figure 34.: Different cluster sizes (a-d) for the water-free ([θ[H_2O]=0) surface considered in this work (Color scheme of atoms: yellow-fixed Al, grey-unfixed Al, green-fixed oxygen, red-unfixed oxygen) (Reproduced from S. Gojare *et al.* [154] (2025), *ChemPhysChem* under the terms of the CC-BY license).

Figure 34 shows the schematic of different cluster sizes explored for the θ[H_2O]=0 surface. The cluster size was increased by consecutively adding the surrounding Al and O shells to the previously optimized smaller cluster. Each cluster consisted of three bottom layers of which only the top layer was relaxed while the rest was kept fixed. Three layers were chosen for the symmetry reason. The bottom layers were fixed to guarantee a smooth continuation to the bulk structure used in PCF. The results showed that the CO BE converged gradually until sizes (c) and (d) with BE of (-0.95)-(-0.97) eV (without BSSE correction) respectively (see Table 7). A test calculation was carried out to analyze the influence on the CO BE by relaxing the Al atom beneath the adsorption

site. However, there was negligible influence seen on the CO BE. Thus, due to the computational effort, cluster size (c) was chosen for further calculations.

Table 7.: CO binding energy (E_{bind}) (eV), scaled CO vibrational frequency ν(CO) (cm^{-1}) on the clusters of the $\theta[H_2O]$=0 (water-free) surface and calculated using the B3LYP and def2-TZVPP basis set (no BSSE correction included). Refer Figure 34 for the nomenclature (Reproduced from S. Gojare *et al.* [154] (2025), *ChemPhysChem* under the terms of the CC-BY license).

Cluster size	E_{bind} (eV)	ν(CO) (cm^{-1})
(a)	-0.56	2210
(b)	-0.75	2165
(c)	-0.95	2195
(d)	-0.97	2192

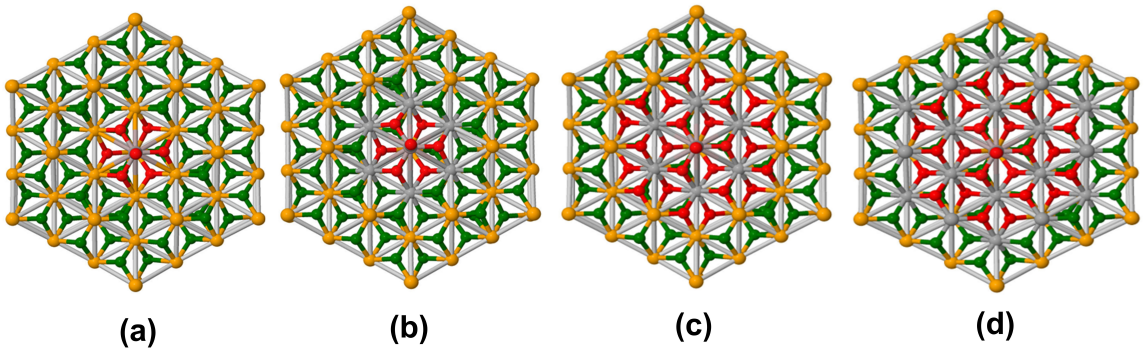

Figure 35.: Schematic of sequentially relaxed Al and O shells surrounding the adsorption site of the CO molecule (a-d) of the cluster size (c) shown for $\theta[H_2O]$=0 surface (Figure 34). (Color scheme of atoms: yellow-fixed Al, grey-unfixed Al, green-fixed oxygen, red-unfixed oxygen) (Reproduced from S. Gojare *et al.* [154] (2025), *ChemPhysChem* under the terms of the CC-BY license).

The local interactions between the CO molecule and differently terminated α-Al_2O_3 surfaces ($\theta[H_2O]$=0 (water-free), $\theta[Al(OH)_3]$=1 (fully hydroxylated), and with water dissociated $\theta[H_2O]$=1 surface) at low CO coverage was analyzed using the sequential shell relaxation approach on the embedded cluster size (c) (schematically shown in Figure 35 for the $\theta[H_2O]$=0 surface). In the first relaxation step, the cluster region consisted of only the central Al^{3+} and the first oxygen shell (6 atoms), and the rest was kept fixed. The region for relaxation was increased by systematically adding the surrounding Al and O shells to the pre-relaxed cluster part. The atoms at the edge of the cluster were always kept fixed. The structural properties such as CO binding energy, CO orientation, adsorbate-induced surface relaxations, charge transfer, and vibrational frequency were studied as a function of the relaxed shells.

4.1.2.2. CO binding energy

The variation in the CO BE as a function of the relaxed shell is shown in Figure 36.

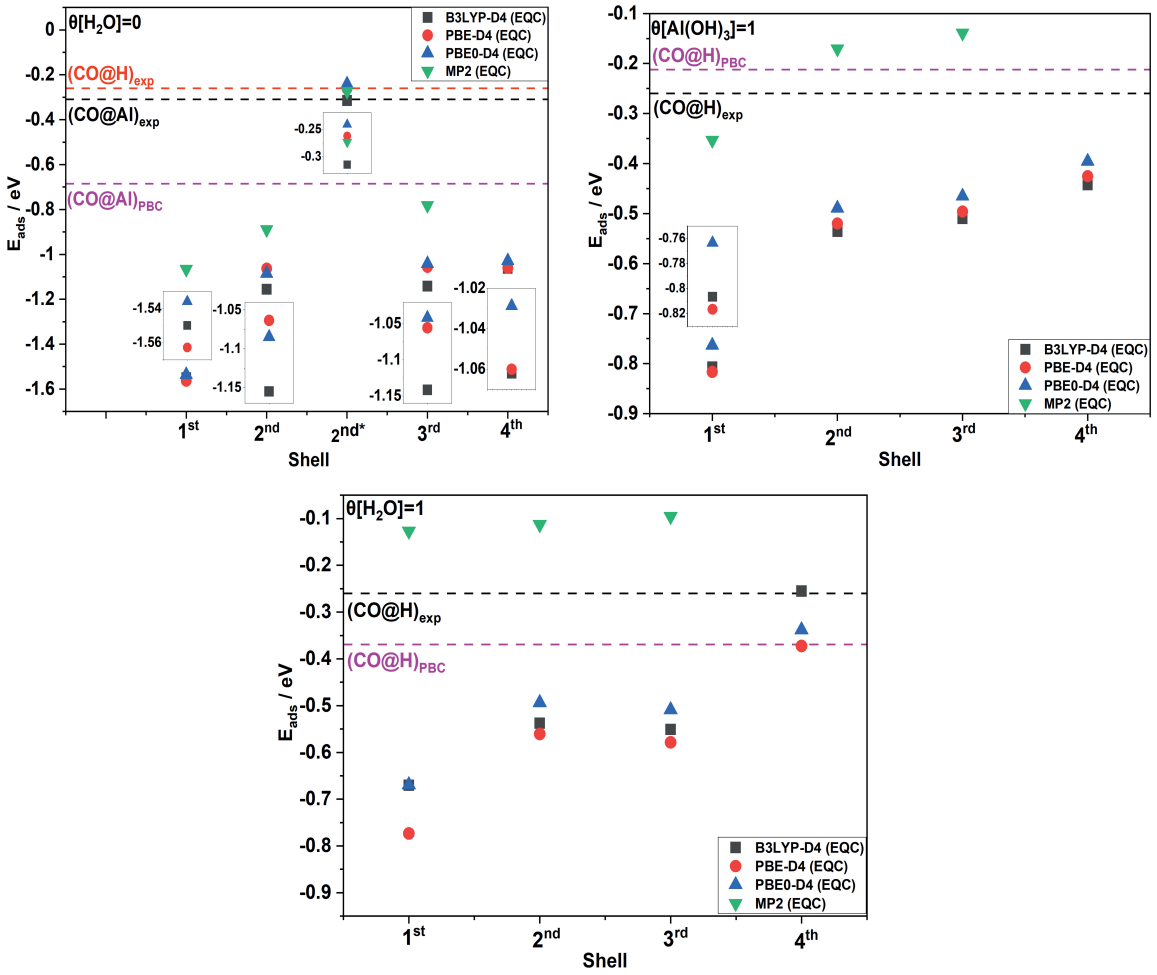

Figure 36.: CO binding energy as a function of the number of relaxed shells of cluster size (c) obtained for water-free [θ[H_2O]=0] (Figure 34), the model θ[[H_2O=0]+OH+H] with CO adsorbed on hydroxyl group (denoted 2nd*) (see the description in the text), as well as for full hydroxylated [θ[$Al(OH)_3$]=1] and H_2O dissociated [θ[H_2O]=1] surfaces. For each surface, the CO binding energy is calculated without BSSE corrections. In all the cases only a single CO molecule was adsorbed. The def2-TZVPP basis set was used in all the computations. The horizontal dashed lines represent the binding energies obtained by periodic DFT and in the experiment (Reproduced from S. Gojare *et al.* [154] (2025), *ChemPhysChem* under the terms of the CC-BY license).

The provided BE values do not contain the BSSE correction and are used to verify its convergence with respect to the relaxed shell. The general trend shows that upon relaxation of the first shell, the CO BE is overestimated for θ[H_2O]=0 surface and underestimated for θ[$Al(OH)_3$]=1 and θ[H_2O]=1 surfaces. This is due to the tight structural restrictions. Further relaxation up to the 2^{nd} shell showed a strong reduction in the CO BE values

due to the extra stability gained by the structural relaxation. Small changes in BE were seen for the 3^{rd} shell relaxation. The results obtained for the 4^{th} shell relaxation were neglected. The atoms of the 4^{th} shell were close to the edge of the cluster, which gave rise to inconsistent results. Hence, relaxation until the 3^{rd} shell for $\theta[H_2O]$=0 surface and relaxation until the 2^{nd} shell for $\theta[Al(OH)_3]$=1 and $\theta[H_2O]$=1 surfaces yielded reliable CO BE. A comparison at different levels of theory showed that the BE calculated with hybrid functionals and PBE are in a similar energy range. The CO BE calculated using MP2 method for $\theta[H_2O]$=0 surface is also in the same range. However, it cannot properly describe the CO adsorption scenario in the case of $\theta[Al(OH)_3]$=1 and $\theta[H_2O]$=1 surfaces.

4.1.2.3. CO binding mode

The binding character of the CO molecule on the $\theta[H_2O]$=0, $\theta[Al(OH)_3]$=1 and $\theta[H_2O]$=1 surfaces was analyzed. The side and top view of the energetically stable CO@cluster configurations on all three surfaces are shown in Figure 38 and 37.

Table 8.: Tilt angle of the adsorbed CO relative to the z-axis at $\theta[H_2O]$=0 and $\theta[[H_2O{=}0]+OH+H]$ surfaces and is calculated with respect to the nearby atoms of the cluster (refer Figure 37 for nomenclature). All values are calculated using def2-TZVPP basis set (Reproduced from S. Gojare *et al.* [154] (2025), *ChemPhysChem* under the terms of the CC-BY license).

Atoms selected	CO tilt angle (θ) (°)					
	$\theta[H_2O]$=0			$\theta[[H_2O{=}0]+OH+H]$		
	PBE	B3LYP	PBE0	PBE	B3LYP	PBE0
Al_0-C-O	0	0	0	51	13	43
Al_1-C-O	40	40	40	66	35	57
Al_2-C-O	37	37	38	71	33	65
Al_3-C-O	40	40	40	60	25	57
Al_4-C-O	38	37	38	31	13	34
Al_5-C-O	40	40	40	24	17	16
Al_6-C-O	38	37	38	45	27	35
O_1-C-O	34	34	34	59	24	51
O_2-C-O	20	20	20	64	24	58
O_3-C-O	34	34	34	47	11	43
O_4-C-O	20	20	20	33	6	27
O_5-C-O	34	34	34	38	10	30
O_6-C-O	20	20	20	55	27	46

From the figure 38, it is clear that CO binds strongly to the surface Al^{3+} cation and prefers a perpendicular orientation with θ=180° on $\theta[H_2O]$=0 surface (refer to Table.

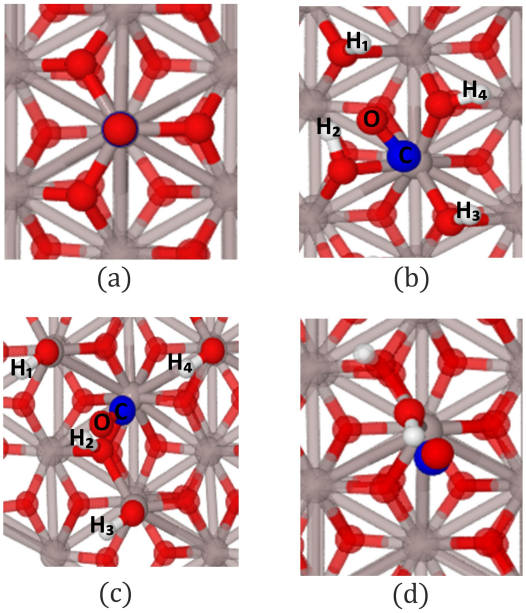

Figure 37.: Top view of the clusters showing the interaction between CO molecule and the nearby surface hydroxyl groups. (a) Water-free (clean/dry) [$\theta[H_2O]$=0] surface; (b) full hydroxylated [$\theta[Al(OH)_3]$=1] surface; (c) H_2O dissociated [$\theta[H_2O]$=1] surface (c); (d) low coverage model [θ[[H_2O=0]+OH+H] (see text for description). (Color scheme of atoms: grey-unfixed Al, red-unfixed oxygen, white-unfixed hydrogen, blue-carbon) (Reproduced from S. Gojare *et al.* [154] (2025), *ChemPhysChem* under the terms of the CC-BY license).

8 for the values calculated using all three DFT functionals). In this configuration, the strong interaction at the interface is facilitated by a charge transfer of 0.16 $|e|$ from the CO molecule to the surface (Figure 38(a) and 37(a), Table 9). On the other hand, a large distance is present between the surface and CO molecule in the cases of $\theta[Al(OH)_3]$=1 and $\theta[H_2O]$=1 surfaces showing that CO is weakly adsorbed. This is due to the inaccessible surface Al^{3+} cations for the molecule to bind strongly to the surface (Table 11). Thus, the CO molecule weakly interacts with the surface and is mainly stabilized by the weak electrostatic interactions with the surrounding surface hydroxyl groups (Figure 38(b)-38(c) and 37(b)-37(c)).

Upon adsorption of the CO molecule, adsorbate-induced relaxation was observed. The relaxation effect was calculated as the change in the displacement of the top Al^{3+} atom along the surface normal before and after the CO adsorption. The values for all surfaces are given in Table 10. CO adsorption on $\theta[H_2O]$=0 surface led to a slightly downward dispacement of the Al^{3+} cation (≈0.3 Å) towards the bulk. This is due to the low coordination of the surface atoms, which show high surface reactivity. On the other two surfaces, $\theta[Al(OH)_3]$=1 and $\theta[H_2O]$=1, the Al^{3+} at the adsorption site moved negligibly in an upward direction due to the interaction of surface OH groups with the CO molecule via OC-HO interaction. The detailed study on the relaxation of the top layer without an adsorbate on respective surfaces is given in Chapter 4.2. The CO bond length

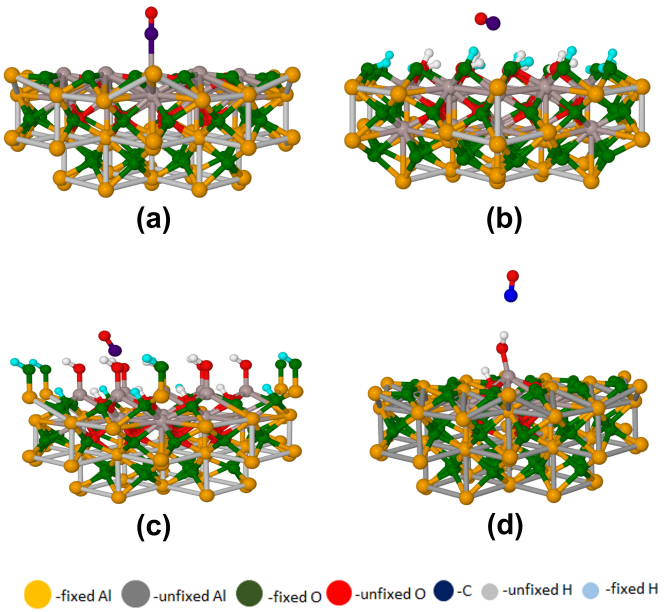

Figure 38.: Schematic of the CO binding configuration on the water-free (clean/dry) ($\theta[H_2O]$=0) surface (a); the full hydroxylated ($\theta[Al(OH)_3]$=1) surface (b); the H_2O dissociated ($\theta[H_2O]$=1) surface (c), and the low coverage model ($\theta[[H_2O{=}0]{+}OH{+}H]$) (d) (see text for description). (Color scheme of atoms: yellow-fixed Al, grey-unfixed Al, green-fixed oxygen, red-unfixed oxygen, blue-carbon, white-unfixed hydrogen, cyan-fixed hydrogen) (Reproduced from S. Gojare *et al.* [154] (2025), *ChemPhysChem* under the terms of the CC-BY license).

calculated using hybrid functionals showed a small contraction on $\theta[H_2O]$=0 surface compared to the $CO_{(g)}$. While it remained constant on $\theta[Al(OH)_3]$=1 and $\theta[H_2O]$=1 surfaces (Table 11).

Table 9.: Atomic charges (in $|e|$) and orbital population computed using B3LYP and def2-TZVPP basis set for C, Al, O atoms of $\theta[H_2O]$=0 surface (Reproduced from S. Gojare *et al.* [154] (2025), *ChemPhysChem* under the terms of the CC-BY license).

Model	Atoms	Charge	Orbital population	
			Core	Valence
Surface	Al	2.220	9.991	0.730
$(CO)_g$	C	0.486	1.999	3.467
	O	-0.486	1.999	6.450
CO on $\theta[H_2O]$=0	Al	2.048	9.992	0.906
	C	0.612	1.999	3.343
	O	-0.383	1.999	6.350

Table 10.: The calculated adsorbate induced relaxation (Å) (the change in distance between the top and the second Al layer upon CO adsorption) with respect to the relaxed shells. All values are calculated using the def2-TZVPP basis set (Reproduced from S. Gojare *et al.* [154] (2025), *ChemPhysChem* under the terms of the CC-BY license).

Relaxed shell	Surface	Layer relaxation (Å)		
		PBE	B3LYP	PBE0
1^{st}	$\theta[H_2O]$=0	-0.29	-0.24	-0.27
	$\theta[Al(OH)_3]$=1	-0.04	-0.04	-0.05
	$\theta[H_2O]$=1	-0.19	-0.17	-0.19
2^{nd}	$\theta[H_2O]$=0	-0.09	-0.02	-0.06
	$\theta[Al(OH)_3]$=1	+0.04	+0.03	+0.03
	$\theta[H_2O]$=1	+0.09	+0.07	+0.08
3^{rd}	$\theta[H_2O]$=0	-0.11	-0.03	-0.08
	$\theta[Al(OH)_3]$=1	+0.01	0	0
	$\theta[H_2O]$=1	+0.05	+0.04	+0.03
4^{th}	$\theta[H_2O]$=0	+0.36	+0.16	+0.24
	$\theta[Al(OH)_3]$=1	0	+0.02	0
	$\theta[H_2O]$=1	+0.04	+0.02	+0.03

Table 11.: Distance (Å) calculated between surface Al^{3+} and CO molecule (denoted as Al-CO) and CO bond length (Å) with the def2-TZVPP basis set (Reproduced from S. Gojare *et al.* [154] (2025), *ChemPhysChem* under the terms of the CC-BY license).

Surface	Al-CO (Å)				CO (Å)			
	PBE	B3LYP	PBE0	MP2	PBE	B3LYP	PBE0	MP2
$\theta[H_2O]$=0	2.17	2.18	2.19	2.18	1.13	1.12	1.12	1.13
$\theta[Al(OH)_3]$=1	3.47	3.56	3.53	3.57	1.14	1.13	1.13	1.14
$\theta[H_2O]$=1	4.24	4.32	4.27	4.36	1.14	1.13	1.13	1.14
$CO_{(g)}$	-	-	-	-	1.14	1.13	1.12	1.14

4.1.2.4. Comparison with experiment

In the experiment (described in the introduction section), partial hydroxylation of α-Al_2O_3 surface was observed. However, $\theta[Al(OH)_3]$=1 and $\theta[H_2O]$=1 surfaces are fully saturated with OH groups and thus do not represent the experimental scenario. Hence, to illustrate the low coverage of hydroxyl groups, one single H_2O molecule was added to the $\theta[H_2O]$=0 surface in 1-2 dissociated configuration, i.e. one hydroxyl group

attached to the central Al^{3+} cation and a proton to the nearby oxygen ion (denoted as θ[[H_2O=0]+OH+H]) (see Figures 38(d) and 37 (d)). The analysis of the CO binding mode on this model showed that CO interacts weakly with the hydroxyl group with BE in the range of -0.25 to -0.3 eV (no BSSE correction included).

The distinctive CO interaction with the OH group on θ[[H_2O=0]+OH+H]) model was further analyzed and compared with the other two hydroxylated surfaces, θ[$Al(OH)_3$]=1 and θ[H_2O]=1. The analysis was carried out by comparing the distances between C and O atoms of the CO molecule with the surface H atom of the nearest hydroxyl group (denoted as $C_{(CO)}$-$H_{(surface)}$ and $O_{(CO)}$-$H_{(surface)}$) (see Figure 37 for the assigned atom numbers and Table 12). From Table 12, it can be seen that the shortest distance between $C_{(CO)}$-$H_{(surface)}$ calculated for θ[$Al(OH)_3$]=1, θ[H_2O]=1, and θ[[H_2O=0]+OH+H] surfaces are 2,7, 2,3 and 2,3 Å respectively which is shorter than the sum of their Van der Waals radii [155]. In contrast, the $O_{(CO)}$-$H_{(surface)}$ distance calculated for all the surfaces is greater than 3 Å in most of the cases (longer than the sum of their van der Waals radii). Thus, it shows the presence of a weak OH-CO hydrogen bond on all three surfaces, in agreement with the experimental observations. Additional calculations were carried out with hybrid functionals without including dispersion corrections to check whether they play a role in OC-HO weak interaction. The results showed that the CO molecule does interact with the hydroxyl group with a bond length of 2.44 Å indicating an OC-HO interaction.

Table 12.: The bond length (Å) between CO molecule and surface OH group (denoted as $O_{(CO)}$-$H_{(surface)}$ and $C_{(CO)}$-$H_{(surface)}$) present on θ[[H_2O=0]+OH+H], θ[$Al(OH)_3$]=1, θ[H_2O]=1 surfaces. All values are calculated with the def2-TZVPP basis set (Reproduced from S. Gojare *et al.* [154] (2025), *ChemPhysChem* under the terms of the CC-BY license).

Surface	Atoms	$O_{(CO)}$-$H_{(surface)}$ (Å)			$C_{(CO)}$-$H_{(surface)}$ (Å)		
	(X:$O_{(CO)}$ / $C_{(CO)}$)	PBE	B3LYP	PBE0	PBE	B3LYP	PBE0
θ[$Al(OH)_3$]=1	X-H_1	2.62	2.61	2.64	3.18	3.23	3.25
	X-H_2	3.11	3.06	3.09	3.09	3.1	3.12
	X-H_3	3.78	3.77	3.74	2.68	2.72	2.68
	X-H_4	3.56	3.53	3.55	3.12	3.16	3.17
θ[H_2O]=1	X-H_1	3.17	3.17	3.14	3.15	3.17	3.19
	X-H_2	3.67	3.74	3.7	2.97	3.1	3.12
	X-H_3	3.17	3.23	3.23	3.13	3.21	3.24
	X-H_4	3.24	3.32	3.33	2.24	2.29	2.27
θ[[H_2O=0]+OH+H]	X-H	3.25	3.42	3.31	2.32	2.33	2.33

4.1.2.5. CO vibrational frequency

The computed CO vibrational frequency shift in comparison to $CO_{(g)}$ using the embedded cluster model along with the results of periodic boundary condition computations (calculated in the group of PD Dr. Philipp Plessow) at low CO coverages is shown in Figure 39.

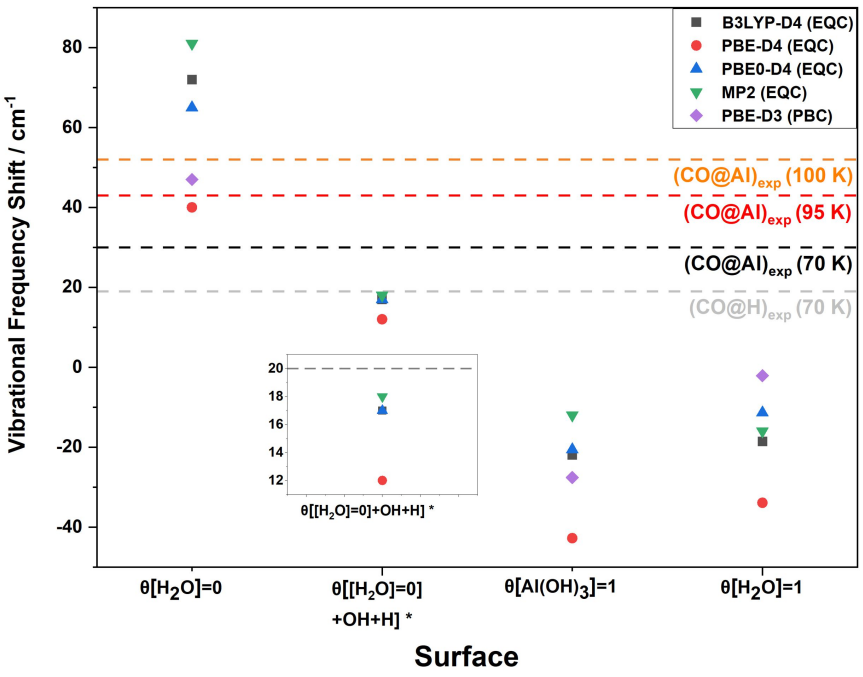

Figure 39.: CO vibrational frequency shift with respect to CO vibrational frequency in the gas phase obtained on the three α-Al_2O_3 (0001) surfaces and calculated with different DFT functionals and the MP2 method in conjunction with the def2-TZVPP basis set. The horizontal lines mark the experimental data. The CO frequencies using the model θ[[H_2O=0]+OH+H] with CO adsorbed on hydroxyl group (denoted θ[[H_2O]=0]+OH+H]*) are also included. For θ[H_2O]=0 surface, the frequencies were calculated for cluster with shells relaxed until the 3^{rd} shell while for θ[Al(OH)$_3$]=1, θ[H_2O]=1 and θ[[H_2O]=0]+OH+H] surfaces, frequencies were computed for cluster with shells relaxed until 2^{nd} shell (Reproduced from S. Gojare *et al.* [154] (2025), *ChemPhysChem* under the terms of the CC-BY license).

All theoretical data is compared with the experimental values at different temperatures. As computations are carried out for low CO coverages, the theoretical values are comparable with the experimental data at 100 K in the case of θ[H_2O]=0 surface. The vibrational frequency shift calculated for the CO interaction with the Al^{3+} site on the θ[H_2O]=0 surface was seen to be blue-shifted which is in agreement with the experimental observation at 100 K (Figure. 33). The frequency shift computed using hybrid functionals and MP2 showed a large shift compared to the PBE functional. The vibrational frequency

shift for the CO interaction with the OH group of the θ[[H_2O=0]+OH+H] model was seen to be blue-shifted and is in good agreement with the experimental results measured at the temperature of 70 K. However, the vibrational shift determined for θ[$Al(OH)_3$]=1, θ[H_2O]=1 surfaces were seen to be red-shifted which deviates from the experimental observation. The same observations were also reported in the periodic DFT calculations. Hence it can be deduced that the θ[[H_2O=0]+OH+H] model which illustrates the partial hydroxylated α-Al_2O_3 surface with low CO and hydroxyl group coverage, is in good agreement with the experiment.

4.1.2.6. Discussion

Our results in this study show the dependence of surface terminations of α-Al_2O_3 on the CO properties such as binding energies and vibrational frequencies. The comparison of the computed data for θ[H_2O]=0 and θ[[H_2O=0]+OH+H] surfaces is in good agreement with the trends observed in the experiment at temperatures of 70 and 100 K. A summary of all the computed values such as CO BE (BSSE correction included) and CO vibrational frequency shifts is summarized in Table 13 along with the experimental data. As mentioned previously, all the reported values for CO properties are computed using default parameters in TURBOMOLE. Therefore, a detailed analysis regarding the influence of different parameters such as grid size, BSSE correction, and diffuse basis set on the values of the CO properties was evaluated.

Table 13.: Summary of the results for the CO binding energy (eV) (BSSE corrected) and CO vibrational frequency shift $\Delta\nu$(CO) (cm^{-1}) on two different surfaces, θ[H_2O]=0 and θ[[H_2O=0]+OH+H] with one adsorbed CO molecule in the EQC approach. All values are computed using def2-TZVPP basis set. Experimental data is also provided for comparison. Superscript *a* and *b* denotes the calculations carried out using grid size m3 and m4 respectively (Reproduced from S. Gojare *et al.* [154] (2025), *ChemPhysChem* under the terms of the CC-BY license).

Surface	CO properties	Exp. values	Method			
			PBE	B3LYP	PBE0	MP2
θ[H_2O]=0	BE (eV)	-0.31	-0.55^a -0.55^b	-0.71^a -0.75^b	-0.55^a -0.60^b	-0.38^a -0.39^b
	$\Delta\nu$(CO)(cm^{-1})	52^{100K}	40	72	65	81
θ[[H_2O=0]+OH+H]	BE (eV)	-0.26	-0.29^a -0.22^b	-0.35^a -0.27^b	-0.27^a -0.2^b	-0.21^a -0.21^b
	$\Delta\nu$(CO)(cm^{-1})	19^{70K}	12	17	17	18

BSSE: The determination of the CO BE on the α-Al_2O_3 surface in the experiment has shown a negligible energy difference of only 0.04 eV between the interactions of CO with Al^{3+} and OH sites (Table 13). In contrast, the CO BE (without BSSE corrections included) calculated for both the scenarios using the EQC model amounted to an energy difference of ≈0.8 eV which deviates from the reported experimental value. On the other hand, PBC calculations also resulted in a similar trend where energy differences of ≈0.8

eV were seen for CO@Al^{3+} and CO@O^{2-} interactions and CO interaction with -OH groups resulted in a BE less than ≈0.4 eV respectively [156]. This shows that the results obtained from the EQC models is in well agreement with the PBC calculations. One of the reasons for the deviation of the EQC results might arise from the BSSE in the CO BE (section 4.1.2.2). Due to the usage of finite basis sets in the computations, inclusion of the BSSE correction is essential while calculating the BE [157]. Thus, the counterpoise (CP) correction of Boys and Bernadi [152] was used. Table 13 gives BSSE corrected CO BE values. When comparing the CO BE on the $\theta[H_2O]$=0 surface with and without BSSE correction, it is seen that the BSSE contribution to the BE is approximately 52 %, which is a quite large contribution to compute accurately. However, the BSSE contribution in the CO BE on θ[[H_2O=0]+OH+H] model was only ≈10 % of the BE. Thus, it shows that the BSSE correction has to be correctly incorporated into the calculation of the binding energies.

In general, the BSSE gets smaller with the usage of a larger basis set [157]. A test calculation on CO at the $\theta[H_2O]$=0 surface (optimized using def2-TZVPP) was carried out in which the BSSE contribution for each fragment, CO and the cluster was analyzed. The result showed that the BSSE of CO was small and did not change much with increasing the basis set on the cluster. In contrast, the BSSE on the cluster was rather large. Thus, to improve the BSSE convergency in the $\theta[H_2O]$=0 surface, the basis set size was sequentially incremented in each step on the cationic and anionic sites near the adsorption site of the optimized geometry (obtained using def2-TZVPP basis set). A constant def2-TZVPP basis set was employed on the CO molecule. A single-point calculation was carried out in each step. Then the CO BE without (denoted as noCP) and with (denoted as CP) counterpoise correction for different basis set compositions were calculated. Table 14 contains the information on the employed basis set on each site and the corresponding CO BE values calculated at each step. From the Table, it can be seen that using the def2-TZVPP basis set led to a CO BE of -1.14 eV (noCP) and -0.71 eV (CP). The difference (denoted as Δ(BE)) between the non-corrected and CP-corrected values is 0.41 eV. Thus, in the next step, a diffuse def2-TZVPPD basis set was used to improve the description of the electrons in the O^{2-} sites near the adsorption site [157]. However, it can be seen that the addition of a diffuse basis set on the oxygen sites increased the CO BE by 0.14 eV with still a large contribution (≈50 %) of BSSE to the CO BE. Further increase of the basis (def2-QZVPP) on the cationic site led to a Δ(BE) of 0.54 eV. Following this approach, it can be seen that irrespective of the increase in the basis functions on the cationic and anionic sites, the Δ(BE) remains constant at a value of 0.54 eV. This large difference between noCP and CP values shows that convergency is not achieved. This might be due to the large number of ECPs added on the Al^{3+} cations in the shells further away from the adsorption site, which can lead to difficulty in reaching a smooth convergence. Therefore, along with the def2-TZVPPD basis set on O^{2-} sites, the small def2-SVP basis sets were used for the 3^{rd} shell consisting of Al^{3+} cations. The calculated CO BE was further reduced to -1.2 eV. The reason for not reaching the smooth convergence between the non-corrected and the CP-corrected CO BE might arise from the extensive use of the ECPs at the boundary of the cluster.

Table 14.: The computed CO binding energy on $\theta[H_2O]$=0 surface using Karlsruhe def2-XVPP (X-SV,TZ, QZ) basis set compositions with (CP) and without counterpoise corrections (noCP). Δ(BE) denotes the energy difference (eV) between the energy values calculated with and without counterpoise corrected. All these values are calculated using B3LYP DFT functional.

Atoms	Basis set					
CO	TZVPP	TZVPP	TZVPP	TZVPP	TZVPP	TZVPP
Al	TZVPP	TZVPP	QZVPP	QZVPP	QZVPP	TZVPP
O_{1-3}	TZVPP	TZVPPD	TZVPPD	QZVPP	QZVPPD	TZVPPD
Al (2^{nd} shell)	ECP	ECP	ECP	ECP	ECP	SVP
BE (eV) (noCP)	-1.14	-1.28	-1.16	-1.25	-1.12	-1.2
BE (eV) (CP)	-0.71	-0.74	-0.63	-0.61	-0.57	-
Δ(BE) (eV)	0.41	0.54	0.54	0.64	0.54	-

Grid size: Furthermore, the influence of the grid size was also evaluated. The CO BE calculated using the default m3 grid size (denoted with superscript a) along with density convergence set to 10^{-6} was compared with a more dense grid m4 size (calculations done by Dr.Juana Vázquez Quesada) (denoted with superscript b) along with a tight density convergence set to 10^{-8}. Other parameters were kept the same. As seen in the Table 13, the computed values with grid size m4 (denoted with superscript b) and hybrid functionals on $\theta[H_2O]$=0 surface show an increase in CO BE of $\approx$0.04 eV compared to the ones calculated with grid size m3. No change in the computed values using GGA functional was observed. In contrast, BE calculated on θ[[H_2O=0]+OH+H] model showed a decrease of $\approx$0.08 eV when grid size m4 is employed. Thus, the results obtained by using both grids m3 and m4 show similar trends along with $\leq$0.1 eV energy differences between the respective calculated values. Grid size m4 are more reliable as it is more dense grid compared to grid size m3.

In the analysis of the CO vibrational frequency shift, it can be seen that the frequency shifts calculated on the $\theta[H_2O]$=0 surface using hybrid functionals and MP2 are larger compared to the PBE functional. One of the reasons for such an observation can be that computations are carried out for low CO coverages while the CO coverage might still be higher in the experiment, which can cause the deviations.

Thus, from all different analyses, it is seen that different parameters do influence the values of the CO BE. Therefore, a detailed benchmark study is essential to judge the accuracy of the calculations. However, the results obtained by employing the EQC model agree well with the experimental trends and the PBC data, thus enabling the usage of different levels of theory.

4.1.3. Conclusion

In this project, the surface structure and reactivity of the Al-terminated α-Al_2O_3 surface were studied using an embedded cluster model. Three different hydroxylation coverages on α-Al_2O_3 surface, $\theta[H_2O]$=0 (water free), $\theta[Al(OH)_3]$=1 (fully hydroxylated) and $\theta[H_2O]$=1 (H_2O dissociated) were investigated with low CO coverage. According to the analysis of the CO binding mode, CO was seen to bind strongly to the surface Al^{3+} cation which is facilitated by the charge transfer from the molecule to the surface and preferring a perpendicular orientation. On the $\theta[Al(OH)_3]$=1 and $\theta[H_2O]$=1 surfaces, the CO molecule was seen to be weakly adsorbed on the surface and mainly stabilized by the weak electrostatic interactions with the surrounding hydroxyl groups via OC-HO hydrogen bonding. However, the wavefunction-based MP2 method did not well describe the weak interaction on the $[Al(OH)_3]$=1 and $\theta[H_2O]$=1 surface. Therefore, analysis with higher correlation methods is needed to accurately predict the CO interactions. The θ[[H_2O=0]+OH+H] model illustrated the partial hydroxylation scenario quite well and the results agreed well with the experimental observations. The CO vibrational frequency was significantly blue-shifted for CO interaction with Al^{3+} cations and on low hydroxyl coverage.

4.2. CO_2 adsorption on α-Al_2O_3 surface

4.2.1. Experiment

The IRRAS experiments carried out on partially hydroxylated α-Al_2O_3 single crystals in the group of Dr. Yuemin Wang (IFG, KIT), showed that at low CO_2 dose of 0.5 L and at a temperature of 65 K, both the p- and s- polarization of the IRRAS data consisted a characteristic peaks at 2340 cm^{-1} (Figure 40) arising from the monolayer adsorption of the CO_2 molecules. The IR-adsorption bands arising from the adsorbates interacting with the dielectric surface are positive or negative in relation to the orientation of the relevant transition dipole moment (TDM). In p-polarized light, the positive adsorption bands arise from the molecular vibrations with a component of the TDM parallel to the surface while the negative adsorption bands arise from the vibrations with a component perpendicular to the surface. In contrast, the adsorption bands of the s-polarized light is always negative when the component of the vibration is parallel to the surface and becomes zero perpendicular to the surface. As its seen in Figure 40, due to the presence of the peak in both p- and s-polarization data, it is estimated that the molecule was present in almost parallel orientation and weakly physisorbed onto the surface. No formation of surface carbonate was observed in the experiment.

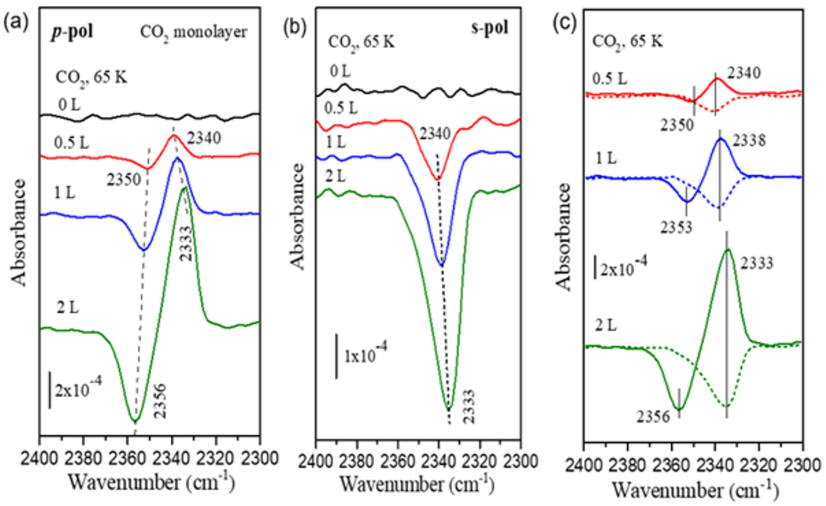

Figure 40.: IRRAS data of CO_2 adsorption (0-2 L) at 65 K on α-Al_2O_3 (0001) single crystal at a grazing incidence angle of 80°: (a) p-polarized light incident; (b) s-polarized light incident. (c) Comparison of IRRAS data of sub-monolayer and monolayer adsorption of CO_2 adsorption at 65 K on α-Al_2O_3 (0001) single crystal: solid lines-p-polarized light incident; dashed lines-s-polarized light incident [Figure provided by Dr. Yuemin Wang].

Further in-depth investigation of the CO_2 adsorption and interaction with the α-Al_2O_3 surface depending on the variation in hydroxyl group coverages was carried out by

employing DFT along with the embedded quantum cluster method. The variance in CO_2 properties with respect to the variation in hydroxyl group coverages was analyzed. Particularly, the following study focused on the low CO_2 coverages (0.5 L dose in the experiment). The CO_2 properties such as binding mode, binding energies, and vibrational frequencies were computed and compared with the experimental data at different levels of theory.

4.2.2. Computational details

In this study, the dry surface (denoted as $\theta[H_2O]$=0) and the fully hydroxylated surface (denoted as $\theta[Al(OH)_3]$=0) were considered along with one adsorbed CO_2 molecule to study the interactions at low CO_2 coverages. To examine intermediate hydroxyl coverages, the $\theta[H_2O]$=0 cluster (shown in Figure 34) was further modified by adding one dissociated water molecule (denoted as θ[[H_2O=0]+OH+H] model). Details are discussed in Chapter 4.1. Alumina and oxygen centered cluster geometries were used depending on the interaction of the CO_2 molecule with different sites. The values used for scaling the harmonic CO_2 vibrational frequencies were 0.9938 for PBE, 0.9748 for B3LYP, and 0.9571 for PBE0. The basis set superposition error (eq. 70) was also incorporated in the calculation of the CO_2 BE. Grid size m4 was used for calculating the CO_2 BE.

4.2.3. Results and Discussion

4.2.3.1. Layer relaxation in α-Al_2O_3 (0001) surface

The clusters used for calculating the water-free (θ[[H_2O]=0), the surface with one dissociated H_2O molecule on water-free surface (θ[[H_2O=0]+OH+H] model) and the fully hydroxylated ($\theta[Al(OH)_3$=1) surface are shown in Figure 41. It is well known that the top-most layer of the α-Al_2O_3 (0001) surface undergoes a strong relaxation due to the unsaturation of the surface atoms [117, 158]. Therefore, a thorough analysis of the generated clusters was conducted to check if they reproduce the same phenomenon in the top-layer. As shown in the figure, Al_1, O_1, O_3, O_5 atoms highlighted in black are exposed in the top layer and are unsaturated compared to the ones in the bulk (shown in blue color). The atoms Al_{2-7} and $O_{2,4,6}$ highlighted in blue color are the ones situated in the layer beneath the top layer and are saturated atoms. The coordinates of all these atoms in both of the clusters were optimized.

The computed values for the atomic displacements in each cluster are given in Table 15. The computations for the water-free cluster (Figure 41(a)) are in good agreement with the experimental observations [108, 159] where there is significant displacement of the surface atoms towards the bulk, nearly bond-length-conserving displacement [114]. The surface Al-atoms moved downwards with respect to the surface normal while the O-atoms in the second layer move outwards to conserve the Al-O bond length. The

Al-atoms distant from the central Al atom are seen to be less affected compared to Al_1 at the cluster center.

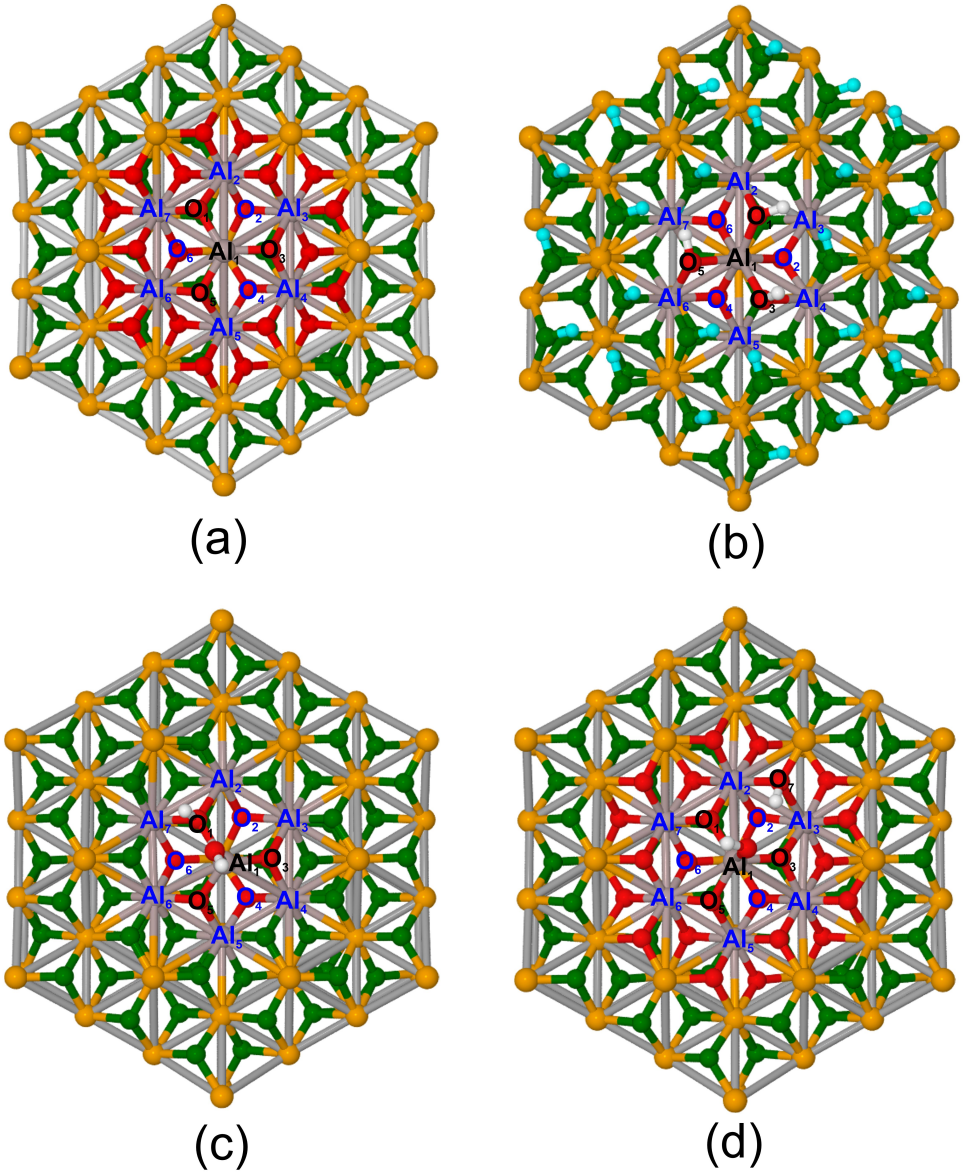

Figure 41.: Schematic of clusters (a) water-free, (b) fully hydroxylated, (c) θ[[H_2O=0]+OH+H] containing 1-2 dissociated H_2O and (d) θ[[H_2O=0]+OH+H] containing 1-4 dissociated H_2O molecule. They are optimized using the B3LYP functional and the def2-TZVPP basis set. The labels in black denote unsaturated atoms and in blue denote saturated atoms. (Color scheme of atoms: yellow-fixed Al, grey-unfixed Al, green-fixed oxygen, red-unfixed oxygen, white-unfixed hydrogen, cyan-fixed hydrogen).

The results show relaxations of the water-free surface varying from 0.04 to 0.5 Å depending on the extent of atomic unsaturation. In the case of the θ[[H_2O=0]+OH+H]

model, two different clusters were generated depending on the adsorption sites of the dissociated H_2O molecule: 1-2 or 1-4 configuration.

Table 15.: Atomic displacement (Å) calculated for the water-free surface (θ[[H_2O]=0), one dissociated H_2O molecule on the water-free surface (θ[[H_2O=0]+OH+H] model) in 1-2 and 1-4 configuration (see text for description) and the fully hydroxylated (θ[$Al(OH)_3$]=1) surface computed using the def2-TZVPP basis set (Please refer to Figure 41 for the atom numbers considered for the calculations).

Atoms	Atomic displacement (Å)								
	Water-free			θ[[H_2O=0]+OH+H] 1-2/1-4			Fully hydroxylated		
	PBE	B3LYP	PBE0	PBE	B3LYP	PBE0	PBE	B3LYP	PBE0
Al_1	-0.45	-0.4	-0.49	0.48/ -0.15	0.45/ -0.1	0.43/ -0.11	-0.04	-0.06	-0.07
O_1	-0.06	-0.1	-0.11	-0.02/ -0.06	-0.04/ -0.04	-0.06/ -0.04	-0.03	-0.03	-0.07
O_2	0.02	0.01	0.01	-0.01/ 0.06	-0.01/ 0.05	-0.01/ 0.05	-0.01	-0.01	-0.01
O_3	-0.07	-0.1	-0.11	-0.09/ -0.11	-0.12/ -0.07	-0.13/ -0.07	-0.03	-0.05	-0.06
O_4	0.02	0.01	0.01	-0.04/ 0.03	-0.05/ 0.03	-0.05/ 0.03	-0.01	-0.02	-0.02
O_5	-0.07	-0.1	-0.11	-0.1/ 0.03	-0.13/ 0.00	-0.15/ 0.01	-0.05	-0.08	-0.09
O_6	0.02	0.01	0.01	-0.03/ 0.05	-0.04/ 0.05	-0.04/ 0.05	0	-0.01	-0.01
Al_2	-0.03	-0.04	-0.04	-0.08/ -0.04	-0.09/ -0.04	-0.1/ -0.04	-0.05	-0.06	-0.05
Al_3	0.04	0.01	0.01	0.03/ 0.08	0.01/ 0.05	0.01/ 0.05	-0.03	-0.03	-0.03
Al_4	-0.03	-0.04	-0.04	-0.06/ -0.05	-0.07/ -0.03	-0.07/ -0.03	-0.07	-0.06	-0.07
Al_5	0.04	0.01	0.01	0.01/ 0.05	-0.02/ 0.03	-0.02/ 0.04	-0.03	-0.03	-0.03
Al_6	-0.03	-0.04	-0.04	-0.04/ 0.00	-0.05/ -0.01	-0.06/ -0.01	-0.08	-0.08	-0.08
Al_7	0.04	0.01	0.01	-0.09/ 0.03	-0.11/ 0.03	-0.11/ 0.03	-0.03	-0.03	-0.03

In 1-2 configuration, the OH^- binds to the surface Al^{3+} cation and the proton binds to the directly neighboring O^{2-} site (Figure 41(c)). While in the 1-4 configuration, the OH^-

binds to the surface Al^{3+} cation and the proton binds to the next neighboring O^{2-} site (Figure 41(d)). The data in Table 15 shows that in the case of the 1-2 configuration, the Al_1 surface atom is pulled outwards due to the bonding with the hydroxyl group. The charge of -0.25 $|e|$ was transferred from the surface to the dissociated water molecule. O_{1-6} and Al_{2-7} are displaced downwards towards bulk, similar to the behavior of the θ[[H_2O]=0 surface. However, in the 1-4 configuration, the displacement of the Al_1 atom is relieved by ≈0.1 Å and the O^{2-} atom is seen to move upwards by ≈0.05 Å . According to the energetics, the 1-4 configuration is less stable by ≈0.4 eV than the 1-2 configuration. The result is in agreement with the literature [146]. Therefore, for further studies, the 1-2 configuration of the θ[[H_2O=0]+OH+H] model is taken into account. The relaxations in the fully hydroxylated surface are comparatively negligible due to the full saturation of the surface atoms [159] (Figure 41 (b)).

4.2.3.2. CO_2 binding mode on the water-free surface

Firstly, the defect-free Al-terminated water-free (θ[H_2O]=0) surface was considered for the adsorption of the CO_2 molecule. Previous studies have shown that CO_2 interacts with both acidic and basic surface sites. Therefore, two different clusters were generated depending on the central adsorption sites, (a) with Al^{3+} and (b) with O^{2-} for the CO_2 adsorption (Figure. 42). Initially, both the clusters were relaxed until the 3^{rd} shell using the def2-TZVPP basis set and were further used for the CO_2 molecule adsorption. The test calculation on the contribution of the different cluster shapes on the molecule's binding energy was seen to be negligible.

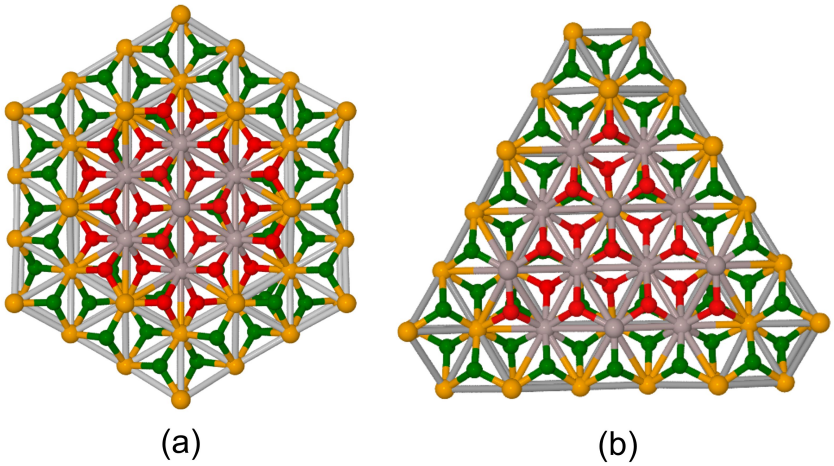

Figure 42.: Schematic of cluster sizes for the water-free surface, (a) Al centered, (b) O-centered cluster. (Color scheme of atoms: yellow-fixed Al, grey-unfixed Al, green-fixed oxygen, red-unfixed oxygen).

As mentioned previously, CO_2 binds in different configurations depending on the adsorption sites. The results from the geometry optimizations the following two configurations

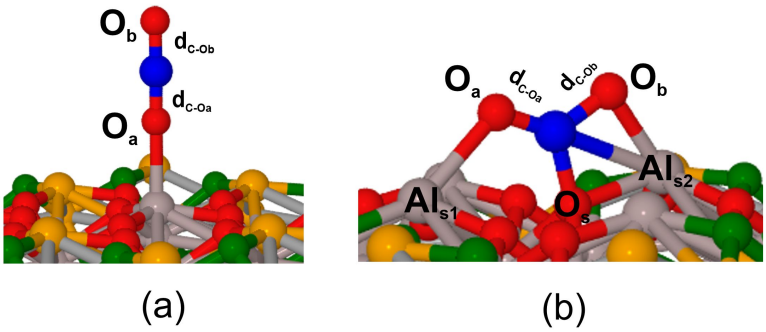

Figure 43.: Schematic of CO_2 binding modes on water-free surface, (a) CO_2 interacting with acidic Al^{3+} site, (b) CO_2 interacting with basic O^{2-} site. (Color scheme of atoms: yellow-fixed Al, grey-unfixed Al, green-fixed oxygen, red-unfixed oxygen, blue-carbon).

to be most stable: (a) Linear adsorbed CO_2 and (b) tridentate carbonate (Tri) shown in Figure 43 and their corresponding binding energies are given in Table 16.

Table 16.: CO_2 binding energies (eV) calculated for the water-free surface depending on the interaction sites. All values are calculated using the def2-TZVPP basis set and are BSSE corrected.

Site of interaction	CO_2 binding energy (eV)		
	PBE	B3LYP	PBE0
O^{2-}	-0.92	-1.14	-1.13
Al^{3+}	-0.26	-0.57	-0.36

After comparing the CO_2 binding energies (given in Table 16) in these two configurations, it is clear that the tridentate carbonate is more stable compared to the linear configuration. In the linear configuration, the CO_2 molecule binds weakly to the surface Al^{3+} atom via oxygen (O_a) with a bond length of ≈2.02 Å. In the tridentate carbonate (Tri) configuration, the two oxygens of the CO_2 molecule are bound to the surface Al^{3+} atoms, and the carbon atom is bound to the Lewis basic site O^{2-} at a distance of 1.4 Å. The structural changes in the cluster geometry and the CO_2 molecule upon its adsorption were studied by calculating the atomic displacement of the Al^{3+} cation and O_s at the adsorption site, changes in the O-C-O bond angle and the internal CO_2 bond lengths. The calculated values are given in Table 17. The influence on the CO_2 structural properties upon adsorption shows that in the linear orientation, the C-O bond length is not affected much compared to $CO_{2(g)}$. The computed O-C-O bond angle is also 180° at all levels of theory. However, there is some influence on the relaxation of the Al^{3+} cation at the adsorption site. The Al^{3+} relaxation is relieved upon adsorption. The surface Al is observed to be pulled out by ≈0.4 Å . In the tridentate carbonate configuration, the geometrical analysis shows that both the adsorbate and substrate are significantly

perturbed upon chemisorption. The CO_2 molecule adsorption led to the elongation of O_s-Al_{s2} from 1.69 Å in the clean surface to 1.91 Å in the adsorbed configuration. The additional new bonds formed between the molecule and the surface led to stronger binding strength. The C-O bond lengths were also affected, leading to a significant elongation and the molecule is strongly bent with the bond angle of ≈130 °. The inward relaxation of both the surface Al atoms is seen to be relieved with displacement in an upward direction.

Table 17.: Comparison of the structural parameters in the CO_2 molecule such as CO_2 bond length (BL) (Å) between O_a-C-O_b (d_{C-Oa}/d_{C-Ob}), O-C-O bond angle (°), atomic displacement (Δr) (Å) of the two stable sites Al_{s2} and O_s in both the configurations shown in Figure 43.

	d_{C-Oa}/d_{C-Ob}(Å)			O-C-O angle (°)			Δr (Al_{s2} / O_s) (Å)		
	PBE	B3LYP	PBE0	PBE	B3LYP	PBE0	PBE	B3LYP	PBE0
Linear	1.17 /1.16	1.16 /1.15	1.16 /1.15	180	180	180	0.34	0.42	0.44
Tri	1.23 /1.29	1.22 /1.28	1.22 /1.28	130	131	130	0.74 /0.14	0.53 /0.14	0.69 /0.14
$CO_{2(g)}$	1.17	1.16	1.16	180	180	180	-	-	-

The charge distributions in the stable CO_2/α-Al_2O_3 configurations were determined by calculating the charges using natural population analysis [91](Table 18). The net electronic charge transferred from the surface to the linearly adsorbed CO_2 is almost neutral showing weak molecular interaction with the surface, a physisorption phenomenon. This can be due to the structural integrity of the Al_2O_3 surface and the non-polar nature of the CO_2 molecule. Thus the contribution of the CO_2 molecule interaction with the Lewis acid site to the combined interaction is expected to be negligible. However, in some former theoretical studies, the tilting in the CO_2 molecular axis was seen which is not observed in the present calculations [124, 158]. In tridentate carbonate configurations the net electronic charge transfer is 0.39 $|e|$ showing that CO_2 predominantly acts as a Lewis acid and thus accepts the electrons from the surface revealing the strong chemisorption phenomenon.

Table 18.: Atomic charges (in $|e|$) computed for different CO_2 adsorption configurations on the water-free surface (shown in Figure 43), isolated CO_2 molecule and the bare clusters. These values are computed using B3LYP and def2-TZVPP basis set. (Δ is the difference between the atomic charges before and after CO_2 adsorption).

Model	Cluster	Atom	Charge	Δ
$CO_{2(g)}$		C	0.98	
		O_a	-0.49	
		O_b	-0.49	
Al_2O_3	Linear	Al_1	2.22	
	Tri	O_s	-1.7	
		Al_{s1}	2.56	
		Al_{s2}	2.59	
CO_2/Al_2O_3	Linear	Al_1	2.50	0.28
		C	2.03	1.05
		O_a	-0.99	-0.5
		O_b	-0.98	-0.49
	Tri	O_s	-1.27	0.43
		Al_{s1}	2.57	0.01
		Al_{s2}	2.57	-0.02
		C	1.99	1.01
		O_a	-1.17	-0.68
		O_b	-1.21	-0.72

4.2.3.3. Effect of hydroxylation coverage

The effect of variation in the surface hydroxylation coverage on the CO_2 interaction was studied using two different cluster models, (a) θ[[H_2O]=0]+OH+H] model and (b) θ[Al(OH)$_3$]=1 shown in Figure 44. The θ[[H_2O]=0]+OH+H] model with 1-2 configuration (Figure 41 (c)) was used representing the low hydroxyl coverage while the θ[Al(OH)$_3$]=1 is the fully hydroxylated surface containing one proton on each Lewis base site. Both these clusters were optimized until the 2^{nd} shell using the def2-TZVPP basis set.

The stable CO_2 configuration on the hydroxylated surface is shown in Figure. 45. It can be seen that the CO_2 molecule interacts weakly with the surface hydroxyl groups. The CO_2 BE on the θ[[H_2O]=0]+OH+H] model is weaker by ≈0.12-0.14 eV (depending on the employed DFT functionals) compared to the fully hydroxylated surface (Table 19). This stabilization effect on the θ[Al(OH)$_3$]=1 surface is mainly due to the weak electrostatic interactions exerted by the hydroxyl groups in its vicinity. The presence of hydrogen bonding between CO_2 and the hydroxyl groups can also play a role in molecule stabilization. From the data given in Table 20 and Figure 46, it is evident in both the models that oxygen of the CO_2 molecule interacts with the hydrogen atom of the hydroxyl group. The bond length between O_{CO2}-$H_{surface}$ is ≈2.2 Å which is shorter than the sum of their van der Waals radii (2.5 Å). The structural parameters of

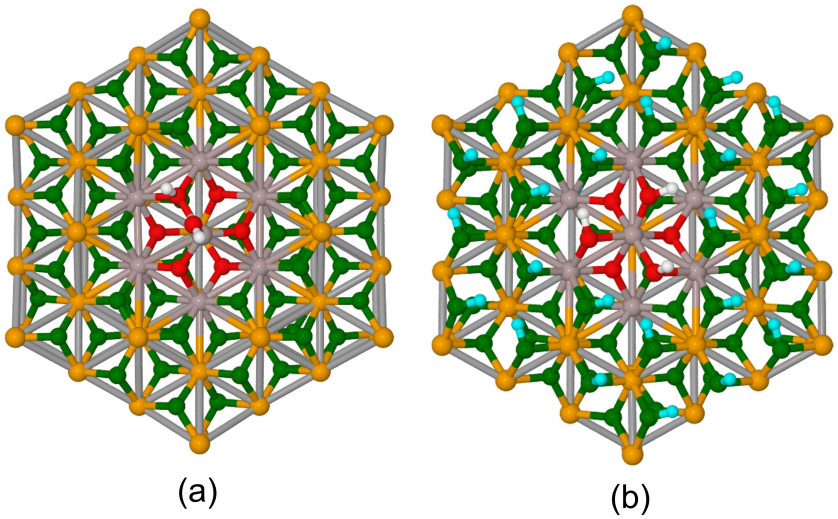

Figure 44.: Schematic of hydroxylated clusters, (a)θ[[H_2O=0]+OH+H] model, (b) Fully hydroxylated (θ[$Al(OH)_3$]=1) (Color scheme of atoms: yellow-fixed Al, grey-unfixed Al, green-fixed oxygen, red-unfixed oxygen, white-unfixed hydrogen, cyan-fixed hydrogen).

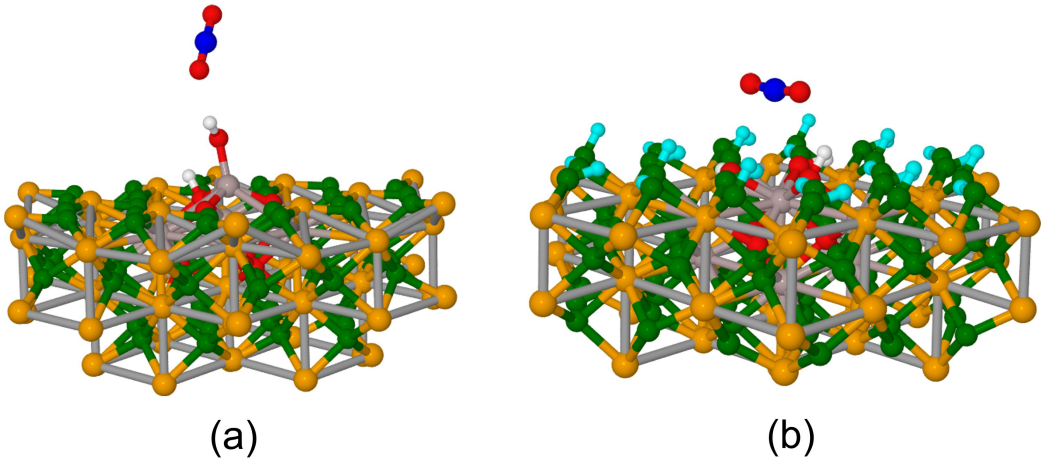

Figure 45.: Schematic of the CO_2 binding configuration on the (a) θ[[H_2O=0]+OH+H] model, (b) fully hydroxylated (θ[$Al(OH)_3$]=1) (Color scheme of atoms: yellow-fixed Al, grey-unfixed Al, green-fixed oxygen, red-unfixed oxygen, white-unfixed hydrogen, cyan-fixed hydrogen, blue-carbon).

CO_2 showed negligible changes upon interaction with the fully hydroxylated surface. The CO_2 orientation on the θ[[H_2O=0]+OH+H] model was almost perpendicular to the surface while on the fully hydroxylated surface it was oriented almost parallel to the surface. Also, negligible effects were seen on the atomic displacement of the Al_1 atom upon CO_2 interaction with the hydroxyl group. No formation of bicarbonate was observed in this study.

Table 19.: CO_2 binding energies (eV) calculated for the θ[[H_2O=0]+OH+H] model and the fully hydroxylated (θ[$Al(OH)_3$]=1) surface. All values are calculated using the def2-TZVPP basis set and are BSSE corrected.

Model	CO_2 binding energy (eV)		
	PBE	B3LYP	PBE0
θ[[H_2O=0]+OH+H]	-0.24	-0.32	-0.23
θ[$Al(OH)_3$]=1	-0.38	-0.44	-0.37

Table 20.: The bond length (Å) between the CO_2 molecule and the surface hydroxyl groups (denoted as O_{CO2}-$H_{Surface}$) present on the θ[[H_2O=0]+OH+H] model and the fully hydroxylated (θ[$Al(OH)_3$]=1) surface. All values are calculated using def2-TZVPP basis set.

Model	Atoms	O_{CO2}-$H_{Surface}$ (Å)		
		PBE	B3LYP	PBE0
θ[[H_2O=0]+OH+H]	O-H_S	2.13	2.16	2.14
θ[$Al(OH)_3$]=1	O_a-H_1	2.18	2.21	2.21
	O_a-H_2	3.02	2.94	2.97
	O_b-H_3	2.25	2.22	2.22
	O_b-H_4	3.19	3.19	3.21

4.2.3.4. Comparison with experiment

The computed vibrational frequencies of the CO_2 molecule on three different surfaces, water-free (θ[H_2O]=0), θ[H_2O=0]+OH+H] model, and fully hydroxylated (θ[$Al(OH)_2$]=1) is shown in Figure 47. The vibrational frequencies computed for CO_2 adsorbed on the θ[H_2O]=0 surface in linear and tridentate carbonate orientations is denoted as $CO_{2(ver)}$/θ[H_2O]=0 and $CO_{2(par)}$/θ[H_2O]=0 respectively. As shown in the figure, the dashed black line denotes the experimental value with 9 cm^{-1} red-shifted with respect to $CO_{2(g)}$. The vibrational frequency shift for the tridentate carbonate configuration is strongly red-shifted with respect to $CO_{2(g)}$. This scenario can be neglected as the formation of carbonate was not observed in the experiment. The vibrational frequency of CO_2 in linear orientation is blue-shifted with respect to $CO_{2(g)}$. This scenario can also be neglected as it deviates from the experimental value. In the case of CO_2 interaction with the hydroxylated θ[H_2O]=0]+OH+H model the vibrational frequencies are slightly blue-shifted with respect to $CO_{2(g)}$. However, in the computations, an imaginary frequency was observed, which indicates that this situation is a saddle point. While on the fully hydroxylated (θ[$Al(OH)_2$]=1) surface, the frequencies are slightly blue-shifted and in better agreement to the small red shift.

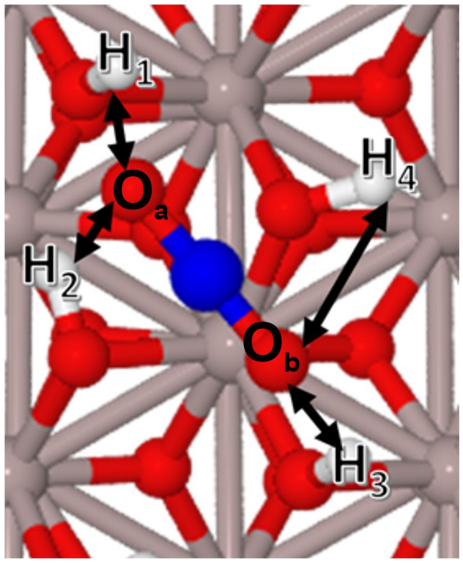

Figure 46.: Top view of the fully hydroxylated (θ[Al(OH)$_3$]=1) surface (shown in Figure 45(b)) showing the interaction between CO_2 and the surface hydroxyl groups in the vicinity (Color scheme of atoms: grey-unfixed Al, red-unfixed oxygen, white-unfixed hydrogen, blue-carbon).

4.2.3.5. Influence of the exchange-correlation functional

Lastly, the influence of the GGA functional, PBE and the hybrid functionals B3LYP and PBE0, on the CO_2 properties will be examined. The general trend for CO_2 binding energies calculated for both sites, Al^{3+} and O^{2-} on the water-free surface show that GGA predicts a slightly lower adsorption energy by ≈0.2 eV compared to the yields of hybrid functionals (Table 16). PBE functional predicts a small binding energy of CO_2 on Al^{3+} site (physisorption) while the hybrid functionals show a quite high adsorption energy, more like a chemisorption scenario (BE ≥ 0.3 eV). In the case of hydroxylated surfaces, all the functionals show a similar trend of the CO_2 BE indicating a weak interaction between CO_2 and the surface. The CO_2 BE is a bit higher on fully hydroxylated surface compared to the θ[H_2O=0]+OH+H model due to the weak electrostatic interactions present between the molecule and the underlying hydroxyl groups leading to the system stabilization. All the functionals showed a similar trend. Further, structural parameters such as atomic displacements along the surface normal, bond lengths and bond angles of all the clusters computed at different levels of theory showed consistent results. In the case of the vibrational frequency analysis, all the functionals showed the same trend in the vibrational frequency shift on the water-free surface and the θ[[H_2O=0]+OH+H] model. However, on the fully hydroxylated surface, the CO_2 vibrational frequency is mainly blue-shifted (7cm^{-1} (B3LYP) and 6cm^{-1} (PBE0)) with respect to the $CO_{2(g)}$. While the frequency shift computed using PBE functional is red-shifted by 5cm^{-1} with respect to $CO_{2(g)}$ which is in good agreement with the experimental observation. In the experiment, the reported CO_2 vibrational frequency is seen to be red-shifted by 9 cm^{-1} (Figure 47). Thus, when comparing the experimental observations with the computational results, it

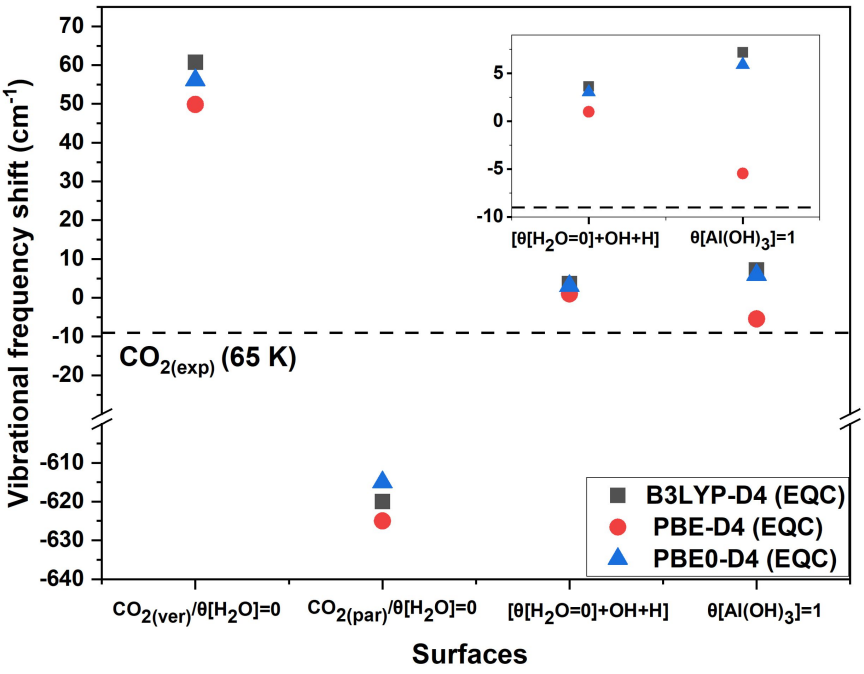

Figure 47.: CO_2 vibrational frequency shift (cm^{-1}) computed on water-free ($\theta[H_2O]$=0), θ[[H_2O=0]+OH+H] model, and fully hydroxylated ($\theta[Al(OH)_2]$=1) surfaces with respect to $CO_{2(g)}$. The dashed black line defines the experimental value determined using the IRRAS technique.

can be concluded that results computed on $\theta[Al(OH)_2]$=1 surface reproduced the trends quite well compared to the other surfaces.

4.2.4. Conclusion

The interaction of the CO_2 molecule with α-Al_2O_3 surface was studied using density functional theory along with an embedded cluster model. Within this study, three different surfaces were analyzed, the water-free ($\theta[H_2O]$=0), the θ[H_2O=0]+OH+H model, and the fully hydroxylated ($\theta[Al(OH)_2]$=1). The influence of the degree of hydroxylation on the CO_2 binding mode was analyzed. On the $\theta[H_2O]$=0 surface, the CO_2 molecule was seen to bind with Al^{3+} and O^{2-} sites forming a linear orientation and a tridentate carbonate respectively. The tridentate carbonate configuration had a relatively high adsorption energy due to the additional interaction with the neighboring Al^{3+} sites via charge transfer leading to the elongation of O-C-O bond lengths and a decrease in the bond angle. Significant surface relaxation was also seen. The linear CO_2 molecule with bonding via oxygen towards the Al^{3+} cation had a weaker interaction than for the tridentate carbonate configuration and a negligible charge transfer. On the other hand, hydroxylated surfaces, θ[[H_2O=0]+OH+H] model and $\theta[Al(OH)_2]$=1, showed a

weaker interaction with the CO_2 molecule and mainly stabilization by the electrostatic interactions with the surface hydroxyl groups. The CO_2 vibrational frequency shift predicted for the fully hydroxylated surface ($\theta[Al(OH)_2]$=1) are in agreement to the experimental data.

4.3. CO adsorption on Pt/α-Al_2O_3 surface

4.3.1. Computational details

Two types of surfaces were taken into account in this study, the water-free surface ($\theta[H_2O]$=0) and the fully hydroxylated ($\theta[Al(OH)_3]$=1) surface to examine the bare surface and influence of hydroxyl groups on the binding modes of Pt and its corresponding effect on the CO interaction. Due to the presence of heavy element Pt in these calculations, scaler relativistic effects were included by using effective core potential for the Pt-core electrons and dhf-TZVPP-2c basis set [89]. All binding energies reported in this chapter are counterpoise corrected to basis set superposition error [152]. Figure 48 shows the cluster generated for water-free surface. The oxygen-centered cluster shown in Figure 48 was used for the adsorption of the Pt atom. The systematic shell relaxation approach (see Chapter 4.1) was used to examine the convergence (Figure 48(a) and (b)). The cluster was first optimized with the small basis set def2-SVP and re-optimized with def2-TZVPP basis set. The re-optimized cluster was then used for the adsorption of the single Pt atom.

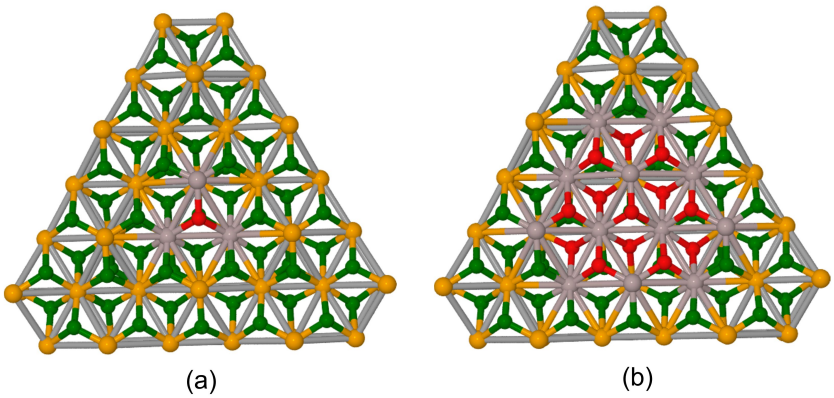

Figure 48.: Schematic of the clusters generated using the sequential shell relaxation approach for the water-free surface with (a) 1^{st} shell, (b) 2^{nd} shell relaxed. Clusters are optimized using the def2-TZVPP basis set (Color scheme of atoms: grey-unfixed Al, yellow-fixed Al, red-unfixed oxygen, green-fixed oxygen).

4.3.2. Results and Discussion

4.3.2.1. Adsorption of Pt atom on α-Al_2O_3 surface

Initially, metal-support interaction (MSI) was examined by placing a single Pt atom on the Al-terminated α-Al_2O_3 cluster model shown in Figure 48. The influence of sequential shell relaxation on the Pt bonding was examined on the water-free surface ($\theta[H_2O]$=0),

relaxing from 1^{st} shell consisting of three Al^{3+} cations and a central O^{2-} until 2^{nd} shell consisting of twelve Al^{3+} and thirteen O^{2-} ions (top and side view shown in Figure 49). The same procedure was followed for the fully hydroxylated surface ($\theta[Al(OH)_3]$=1) (shown in Figure 50).

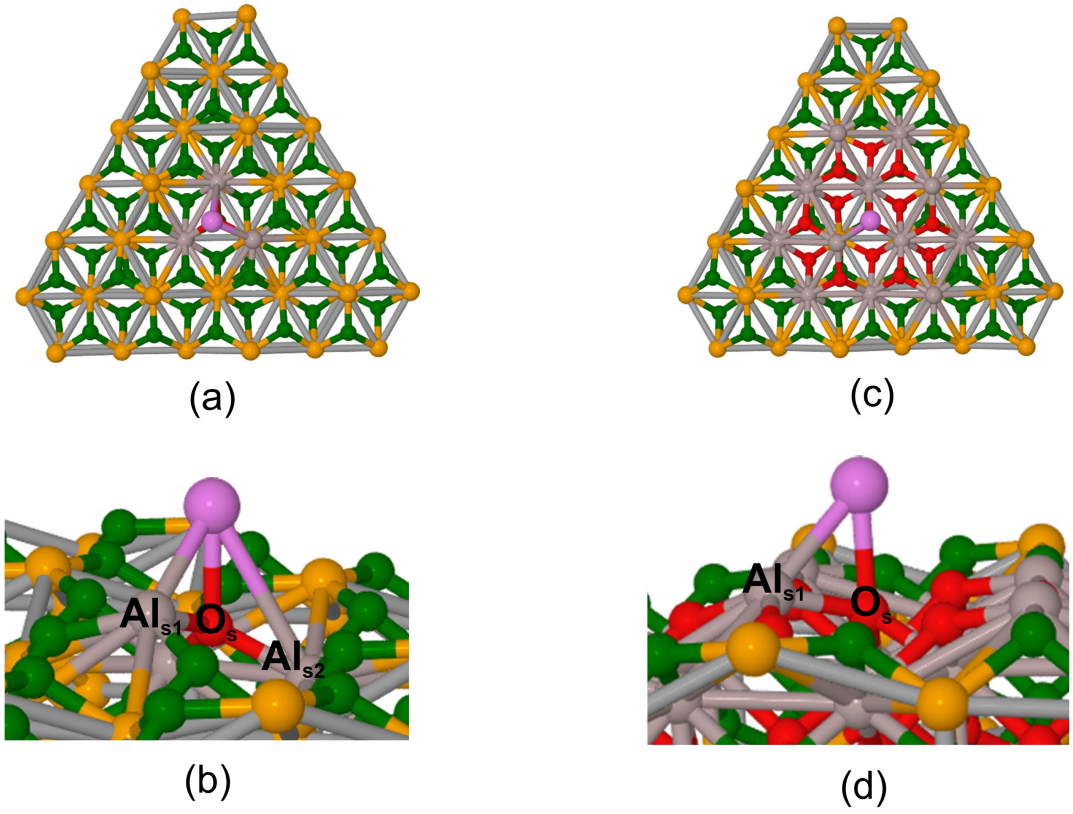

Figure 49.: Schematic of the single Pt atom binding configuration on the water-free surface ($\theta[H_2O]$=0) with relaxation until 1^{st} shell (a (top view),b (side view)) and until 2^{nd} shell (c (top view),d (side view)). All geometries are computed using the def2-TZVPP basis set. (Color scheme of atoms: grey-unfixed Al, yellow-fixed Al, red-unfixed oxygen, green-fixed oxygen, violet-platinum atom).

The single Pt atom was placed at different sites on the Al_2O_3 surface, Al^{3+} and O^{2-} [129, 160, 161]. The initial guess for the Pt adsorption site was selected such that the maximum interaction with the neighboring oxygen atoms is present due to the oxophilic tendency of the Pt atom [128]. As shown in Figure 49, the strongest adsorption site for the Pt single atom on the $\theta[H_2O]$=0 surface is the O^{2-} site with bond length of 2.0 Å (Table 22). Influence of the 1^{st} shell relaxation around the central O^{2-} site (denoted as O_s) led to the

Table 21.: Pt binding energies (eV) calculated for the water-free ($\theta[H_2O]$=0) and the fully hydroxylated ($\theta[Al(OH)_3]$=1) surfaces. All values are calculated using the def2-TZVPP basis set and are BSSE corrected.

Model	Relaxed shell	Pt binding energy (eV)		
		PBE	B3LYP	PBE0
Pt/$\theta[H_2O]$=0	1^{st}	-2.85	-2.56	-2.51
	2^{nd}	-2.88	-2.68	-2.62
Pt/$\theta[Al(OH)_3]$=1	1^{st}	-2.14	-1.83	-1.73
	2^{nd}	-2.1	-1.83	-1.74

interaction of the Pt atom with the two neighboring Al^{3+} sites with a binding energy of -2.9 eV (PBE) and ≈-2.5 eV (B3LYP, PBE0), respectively (Table 21). While relaxation until the 2^{nd} shell reduced the interaction of the Pt atom with only central O^{2-} and Al_{s1} sites and the binding energy further increased by ≈0.12 eV (Table 21). This is due to the release of strong geometric constraints on the relaxation going from 1^{st} to the 2^{nd} shell, further relaxing the Al_{s2} site towards the bulk.

Table 22.: Change in structural parameters after Pt single atom adsorption on the water-free ($\theta[H_2O]$=0) and the fully hydroxylated ($\theta[Al(OH)_3]$=1) surfaces are provided. Bond-length between Pt and O_s (Å) (denoted as d(Pt-O_s), displacement of the O_s site (Å) (denoted as Δr (O_s)), and displacement of Al_{s1} site (Å) (denoted as Δr (Al_{s1})). A positive sign denotes upward displacement and a negative sign denotes downward displacement. For nomenclature refer to Figures 49 and 50. All geometries are optimized using the def2-TZVPP basis set.

Model	d(Pt-O_s)			Δr (O_s)			Δr (Al_{s1})		
	PBE	B3LYP	PBE0	PBE	B3LYP	PBE0	PBE	B3LYP	PBE0
$\theta[H_2O]$=0	2.01	2.03	2.00	-0.07	-0.07	-0.09	0.33	0.29	0.27
$\theta[Al(OH)_3]$=1	2	2.02	1.99	-0.03	0.01	-0.01	-0.02	-0.03	-0.02

The changes in the structural parameters on the surface after Pt single atom adsorption is given in Table 22. According to the results, the Pt adsorption led to a weakening of the O_s-Al_{s1} bond due to the Pt interaction with the O_s site on the $\theta[H_2O]$=0 surface. It is evident from the elongation of the bond from 1.69 to 1.82 Å. The interacting O_s ion is also seen to have a small displacement in the downward direction by ≈0.1 Å while the adjacent Al_{s1} cation moves above the O_s ion with upward displacement of ≈0.3 Å. The bond length present between the Pt atom and the Al_{s1} site is around 2.4 Å. The Al_{s1} atom tends to strengthen its bonding with the O_s site through the bond-order conservation mechanism [114]. All these displacements together show that the surface adapts to optimize the Pt-surface bonding by reorganizing the Al-O bond strengths. Thus, the strong Pt adsorption energy on the $\theta[H_2O]$=0 surface is mainly due to the contribution

of the surface relaxation [162]. Additionally, the population analysis on the Pt/Al_2O_3 shows that the Pt atom has a positive charge (0.11|e|) indicating that it is oxidized while the surface is reduced as a result of the Pt interaction with the Al_2O_3 surface (Table 23). The coupling between the Pt and the O_s has a d character. The O-p orbital is hybridized with the Pt-d orbital to form the chemical bond as can be seen in the population analysis given in Table 23. Charge transfer from the Pt-d orbital to the Al-p orbital is observed. This interaction leads to the upward displacement of the Al^{3+} cations leading to a large distance between the layers leading to its well separation from the layers beneath. This is also seen in the structural analysis. This phenomenon can strongly affect the nearby adsorption sites due to the long-range Coulomb interaction. Thus, these structural and electronic analyses show that on a water-free surface, there is a strong correlation between the adsorption energy of the Pt atom, surface relaxation, local deformations as well as the interfacial Pt-support interaction. Such adsorbate-induced surface relaxation and the local interaction of the metal atoms (for example Pt, Pd, Cu) with both O^{2-} and Al^{3+} sites was also observed on other aluminum oxide polymorphs such as γ-Al_2O_3 and θ- Al_2O_3 surfaces theoretically and experimentally [162–164].

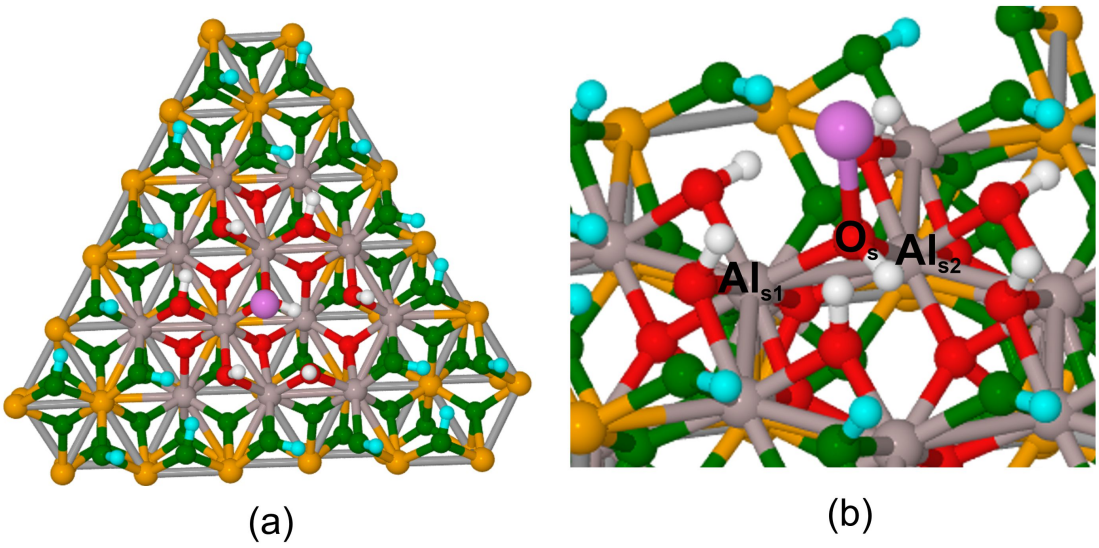

Figure 50.: Schematic of the single Pt atom binding configuration on the fully hydroxylated surface (θ[$Al(OH)_3$]=1) with relaxation until 2^{nd} shell (a (top view), b (side view)). All geometries are computed using the def2-TZVPP basis set. (Color scheme of atoms: grey-unfixed Al, yellow-fixed Al, red-unfixed oxygen, green-fixed oxygen, violet-platinum atom, white-unfixed hydrogen, cyan-fixed hydrogen).

Furthermore, the effect of surface hydroxylation on the Pt adsorption was studied. The Pt adsorption configuration on the fully hydroxylated (θ[$Al(OH)_3$]=1) surface is shown in Figure 50. The results show that Pt adsorbs on the surface O^{2-} site of the hydroxyl group with an adsorption energy of ≈-2 eV (Table 21) and at a distance of 2 Å (Table 22). The adsorption energy on θ[$Al(OH)_3$]=1 is lower compared to the θ[H_2O]=0 surface

due to the absence of an extra interaction with the Al^{3+} cation on the support. These cationic sites are fully saturated with the hydroxyl group terminations and therefore not available for additional interaction with the Pt atom. However, observations reported for Cu/γ-Al_2O_3 system [164] show an opposite trend. Cu is seen to bind with a hydroxyl group and the neighboring O^{2-} ion, leading to higher adsorption energy and stronger surface deformation on a hydroxylated surface than on a water-free surface, which is not seen in the present study. The effect of sequential shell relaxation on the Pt binding energy is also not prominent (Table 21). The effect of full saturation is seen in the analysis of the layer relaxation. The displacement of the O_s and Al_{s1} sites is negligible compared to the $\theta[H_2O]$=0 surface (Table 22) showing that surface hydroxyl groups stabilize significantly the Al_2O_3 surface. Furthermore, the population analysis of the Pt/$\theta[Al(OH)_3]$=1 system shows that the Pt atom is almost charge neutral (-0.02 $|e|$) showing weak interaction with the surface.

Table 23.: Atomic charges (in $|e|$) and orbital population computed for a Pt atom, the water-free ($\theta[H_2O]$=0) and fully hydroxylated ($\theta[Al(OH)_3]$=1) surfaces and the adsorbed Pt on both the surfaces. Given values are for the geometry optimized using B3LYP and def2-TZVPP basis set.

Model	Atom	Charge	Orbital population		
			n(s)	n(p)	n(d)
	Pt	0	2	6	10
$\theta[H_2O]$=0	Al_{s1}	2.6	4.228	6.17	0.0016
	O_s	-1.7	3.833	5.867	0.00
Pt/$\theta[H_2O]$=0	Pt	0.1107	2.18	5.9952	9.714
	Al_{s1}	2.54	4.238	6.217	0.002
	O_s	-1.679	3.832	5.847	0.00
$\theta[Al(OH)_3]$=1	Al_{s1}	2.441	4.216	6.339	0.00369
	O_s	-1.5	3.776	5.724	0.00
	H	0.588	0.412	0.0	0.0
Pt/$\theta[Al(OH)_3]$=1	Pt	-0.023	2.211	5.998	9.814
	Al_{s1}	2.43	4.212	6.354	0.004
	H	0.637	0.363	0.0	0.0
	O_s	-1.488	3.779	5.709	0.00

Both, the water-free ($\theta[H_2O]$=0) and the fully hydroxylated ($\theta[Al(OH)_3]$=1) surfaces, show that Pt strongly interacts with the bare surface via charge transfer, while Pt interacts weakly with the fully hydroxylated surface with minimal interaction with the surface sites. Thus, the probability of Pt atoms to aggregate in nanoclusters can be higher on the hydroxylated surface compared to the bare surface, following the results obtained for Pd/γ-Al_2O_3 system [162].

4.3.2.2. CO interaction on Pt/α-Al_2O_3 surface

In order to determine the chemical states of Pt adsorbed on the Al_2O_3 surface, the CO molecule is used as a probe molecule in the experiment as well as in theoretical models due to the strong bonding present between Pt and the CO molecule. The interaction of CO with Pt/$\theta[H_2O]$=0 and Pt/$\theta[Al(OH)_3]$=1 models is shown in Figure 51 and 52, respectively. The CO binding energies and the bond length on both surfaces are given in Table 24. The atomic charges and the orbital occupations are given in Table 26. The pre-adsorbed single Pt atom acts as an anchor for the adsorption of the CO molecule with a C-down configuration with slightly tilted orientation. The effect of sequential shell relaxation on the CO BE is negligible (≈0.06 eV) relaxing from 1^{st} until the 2^{nd} shell. The CO interaction with the Pt single atom on the $\theta[H_2O]$=0 surface has a binding energy of -3.9, -3.6, and -3.7 eV calculated using PBE, B3LYP, and PBE0 DFT functionals, respectively. The CO bond length is also lengthened upon adsorption on the Pt/$\theta[H_2O]$=0 surface in comparison to the $CO_{(g)}$. Additionally, a direct interaction of Pt with the surface Al_{s1} site is also seen which can lead to the surface stabilization. This is also evident from the shrunk bond length between Al_{s1}-Pt from 2.45 Å to 2.37 Å. The CO interaction with the Pt/$\theta[Al(OH)_3]$=1 surface also shows a similar tilt orientation (Figure 52). The computed CO binding energy on the hydroxyl-terminated Al_2O_3 surface is ≈-4 eV (Table 24). The influence of sequential shell relaxation is negligible (≈0.1 eV) relaxing from 1^{st} until the 2^{nd} shell. The CO bond length is also lengthened to ≈1.17 Å compared to the $CO_{(g)}$.

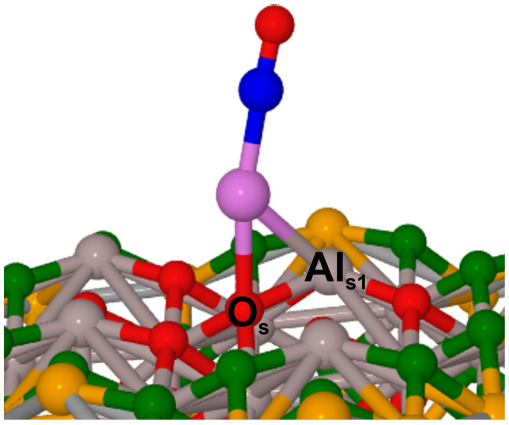

Figure 51.: Schematic of CO binding mode on Pt/$\theta[H_2O]$=0. (Color scheme of atoms: grey-unfixed Al, yellow-fixed Al, red-unfixed oxygen, green-fixed oxygen, violet-platinum atom, blue-carbon).

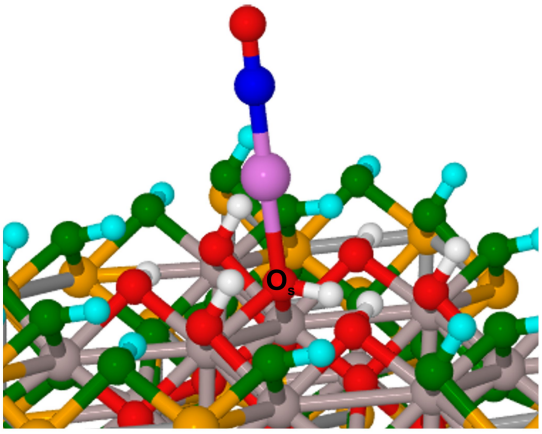

Figure 52.: Schematic of the CO binding mode on Pt/θ[$Al(OH)_3$]=1 surface. (Color scheme of atoms: grey-unfixed Al, yellow-fixed Al, red-unfixed oxygen, green-fixed oxygen, white-unfixed hydrogen, cyan-fixed hydrogen, violet-platinum atom, blue-carbon).

Table 24.: CO binding energies (eV) and bond lengths (Å) calculated for Pt/θ[H_2O]=0 and Pt/θ[$Al(OH)_3$]=1 surfaces using the def2-TZVPP basis set.

Model	Relaxed shell	CO binding energy (eV)			CO bond length (Å)		
		PBE	B3LYP	PBE0	PBE	B3LYP	PBE0
Pt/θ[H_2O]=0	1^{st}	-4.02	-3.62	-3.79	1.16	1.15	1.14
	2^{nd}	-3.93	-3.56	-3.73	1.16	1.14	1.14
Pt/θ[$Al(OH)_3$]=1	1^{st}	-4.7	-4.28	-4.49	1.17	1.16	1.16
	2^{nd}	-4.57	-4.14	-4.36	1.17	1.16	1.16
$CO_{(g)}$	-	-	-	-	1.14	1.13	1.12

The analysis of atomic charges and the orbital occupations (Table 26) for CO adsorption on Pt/θ[H_2O]=0 surface shows that the positive charge on the Pt further increases from +0.11 to +0.267 $|e|$ upon CO adsorption. The carbon of the CO molecule (denoted as C_{CO}) becomes more positive (+0.858 $|e|$) compared to the $CO_{(g)}$ (+0.486 $|e|$) showing strong σ donation from CO towards Pt. This is further confirmed via orbital population where loss of electron density is seen in the *2s* and *2p* orbitals of the carbon. The oxygen of the CO molecule (O_{CO}) becomes more negative (-0.946 $|e|$) showing the gain of electron density in its *2p* orbital and the electron density of Pt-*5d* orbitals is seen to be decreased indicating a π-backdonation from Pt into the antibonding π orbital of CO. The increase in the electron density of the CO $2\pi^*$ orbital thus leads to the C-O bond weakening [2, 5, 129]. Similar results are also seen in the CO adsorption on Pt/θ[$Al(OH)_3$]=1 surface. In the Table, it can be seen that the *2p* orbital of O_{CO} has higher electron density compared to the Pt/θ[H_2O]=0 surface showing that π-backdonation from Pt to CO is stronger on Pt/θ[$Al(OH)_3$]=1 surface. These results show a strong CO-Pt bond formation due to the combination of σ-donation from CO to Pt and π-backdonation from Pt to CO. Further

lengthening of the bond length between Pt-O_s from 2 Å to 2.11 Å is also observed. These observations are in agreement with the Blyholder model [165]. The strong CO binding energy and the presence of a hydroxyl group in the vicinity can further lead to the formation of carbonyl and carbonate species on the Pt site [166]. This scenario has to be further studied. The trends reported here obey quite well with the theoretical study carried out on defect-free Al_2O_3 surface using a plane-wave DFT and PBE functional [129].

Table 25.: Harmonic ($\tilde{\nu}$(CO) (cm^{-1})) and scaled harmonic (ν(CO) (cm^{-1})) CO vibrational frequencies for CO adsorbed on Pt/$\theta[H_2O]$=0 and Pt/$\theta[Al(OH)_3]$=1 surfaces computed using the def2-TZVPP basis set.

Model	$\tilde{\nu}$(CO) (cm^{-1})			ν(CO) (cm^{-1})			Expt.
	PBE	B3LYP	PBE0	PBE	B3LYP	PBE0	(cm^{-1})
Pt/$\theta[H_2O]$=0	2054	2125	2165	2068	2059	2072	2080 [167]
Pt/$\theta[Al(OH)_3]$=1	1980	2037	2078	1994	1974	1990	-

Due to the negligible effect of the sequential shell relaxation on the CO BE and other structural properties, CO vibrational frequencies were computed for the Pt/$\theta[H_2O]$=0 system relaxed until the 2^{nd} shell and Pt/$\theta[Al(OH)_3]$=1 relaxed until the 1^{st} shell. The scaled harmonic CO vibrational frequencies on both these systems are given in Table 25. The general trend in the computed CO vibrational frequency shifts $\Delta(\nu(CO))$ is that it is red-shifted on Pt/$\theta[H_2O]$=0 surface in the range of 75-84 cm^{-1} with respect to $\nu(CO)_{(g)}$ ($\nu(CO)_{(g)}$ = 2143 cm^{-1}) and depends on the employed DFT functionals. The CO vibrational frequency shift $\Delta(\nu(CO))$ on Pt/$\theta[Al(OH)_3]$=1 surface is seen to be further red-shifted in the range of 153-169 cm^{-1} with respect to $CO_{(g)}$ depending on the DFT functionals used. The CO vibrational frequency shift in the mechanism of CO bonding to the transition metal surface is explained by the Byholder model [165] using molecular orbitals. As the vibrational frequency of the C-O stretching frequency is proportional to the strength of the C-O bond, due to the C-O bond weakening on the Pt/$\theta[H_2O]$=0 and Pt/$\theta[Al(OH)_3]$=1 surfaces, the vibrational frequency shifts towards the lower wavenumbers compared to the $\nu(CO)_{(g)}$. Since only one adsorbed CO molecule is considered in the embedded cluster model, it mimics the low CO coverage scenario with high Pt dispersion, and thus are comparable with the experimental data considering the same.

The findings of Anderson *et. al* [167] can be compared with the presented EQC results on CO interaction with the Pt/$\theta[H_2O]$=0 surface. The experiment focused on the CO adsorption on Pt-Rh/Al_2O_3 surface using infrared spectroscopy.

Table 26.: Atomic charges (in $|e|$) and orbital population computed for CO, Pt/θ[H_2O]=0 and Pt/θ[$Al(OH)_3$]=1 systems using the B3LYP functional and the def2-TZVPP basis set. For nomenclature refer to Figures 51 and 52.

Model	Atom	Charge	Orbital population	
			Core	Valence
Pt		0	8	6s=0.00, $5d_{z^2}$=2.00, $5d_{xz}$=2.00, $5d_{yz}$=2.00, $5d_{xy}$=2.00, $5d_{x^2-y^2}$=2.00
$CO_{(g)}$	C_{CO}	0.486	2	2s=1.643, $2p_x$=0.46, $2p_y$=0.46, $2p_z$=0.90
	O_{CO}	-0.486	2	2s=1.724, $2p_x$=1.53, $2p_y$=1.53, $2p_z$=1.665
Pt/θ[H_2O]=0	Pt	0.111	8	6s=0.189, $5d_{z^2}$=1.744, $5d_{xz}$=2.0, $5d_{yz}$=1.99, $5d_{xy}$=1.99, $5d_{x^2-y^2}$=1.993
	Al_{s1}	2.543	10	0.448
	O_s	-1.679	2	7.677
CO/Pt/θ[H_2O]=0	O_{CO}	-0.946	2	2s=1.65, $2p_x$=1.785, $2p_y$=1.796, $2p_z$=1.718
	C_{CO}	0.858	2	2s=1.166, $2p_x$=0.608, $2p_y$=0.662 $2p_z$=0.695
	Pt	0.267	8.0	6s=0.867, $5d_{z^2}$=1.669, $5d_{xz}$=1.635, $5d_{yz}$=1.615, $5d_{xy}$=1.988, $5d_{x^2-y^2}$=1.986
	Al_{s1}	2.483	10	0.494
	O_s	-1.717	2	7.714
Pt/θ[$Al(OH)_3$]=1	Pt	-0.023	8	6s=0.213, $5d_{z^2}$=1.828, $5d_{xz}$=1.993, $5d_{yz}$=1.998, $5d_{xy}$=1.996, $5d_{x^2-y^2}$=1.998
	Al_{s1}	2.43	10	0.554
	H	0.637	0	0.36
	O_s	-1.488	2	7.485
CO/Pt/θ[$Al(OH)_3$]=1	O_{CO}	-0.984	2	2s=1.655, $2p_x$=1.796, $2p_y$=1.797, $2p_z$=1.735
	C_{CO}	0.931	2	2s=1.144, $2p_x$=0.616, $2p_y$=0.616 $2p_z$=0.680
	Pt	0.032	8	6s=1.017, $5d_{z^2}$=1.775, $5d_{xz}$=1.607 $5d_{yz}$=1.605, $5d_{xy}$=1.992, $5d_{x^2-y^2}$=1.993
	Al_{s1}	2.449	10	0.532
	H	0.612	0	0.386
	O_s	-1.501	2	7.499

The IR results obtained on 1.0 wt % Pt/Al_2O_3 surface exposed to a CO/He mixture at 423 K consisted of an IR band at 2080 cm^{-1}. This IR band was ascribed to the linearly absorbed CO on the Pt atom along with strong interaction with the Al_2O_3 surface. The IR band was seen to shift towards lower wavenumbers with an increase in the experimental temperature. Similar observations were reported in another experimental study [163] where the IR band for linearly adsorbed CO species on ionic $Pt^{\delta+}$ sites was present in the range of 2087-2096 cm^{-1}. The main reason for the red-shift was ascribed to the deficiency in the electron density of the Pt. The same trend was also reported for CO adsorbed on a Pt_1/FeO_x single atom catalyst [168]. Thus, the trends observed in the structural analysis and the CO vibrational frequency ν(CO) on Pt/$\theta[H_2O]$=0 model are in good agreement with the previously reported experimental observations. Due to the lack of experimental results on the fully hydroxylated Al_2O_3 surface with adsorbed single Pt atoms and corresponding CO adsorption, only an estimation can be made on the EQC result. As seen in the case of Pt/$\theta[Al(OH)_3]$=1, a strong back donating interaction is observed where the excess electronic charge on Pt is transferred to the CO molecule which can be the reason for the larger shift in (ν(CO)) compared to $\nu(CO)_{(g)}$.

4.3.2.3. Influence of the exchange-correlation functional

Finally, the influence of different DFT exchange-correlation functionals for both the optimized surface models of CO/Pt/$\theta[H_2O]$=0 and CO/Pt/$\theta[Al(OH)_3]$=1 was examined by keeping a constant def2-TZVPP basis set for the relaxed atoms in all calculations. Starting with the different adsorption energies computed for Pt single atom adsorption on Al_2O_3 surface and CO adsorption on Pt/Al_2O_3 systems. On all levels of theory, the Pt bonding to O^{2-} sites is seen to be a stable configuration. The general trend in the adsorption energies is that the binding energy calculated using the PBE functional is higher by ≈0.3 eV for Pt/Al_2O_3 and ≈0.4 eV for $CO/Pt/Al_2O_3$ compared to the hybrid functionals. It is well known that GGA functionals tend to overestimate the bond strengths at the metal-oxide interface and the result is in line with the previous theoretical studies [146, 169]. Hybrid- functionals have shown to be more reliable in such systems in describing the energetics accurately in comparison to experiment due to the additional fraction of HF exchange which can reduce the self-interaction error and the over-delocalization in DFT [170]. However, the structural parameters given in Table 22 reveal that the influence of the different DFT functionals on the structure is negligible. Nevertheless, all methods predict the same trend in the stability for the different active sites on both the models. Next, the influence of the PBE, B3LYP and PBE0 functionals on the CO vibrational frequency was checked. The harmonic and scaled harmonic frequencies computed for CO adsorbed on Pt/$\theta[H_2O]$=0 and Pt/$\theta[Al(OH)_3]$=1 are given in Table 25. The harmonic frequencies are scaled using the scaling factors 1.005589, 0.967442, 0.956129 for PBE, B3LYP and PBE0 respectively. The shift of the harmonic frequencies in comparison to the experimental CO frequency (2080 cm^{-1}) is 26 (PBE), -45 (B3LYP), -85 (PBE0) cm^{-1} respectively. After scaling the harmonic frequencies, the deviation reduces further to 12, 21 and 8 cm^{-1} for PBE, B3LYP and PBE0 functionals, respectively. This result shows

that the scaling factor is needed for the vibrational frequencies computed using hybrid functionals in order to have a better agreement with the experimental value. Due to the unavailability of the experimental value for the Pt/$\theta[Al(OH)_3]$=1 system, the deviation of the harmonic frequencies cannot be validated.

4.3.3. Conclusion

In the present work, a systematic theoretical study was carried out using an embedded cluster model along with DFT to examine the effects of two different surfaces, water-free ($\theta[H_2O]$=0) and fully hydroxylated ($\theta[Al(OH)_3]$=1), on the adsorption of a single Pt atom and its corresponding interaction with the adsorbed CO molecule. The results showed that the Pt atom prefers to bind on top of the basic O^{2-} site on both of the surfaces. It additionally interacted with the surface Al^{3+} site on the water-free surface, leading to high surface deformation and a high Pt adsorption energy. Metal-to-surface charge transfer was also observed at the interface. The adsorption energy on a fully hydroxylated surface was reduced by ≈0.5 eV compared to the water-free surface due to the presence of surface hydroxyl groups, showing that hydroxyl groups stabilize the surface significantly leading to a low surface relaxation. The negligible surface-to-metal charge transfer was seen at the interface.

Further, CO interaction with Pt/$\theta[H_2O]$=0 and Pt/$\theta[Al(OH)_3]$=1 was investigated. The Pt atom acted as an anchor for the CO molecule adsorption in a linear configuration. Higher CO binding energy was seen on Pt/$\theta[Al(OH)_3]$=1 compared to Pt/$\theta[H_2O]$=0 due to the strong interaction between the CO molecule and Pt atom via charge transfer from CO to Pt via σ-donation and Pt towards the molecule via π-backdonation. The CO vibrational frequencies were seen to be red-shifted on both surfaces compared to the frequency of the CO molecule in the gas phase. Finally, the embedded cluster model facilitated the examination of the influence of different DFT functionals on the characteristic properties of the CO adsorbed on Pt/Al_2O_3. The quantitative trend resulting from the computations using all the three functionals, PBE, B3LYP, PBE0 showed that the adsorption energy using the PBE functional was overestimated (≈0.3 eV) compared to the hybrid functionals. Employing scaling factor improved the CO frequency shift values computed using GGA and hybrid functionals.

5. Summary and conclusion

Heterogeneous catalysts containing metal-oxide-supported transition metal nanoclusters have proved to be quite efficient in many chemical reactions relevant to industry. The catalysts high activity is influenced by many factors such as 1) reconstructions in the structure of the nanoclusters supported on the surface, 2) the surface deformation and relaxation of the metal-oxide support, and 3) mutual interactions at the metal-support interface. Moreover, it has been a challenge to understand the key role of each of these factors in the improvement of the catalytic activity. Thus, with the motivation to understand the underlying fundamental aspects responsible for these complex interactions, a comprehensive study was carried out by means of different quantum chemical tools.

The influence of the hydrogen atoms on the structure evolution of small Pt nanoclusters $Pt_nD_{2n}^-$ with n=6-13 was studied. Due to the strong affinity of Pt clusters towards hydrogen adsorption this is important for the application in various catalytic reactions. However, to determine the cluster structure in the experiment is non-trivial. Therefore, in combination with trapped ion electron diffraction spectroscopy (TIED), density functional theory was employed for determining the best-fitting cluster configurations for each cluster size ensemble. In collaboration with PD Detlef Schooss, structures were assigned to each cluster size ensemble by comparing the scattering functions for the simulated clusters with those from the experiment. The predicted Pt-core structure of low energy clusters optimized at TPSS/dhf-TZVP-2c level of theory for each cluster size were in good agreement with the experimental TIED data, except for the $Pt_7D_{14}^-$, where higher lying cluster showed a better agreement with the experiment. Upon having a closer examination of the bare Pt_n^- clusters with the deuterated $Pt_nD_{2n}^-$ showed that the deuterium atoms do influence the Pt core structures. The small bare Pt_n^- cluster show amorphous-like structures which upon interaction with deuterium atoms led to the development of more spherical geometries with higher symmetry. The symmetry of the clusters evolves from the distorted structure of $Pt_6D_{12}^-$ to the cuboctahedral structure at $Pt_{13}D_{26}^-$. This evolution of higher symmetry clusters shows that deuterium atoms prefer to bind in bridge-positions which stabilize the cluster structure. However, in the quest to find the low and best-fitting cluster isomers, many isoenergetic as well as higher-lying isomers with different deuterium configurations at local minima were observed to contribute to the TIED data along with the lowest energy isomer. These contributions cannot be ruled out experimentally.

Among the $Pt_nD_{2n}^-$ clusters, the $Pt_{12}D_{24}^-$ cluster exhibited a unique cuboctahedral cage structure. A thorough analysis was carried out to understand the fundamental reasons

behind the stability of this particular motif. Among the $Pt_{12}D_{24}^-$ ensemble, the cuboctahedral cage structure isomer **1** was observed to be the lowest energy isomer and best-fitting isomer to the TIED data. Irrespective of the low Pt coordination number in the cage structure compared to the other incomplete cuboctahedron isomer **2** in the ensemble, it proves to be a quite stable geometry. The structural analysis of both the isomers, **1** and **2** shows that the number and type of Pt-D bonds are the two decisive factors prominent in the isomers. Isomer **1** shows that bridged-bound deuterium atoms stabilize the structure significantly through strong interaction with the neighboring Pt atoms forming a multi-center bonds. This led to a significant charge transfer and to the stabilization of the electronic structure. In contrast, the deuterium shell of isomer **2** consists of a mixture of on-top and bridge bound deuterium atoms making the cluster quite dynamic. Due to the presence of low activation barriers of different deuterium configuration, the isomer transformation from isomer **2** to **1** can be modeled and observed. Also, the presence of a free *fcc* Pt atom at the core of isomer **2** can make the structure more reactive and help transform into the more stable isomer **1**.

Next, the Al-terminated α-Al_2O_3 (0001) metal-oxide surface was analyzed using an embedded cluster model along with density functional theory and Møller Plesset perturbation theory (MP2). At first, the CO interaction with the Al_2O_3 surface was investigated at low CO coverage. Three differently terminated surfaces were considered, the water-free ($\theta[H_2O]=0$), the fully hydroxylated ($\theta[Al(OH)_3]=1$) and the H_2O dissociated ($\theta[H_2O]=1$) surface. Additionally, the θ[[H_2O=0]+OH+H] surface with dissociated H_2O molecule in 1-2 configuration was analyzed exhibiting low hydroxyl coverage. According to the energetics, a CO molecule strongly binds to the $\theta[H_2O]=0$ surface with an adsorption energy in the range -0.38 to -0.71 eV and a linear CO orientation with C-down configuration. In contrast, weak CO interaction was seen on the hydroxylated surfaces, $\theta[Al(OH)_3]=1$, $\theta[H_2O]=1$ and θ[[H_2O=0]+OH+H] with an adsorption energy in the range of -0.23 to -0.29 eV. The analysis of the CO binding mode shows that on the $\theta[H_2O]=0$ surface, the strong bonding at the interface results from a significant charge transfer from CO towards the support. On the hydroxylated surfaces, the CO molecule is mainly stabilized by the weak electrostatic interactions with the underlying surface hydroxyl groups via OC-HO hydrogen bonding. When comparing the DFT results with MP2 results, it can be inferred that MP2 cannot accurately describe the weak interactions present on the hydroxylated surfaces. The CO vibrational frequencies are seen to be significantly blue-shifted for the CO interaction with the cationic site and low CO coverage. These results agree well with the polarization-resolved infrared reflection absorption spectroscopy results (IRRAS).

A similar analysis for CO_2 adsorption on an Al-terminated α-Al_2O_3 (0001) metal-oxide surface was carried out. In this study again the water-free ($\theta[H_2O]=0$), fully hydroxylated ($\theta[Al(OH)_3]=1$) and (θ[[H_2O=0]+OH+H] (dissociated H_2O molecule in 1-2 configuration) surfaces were considered. On the $\theta[H_2O]=0$ surface, CO_2 is binding in two different configurations via a linear orientation and tridentate carbonate depending on the CO_2 binding site. Among these two configurations, the tridentate carbonate adsorption configuration has a higher adsorption energy (≈-1 eV) compared to the linear orientation

with an adsorption energy in the range of -0.3 to -0.6 eV. The tridentate carbonate configuration is mainly stabilized due to the additional interaction with the neighboring cationic sites facilitating a charge transfer and decrease in the O-C-O bond angle. Significant surface relaxation was observed. On the contrary, in the linear orientation, relatively low charge transfer at the interface leads to weaker interactions. The CO_2 interaction on the hydroxylated surfaces shows a weaker molecule surface interaction and the stabilization of the CO_2 is mainly through the electrostatic interactions with the surface hydroxyl groups. Furthermore, the CO_2 vibrational frequency was seen to be red-shifted for tridentate carbonate configuration while it blue-shifted when oriented in a linear configuration. The vibrational frequency shift on the fully hydroxylated surface was slightly blue-shifted and was in good agreement with the IRRAS experimental results.

Lastly. a systematic investigation was carried out for single Pt atom adsorption on the water-free ($\theta[H_2O]=0$) and the fully hydroxylated ($\theta[Al(OH)_3]=1$) surfaces. The structural analysis of the Pt/Al_2O_3 system shows that Pt prefers to bind on the anionic O^{2-} sites with an adsorption energy of -2.9- -2.6 eV on the $\theta[H_2O]=0$ surface and -2.14- -1.8 eV on the $\theta[Al(OH)_3]=1$ surface. Pt adsorption on the $\theta[H_2O]=0$ surface leads to a high surface deformation due to the additional interaction with the surface cationic site and metal-to-surface charge transfer. Negligible surface relaxation was seen on the $\theta[Al(OH)_3]=1$ surface indicating that hydroxyl groups stabilize the surface significantly. On the hydroxylated surface, negligible charge transfer takes place from the surface to the metal atom. Further CO interaction with the $Pt/\theta[H_2O]=0$ and $Pt/\theta[Al(OH)_3]=1$ surfaces show that CO prefers to bind on top of the Pt atom in linear configuration. Strong CO binding was seen on the $Pt/\theta[Al(OH)_3]=1$ surface due to the significant charge transfer via σ-donation from CO to Pt and π-backdonation from Pt to CO. The CO vibrational frequencies were seen to be red-shifted on both the surfaces compared to $CO_{(g)}$. The obtained results were in good agreement with the experimental results.

In summary, this thesis provided a fundamental understanding of different aspects related to the individual components of the heterogeneous catalytic system utilizing a quantum chemical approach. The effect of hydrogen interaction on the Pt cluster structure, the influence of surface hydroxylation on molecular adsorption, the interface interactions, and the anchoring sites have been successfully studied via density functional theory along with the embedded cluster model. This facilitated a systematic study and to predict the structural and electronic properties at different levels of theory.

A. Appendix

A.1. Appendix for Chapter 3.1

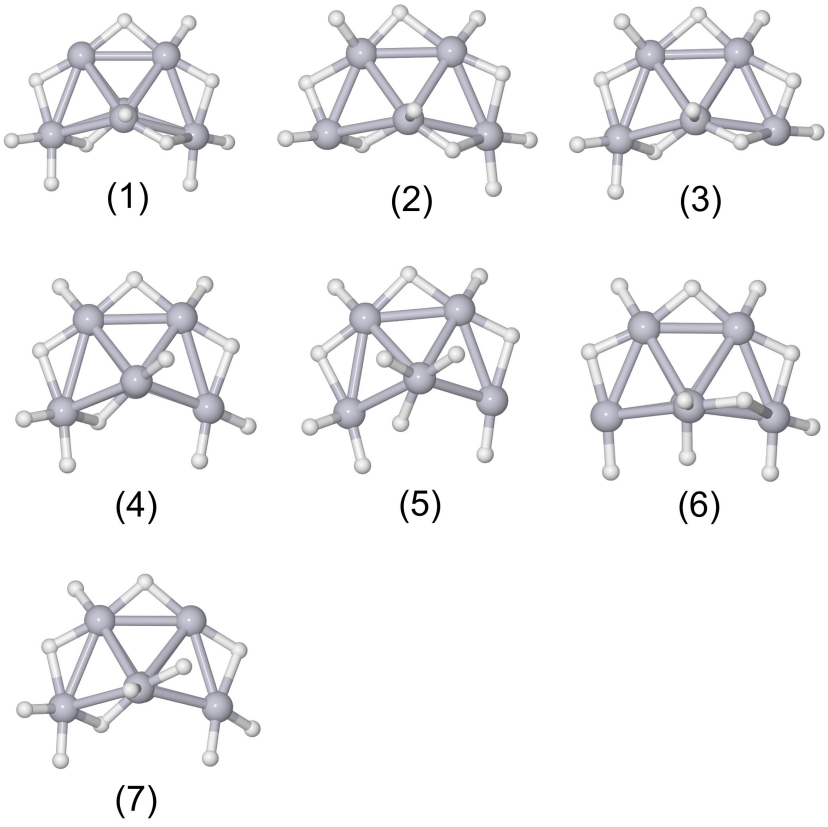

Figure A.1.1.: The higher lying $Pt_6D_{11}^-$ isomers optimized using TPSS/dhf-TZVP-2c.

Table A.1.1.: Relative energies (eV) and profile factors (R_w) of $Pt_6D_{11}^-$ isomers computed using TPSS/dhf-TZVP-2c.

Isomer	Relative energy (eV)	R_w (%)
1	0	5.25
2	0.08	4.73
3	0.14	4.54
4	0.17	2.69
5	0.17	4.68
6	0.23	3.74
7	0.46	4.63

Table A.1.2.: Relative energies (eV) and profile factors (R_w) of $Pt_6D_{12}^-$ isomers computed using TPSS/dhf-TZVP-2c.

Isomer	Relative energy (eV)	R_w (%)
1	0	4.11
2	0.17	4.263
3	0.36	10.53
4	0.37	6.79
5	0.38	5.03
6	0.39	4.79
7	0.41	2.61
8	0.42	6.23
9	0.84	10.98
10	1.27	6.53
11	1.33	17.37
12	1.46	5.49
13	1.52	23.75
14	1.55	10.27
15	1.59	11.41
16	1.59	11.41
17	1.99	10.84

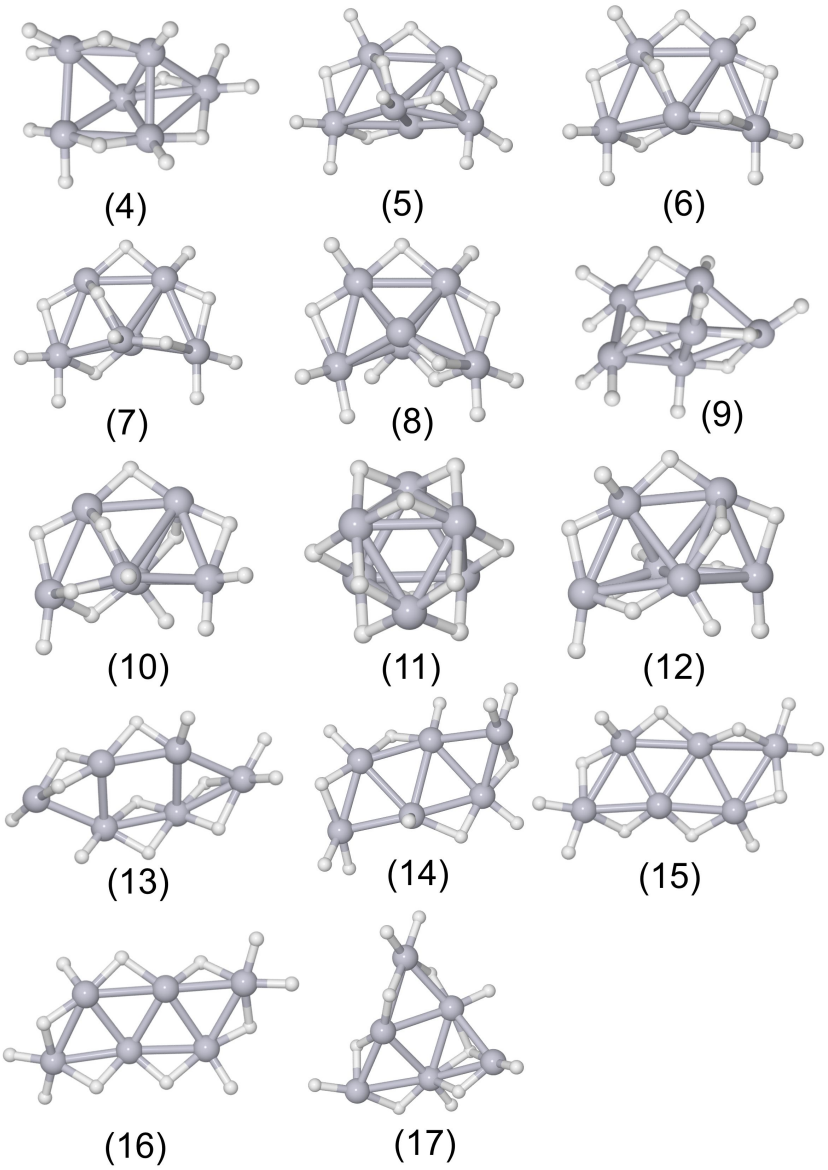

Figure A.1.2.: The higher lying $Pt_6D_{12}^-$ isomers optimized using TPSS/dhf-TZVP-2c.

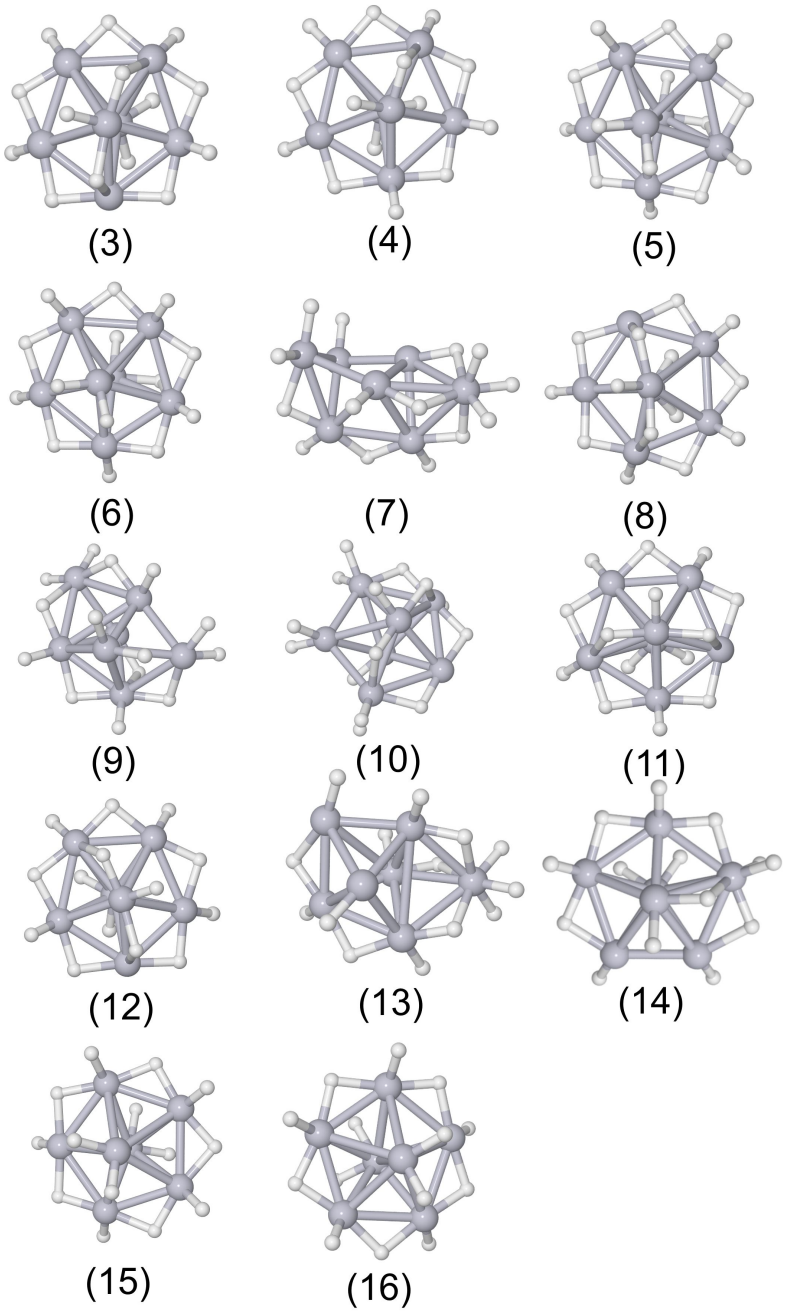

Figure A.1.3.: The higher lying $Pt_7D_{14}^-$ isomers optimized using TPSS/dhf-TZVP-2c.

Table A.1.3.: Relative energies (eV) and profile factors (R_w) of $Pt_7D_{14}^-$ isomers computed using TPSS/dhf-TZVP-2c.

Isomers	Relative energy (eV)	R_w (%)
1	0	10.78
2	0.04	2.98
3	0.28	6.46
4	0.32	2.98
5	0.32	2.97
6	0.32	2.97
7	0.49	18.92
8	0.51	5.82
9	0.51	21.43
10	0.54	3.4
11	0.56	6.64
12	0.56	6.64
13	0.58	23.75
14	0.73	3.1
15	1.06	4.06
16	1.06	4.04

Table A.1.4.: Relative energies (eV) and profile factors (R_w) of $Pt_8D_{16}^-$ isomers computed using TPSS/dhf-TZVP-2c.

Isomer	Relative energy (eV)	R_w (%)
1	0	13.24
2	0.19	5.46
3	0.3	6.44
4	0.16	12.98
5	0.29	14.88
6	0.42	8.18
7	0.44	9.6
8	0.45	31.83
9	0.76	7.71
10	1.08	8.19
11	1.08	12.32
12	1.31	7.89
13	1.36	12.51
14	1.45	9.8
15	1.58	14.06
16	1.79	18.52
17	1.93	16.89
18	2.02	6.54

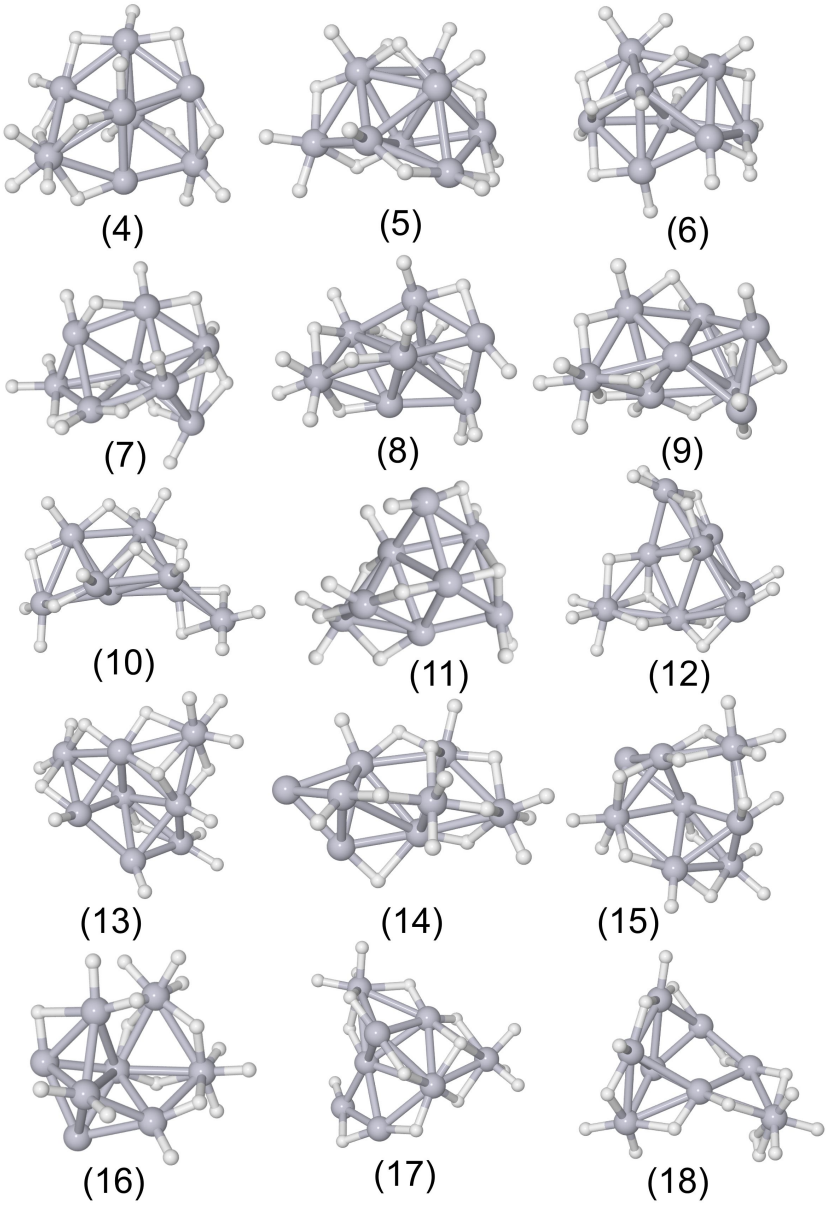

Figure A.1.4.: The higher lying $Pt_8D_{16}^-$ isomers optimized using TPSS/dhf-TZVP-2c.

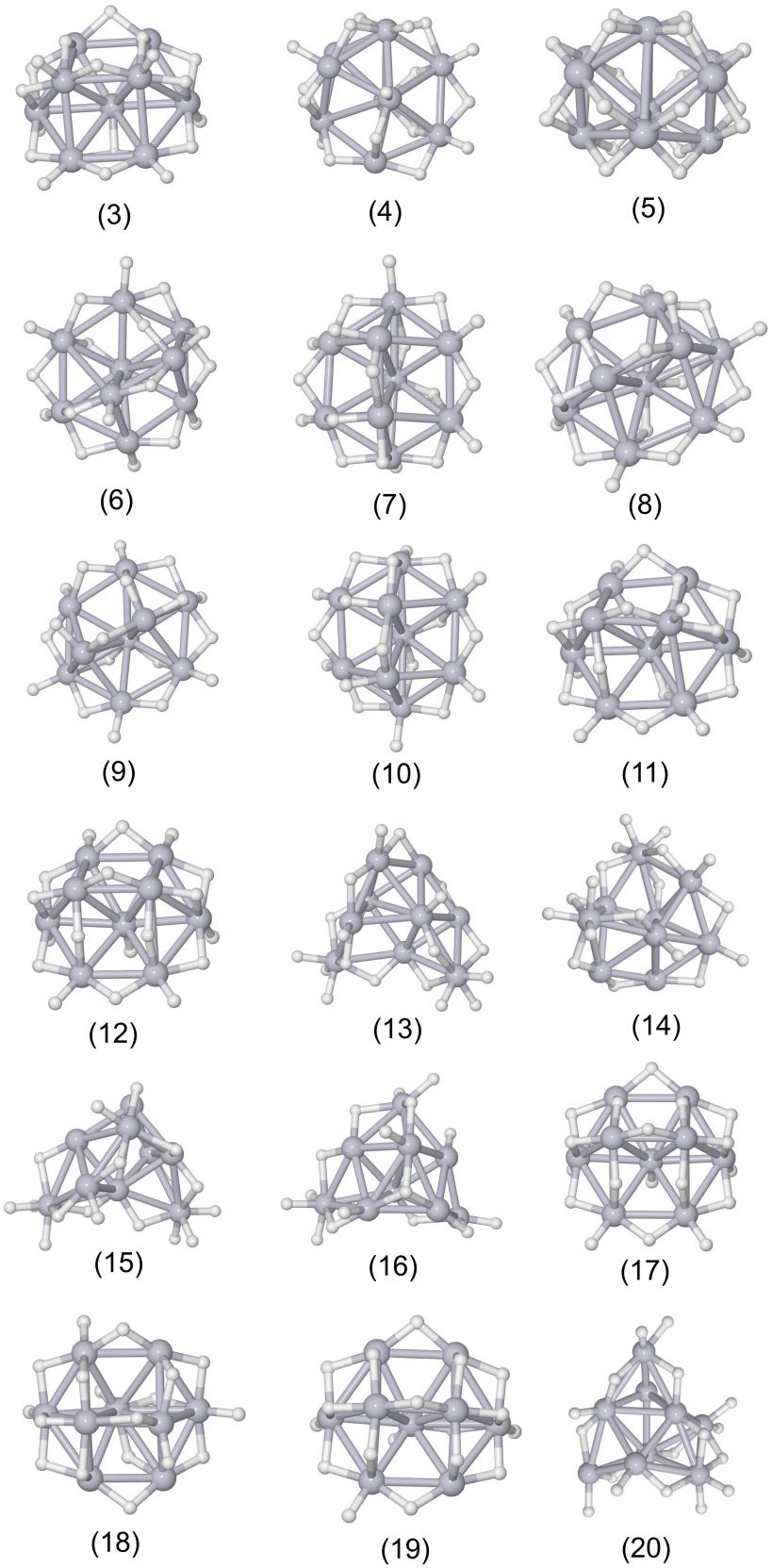

Figure A.1.5.: The higher lying $Pt_9D_{18}^-$ isomers optimized using TPSS/dhf-TZVP-2c.

Table A.1.5.: Relative energies (eV) and profile factors (R_w) of $Pt_9D_{18}^-$ isomers computed using TPSS/dhf-TZVP-2c.

Isomer	Relative energy (eV)	R_w (%)
1	0	4.5
2	0.41	3.1
3	0.11	5.02
4	0.25	5.67
5	0.31	22.65
6	0.32	4.15
7	0.34	3.79
8	0.34	3.81
9	0.34	3.8
10	0.34	3.8
11	0.45	4.49
12	0.58	5.17
13	0.66	6.34
14	0.66	6.33
15	0.75	14.57
16	1.08	7.42
17	1.16	10.33
18	1.32	6.35
19	1.56	4.12
20	1.67	10.8

Table A.1.6.: Relative energies (eV) and profile factors (R_w) of $Pt_{10}D_{20}^-$ isomers computed using TPSS/dhf-TZVP-2c.

Isomer	Relative energy (eV)	R_w (%)
1	0	3.52
2	1.12	25.58
3	0.15	3.59
4	0.15	3.59
5	0.55	4.63
6	0.91	3.54
7	1.15	23.28
8	1.17	11.24
9	1.21	12.8

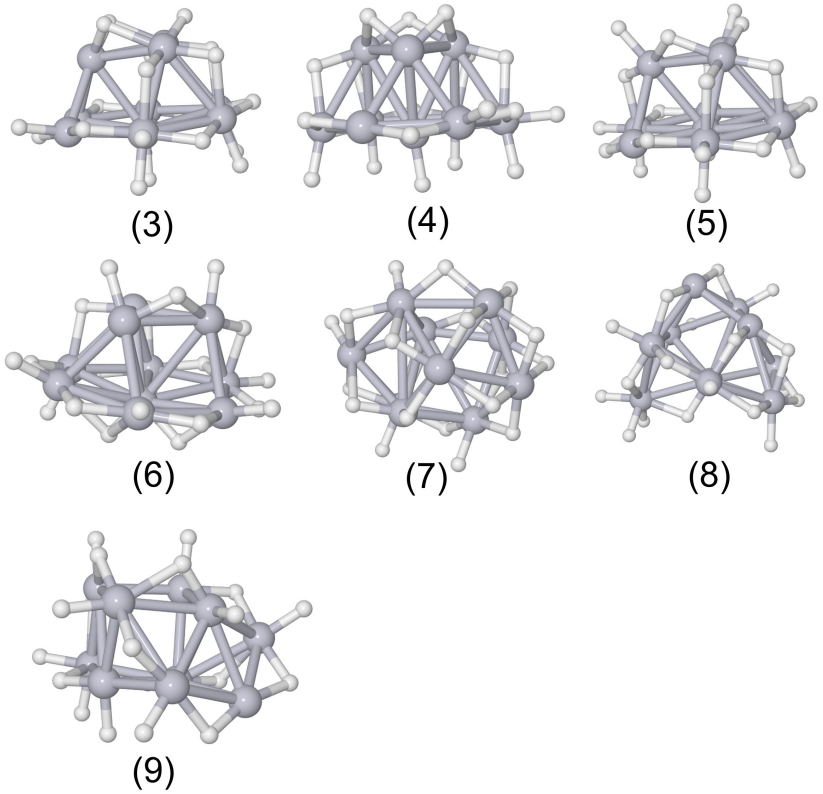

Figure A.1.6.: The higher lying $Pt_{10}D_{20}^-$ isomers optimized using TPSS/dhf-TZVP-2c.

Table A.1.7.: Relative energies (eV) and profile factors (R_w) of $Pt_{11}D_{22}^-$ isomers computed using TPSS/dhf-TZVP-2c.

Isomer	Relative energy (eV)	R_w (%)
1	0	18.53
2	0.03	7.24
3	0.29	7.91
4	0.37	6.96
5	0.43	9.2
6	0.7	8.69
7	0.78	7.82
8	0.83	11.09
9	0.91	9.74
10	0.93	5.68
11	1.18	10.95
12	1.36	15.53
13	2.51	9.79

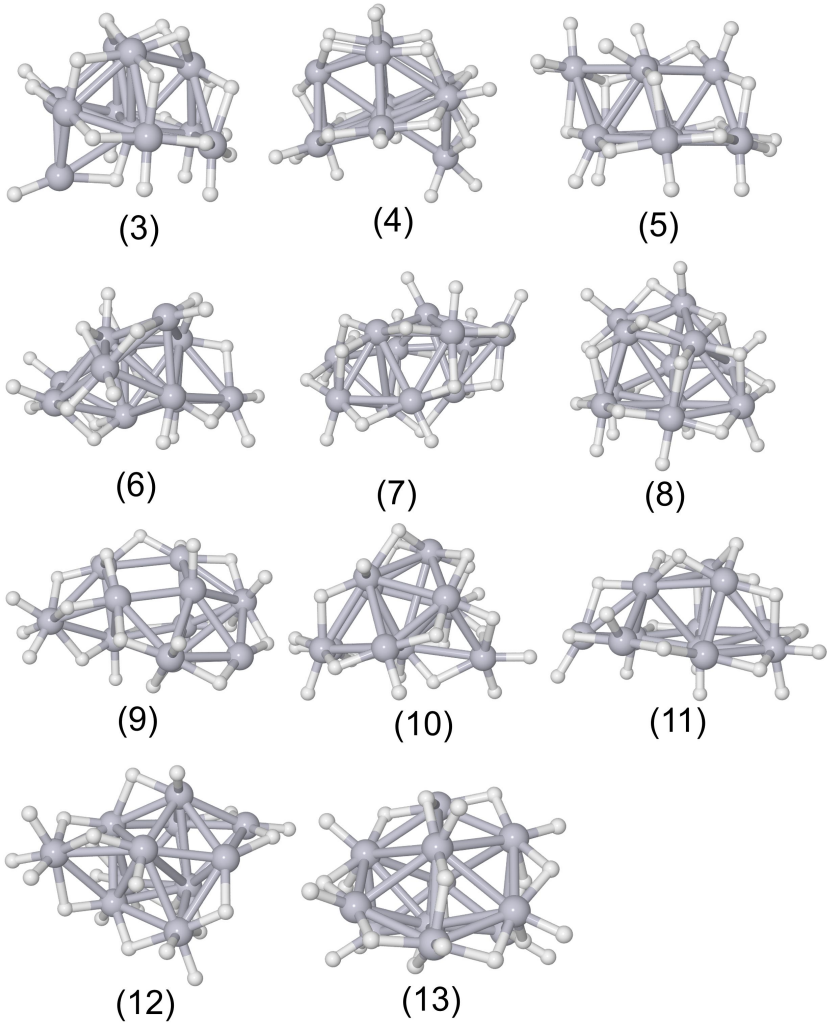

Figure A.1.7.: The higher lying $Pt_{11}D_{22}^-$ isomers optimized using TPSS/dhf-TZVP-2c.

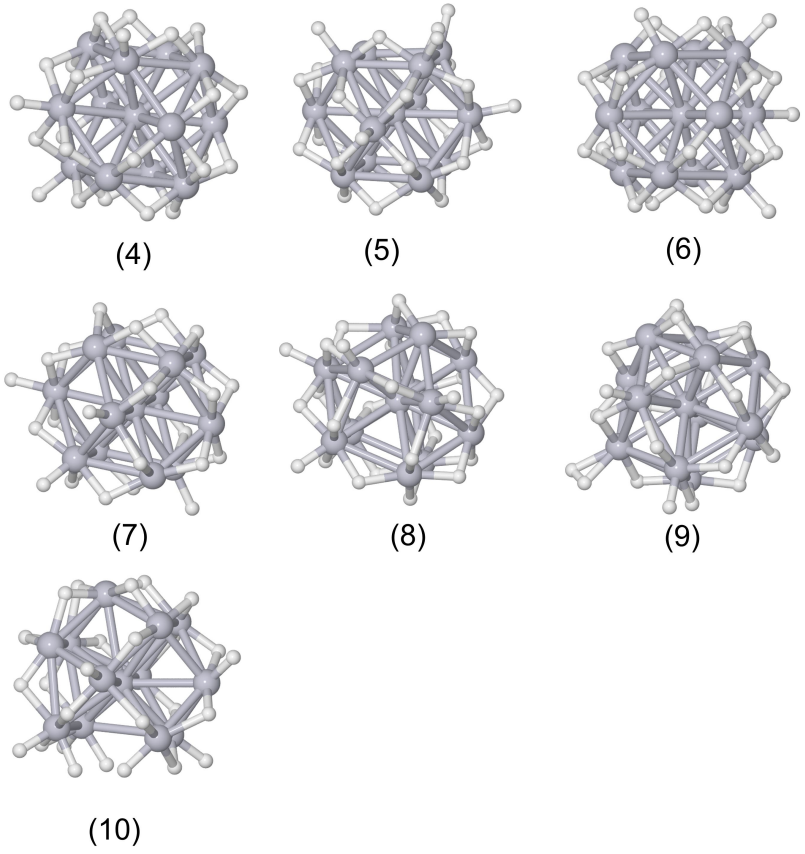

Figure A.1.8.: The higher lying $Pt_{13}D_{26}^-$ isomer **2** optimized using TPSS/dhf-TZVP-2c.

Table A.1.8.: Relative energies (eV) and profile factors (R_w) of $Pt_{13}D_{26}^-$ isomers computed using TPSS/dhf-TZVP-2c.

Isomer	Relative energy (eV)	R_w (%)
1	0	4.5
2	0.42	3.7
3	0.86	6.4
4	0.24	4.5
5	0.5	3.98
6	0.56	4.34
7	0.68	3.93
8	1.04	5.95
9	1.47	6.57
10	2.26	6.13

Table A.1.9.: Relative energies (eV) and profile factors (R_w) of $Pt_{13}D_{25}^-$ **1** isomers computed using TPSS/dhf-TZVP-2c.

Isomer	Relative energy (eV)	R_w (%)
1	0	4.52
1-1	0.32	4.14
1-3	0.34	3.95
1-4	0.46	3.91

A.2. Appendix for Chapter 3.2

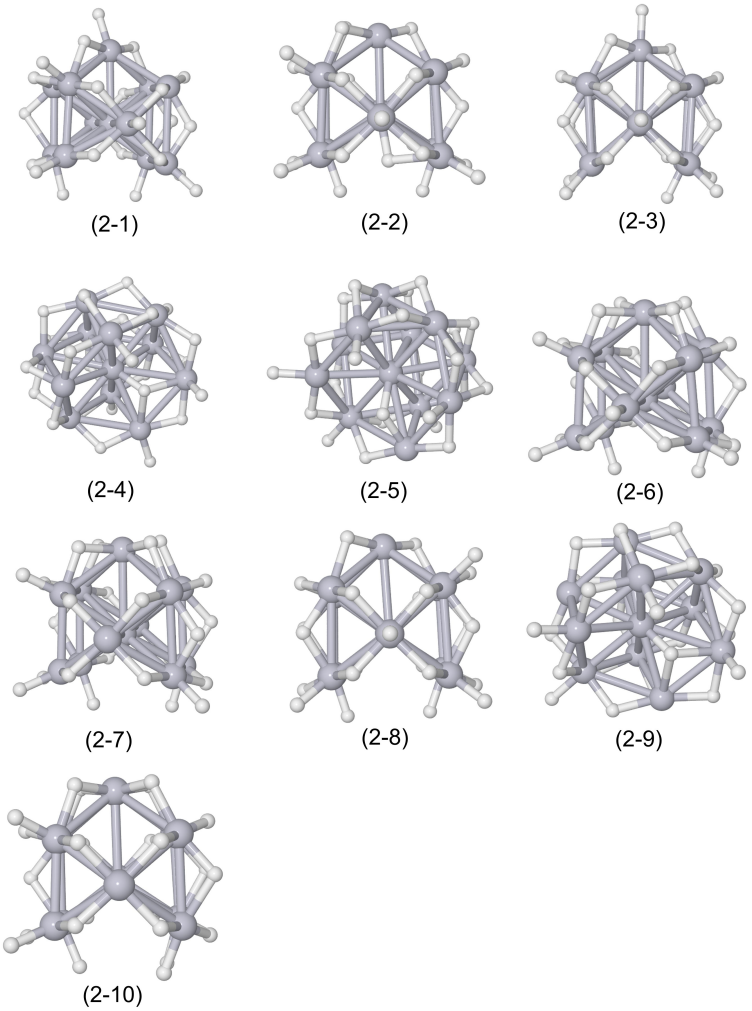

Figure A.2.1.: The higher lying $Pt_{12}D_{24}^-$ isomer **2** optimized using TPSS/dhf-TZVP-2c.

...

Table A.2.1.: Relative electronic energies *E* (TPSS/def2-TZVP) and profile factors (R_w) of the different configurations generated using isomer **2** core structure.(Reproduced under terms of the CC-BY license.[90] (2024), Siddhi Gojare, Dr. Dennis Bumüller, Dr. Stephan Kohaut, Manuel Kraft, Prof.Dr. Ulrich Heiz, Prof.Dr. Manfred M. Kappes, Prof.Dr. Karin Fink, PD Dr. Detlef Schooss, *ChemPhysChem*)

Isomer	E / eV	R_w %
2	0	12
2-1	0.4	12
2-2	0.46	11
2-3	0.54	12
2-4	0.55	10
2-5	0.6	13
2-6	0.6	11
2-7	0.54	13
2-8	0.77	14
2-9	0.54	11

Bibliography

(1) Védrine, J. C. *Chinese Journal of Catalysis* **2019**, *40*, 1627–1636.

(2) Kocemba, I.; Śmiechowicz, I.; Jędrzejczyk, M.; Rogowski, J.; Rynkowski, J. M. *Catalysts* **2021**, *11*, 1475.

(3) Védrine, J. C. *Catalysts* **2017**, *7*, 341.

(4) Ivanova, A.; Slavinskaya, E.; Gulyaev, R.; Zaikovskii, V.; Stonkus, Danilova, I.; Plyasova, L.; Polukhina, I.; Boronin, A. *Applied Catalysis B: Environmental* **2010**, *97*, 57–71.

(5) Alexeev, O. S.; Chin, S. Y.; Engelhard, M. H.; Ortiz-Soto, L.; Amiridis, M. D. *The Journal of Physical Chemistry B* **2005**, *109*, 23430–23443.

(6) Matam, S. K.; Kondratenko, E. V.; Aguirre, M. H.; Hug, P.; Rentsch, D.; Winkler, A.; Weidenkaff, A.; Ferri, D. *Applied Catalysis B: Environmental* **2013**, *129*, 214–224.

(7) Yoo, J. W.; Hathcock, D.; El-Sayed, M. A. *The Journal of Physical Chemistry A* **2002**, *106*, 2049–2054.

(8) Cheng, N.; Stambula, S.; Wang, D.; Banis, M. N.; Liu, J.; Riese, A.; Xiao, B.; Li, R.; Sham, T.-K.; Liu, L.-M., et al. *Nature communications* **2016**, *7*, 13638.

(9) Fryxell, G. E.; Cao, G., *Environmental applications of nanomaterials: synthesis, sorbents and sensors*; Imperial College Press: 2007.

(10) Xie, S.; Zhang, X.; Xu, P.; Hatcher, B.; Liu, Y.; Ma, L.; Ehrlich, S. N.; Hong, S.; Liu, F. *Catalysis Today* **2022**, *402*, 149–160.

(11) Yang, T.; Fukuda, R.; Hosokawa, S.; Tanaka, T.; Sakaki, S.; Ehara, M. *ChemCatChem* **2017**, *9*, 1222–1229.

(12) Henrich, V., *The Surface Science of Metal Oxides*; Cambridge University Press: 1994; Vol. 384.

(13) Thomas, A. C.; Richardson, H. H. *The Journal of Physical Chemistry C* **2008**, *112*, 20033–20037.

(14) Rohmann, C.; Metson, J.; Idriss, H. *Surface science* **2011**, *605*, 1694–1703.

(15) Casarin, M.; Maccato, C.; Vittadini, A. *Inorganic chemistry* **2000**, *39*, 5232–5237.

(16) Kale, M. J.; Christopher, P. *ACS Catalysis* **2016**, *6*, 5599–5609.

(17) Dessal, C.; Len, T.; Morfin, F.; Rousset, J.-L.; Aouine, M.; Afanasiev, P.; Piccolo, L. *ACS Catalysis* **2019**, *9*, 5752–5759.

(18) Wang, Y.; Xiang, B.; Yang, H.-Q.; Hu, C.-W. *ACS omega* **2017**, *2*, 3250–3259.

(19) Sawabe, K.; Satsuma, A. *ACS omega* **2022**, *7*, 4405–4412.

(20) Zhang, R.; Wang, B.; Liu, H.; Ling, L. *The Journal of Physical Chemistry C* **2011**, *115*, 19811–19818.

(21) Yin, S.; Swift, T.; Ge, Q. *Catalysis Today* **2011**, *165*, 10–18.

(22) Zhang, R.; Liu, H.; Wang, B.; Ling, L. *Applied Catalysis B: Environmental* **2012**, *126*, 108–120.

(23) Mager-Maury, C.; Bonnard, G.; Chizallet, C.; Sautet, P.; Raybaud, P. *ChemCatChem* **2011**, *3*, 200–207.

(24) Jensen, F., *Introduction to computational chemistry*; John wiley & sons: 2017.

(25) Atkins, P. W.; Friedman, R. S., *Molecular quantum mechanics*; Oxford university press: 2011.

(26) Møller, C.; Plesset, M. S. *Physical review* **1934**, *46*, 618.

(27) Levine, I. N., *Quantum Chemistry*; PEARSON: 2014.

(28) Koch, W.; Holthausen, M. C., *A chemist's guide to density functional theory*; John Wiley & Sons: 2015.

(29) Hohenberg, P.; Kohn, W. *Physical review* **1964**, *136*, B864.

(30) Kohn, W.; Sham, L. J. *Physical review* **1965**, *140*, A1133.

(31) Perdew, J. P.; Burke, K.; Ernzerhof, M. *Physical review letters* **1996**, *77*, 3865.

(32) Tao, J.; Perdew, J. P.; Staroverov, V. N.; Scuseria, G. E. *Physical review letters* **2003**, *91*, 146401.

(33) Becke, A. D. *The Journal of chemical physics* **1993**, *98*, 1372–1377.

(34) Lee, C.; Yang, W.; Parr, R. G. *Physical review B* **1988**, *37*, 785.

(35) Becke, A. D. *Physical review A* **1988**, *38*, 3098.

(36) Vosko, S.; Wilk, L.; Nusair, M. *J Phys* **1980**, *58*, 1200–1211.

(37) Prasad, R., *Electronic structure of materials*; CRC press: 2013.

(38) Pyykko, P.; Desclaux, J. P. *Accounts of Chemical Research* **1979**, *12*, 276–281.

(39) Wolf, A.; Reiher, M.; Hess, B. A. *The Journal of chemical physics* **2002**, *117*, 9215–9226.

(40) Lenthe, E. v.; Baerends, E.-J.; Snijders, J. G. *The Journal of chemical physics* **1993**, *99*, 4597–4610.

(41) Armbruster, M. K.; Weigend, F.; van Wüllen, C.; Klopper, W. *Physical Chemistry Chemical Physics* **2008**, *10*, 1748–1756.

(42) Evjen, H. *Physical Review* **1932**, *39*, 675.

(43) Rittner, F.; Fink, R.; Boddenberg, B.; Staemmler, V. *Physical Review B* **1998**, *57*, 4160.

(44) Stolarczyk, L. Z.; Piela, L. *International Journal of Quantum Chemistry* **1982**, *22*, 911–927.

(45) Piela, L.; Brédas, J.; André, J. *The Journal of Chemical Physics* **1983**, *78*, 295–300.

(46) Chen, Z.; Wannere, C. S.; Corminboeuf, C.; Puchta, R.; Schleyer, P. v. R. *Chemical reviews* **2005**, *105*, 3842–3888.

(47) Heine, T.; Corminboeuf, C.; Seifert, G. *Chemical reviews* **2005**, *105*, 3889–3910.

(48) Schreckenbach, G.; Ziegler, T. *The Journal of Physical Chemistry* **1995**, *99*, 606–611.

(49) Ditchfield, R. *Molecular Physics* **1974**, *27*, 789–807.

(50) Fernández, I., *Aromaticity: Modern Computational Methods and Applications*; Elsevier: 2021.

(51) Henkelman, G.; Uberuaga, B. P.; Jónsson, H. *The Journal of chemical physics* **2000**, *113*, 9901–9904.

(52) Henkelman, G.; Jónsson, H. *The Journal of chemical physics* **2000**, *113*, 9978–9985.

(53) Jónsson, H.; Mills, G.; Jacobsen, K. W. In *Classical and quantum dynamics in condensed phase simulations*; World Scientific: 1998, pp 385–404.

(54) Sarkar, U.; Blundell, S. *Physical Review B—Condensed Matter and Materials Physics* **2009**, *79*, 125441.

(55) Eberhardt, W. *Surface Science* **2002**, *500*, 242–270.

(56) Liu, Q.; Zhang, Z. *Catalysis Science & Technology* **2019**, *9*, 4821–4834.

(57) Vajda, S.; Pellin, M. J.; Greeley, J. P.; Marshall, C. L.; Curtiss, L. A.; Ballentine, G. A.; Elam, J. W.; Catillon-Mucherie, S.; Redfern, P. C.; Mehmood, F., et al. *Nature materials* **2009**, *8*, 213–216.

(58) Yakovina, O. A.; Lisitsyn, A. S. *Langmuir* **2016**, *32*, 12013–12021.

(59) Carosso, M.; Vottero, E.; Lazzarini, A.; Morandi, S.; Manzoli, M.; Lomachenko, K. A.; Ruiz, M. J.; Pellegrini, R.; Lamberti, C.; Piovano, A., et al. *ACS Catalysis* **2019**, *9*, 7124–7136.

(60) Paz-Borbon, L. O.; Johnston, R.; Barcaro, G.; Fortunelli, A. *The European Physical Journal D* **2009**, *52*, 131–134.

(61) Bus, E.; van Bokhoven, J. A. *Physical Chemistry Chemical Physics* **2007**, *9*, 2894–2902.

(62) Paz-Borbon, L. O.; Johnston, R.; Barcaro, G.; Fortunelli, A. *The European Physical Journal D* **2009**, *52*, 131–134.

(63) Heredia, C. L.; Ferraresi-Curotto, V.; López, M. *Computational materials science* **2012**, *53*, 18–24.

(64) Bumüller, D.; Yohannes, A. G.; Kohaut, S.; Kondov, I.; Kappes, M. M.; Fink, K.; Schooss, D. *The Journal of Physical Chemistry A* **2022**, *126*, 3502–3510.

(65) Imaoka, T.; Kitazawa, H.; Chun, W.-J.; Omura, S.; Albrecht, K.; Yamamoto, K. *Journal of the American Chemical Society* **2013**, *135*, 13089–13095.

(66) Häkkinen, H.; Manninen, M. *Physical review letters* **1996**, *76*, 1599.

(67) Brack, M. *Scientific American* **1997**, *277*, 50–55.

(68) Li, H.; Li, L.; Pedersen, A.; Gao, Y.; Khetrapal, N.; Jónsson, H.; Zeng, X. C. *Nano letters* **2015**, *15*, 682–688.

(69) Sachdev, A.; Masel, R.; Adams, J. *Journal of Catalysis* **1992**, *136*, 320–333.

(70) Ma, Q.; Zhu, H.; Liu, D.; Li, R.; Li, T.; Ren, H.; Zhao, W.; Pan, Y.; Liu, Y.; Guo, W. *Catalysis Science & Technology* **2023**, *13*, 2080–2091.

(71) Wandelt, K., *Encyclopedia of interfacial chemistry: surface science and electrochemistry*; Elsevier: 2018.

(72) Prince, E.; Wilson, A., *International tables for crystallography. Volume C: mathematical, physical and chemical tables*; Wiley Online Library: 1999.

(73) Weast, R. C. **1986**.

(74) Schooss, D.; Blom, M. N.; Parks, J. H.; Issendorff, B. v.; Haberland, H.; Kappes, M. M. *Nano letters* **2005**, *5*, 1972–1977.

(75) Doye, J. P.; Wales, D. J.; Berry, R. S. *The Journal of chemical physics* **1995**, *103*, 4234–4249.

(76) Cleri, F.; Rosato, V. *Physical Review B* **1993**, *48*, 22.

(77) Gupta, R. P. *Physical Review B* **1981**, *23*, 6265.

(78) Neiss, C.; Schooss, D. *Chemical Physics Letters* **2012**, *532*, 119–123.

(79) Rapps, T.; Ahlrichs, R.; Waldt, E.; Kappes, M. M.; Schooss, D. *Angewandte Chemie International Edition* **2013**, *52*.

(80) Balasubramani, S. G.; Chen, G. P.; Coriani, S.; Diedenhofen, M.; Frank, M. S.; Franzke, Y. J.; Furche, F.; Grotjahn, R.; Harding, M. E.; Hättig, C., et al. *The Journal of chemical physics* **2020**, *152*.

(81) TURBOMOLE V7.7 2022, a development of University of Karlsruhe and Forschungszentrum Karlsruhe GmbH, 1989-2007, TURBOMOLE GmbH, since 2007; available from `https://www.turbomole.org`.

(82) Eichkorn, K.; Treutler, O.; Öhm, H.; Häser, M.; Ahlrichs, R. *Chemical physics letters* **1995**, *240*, 283–290.

(83) Eichkorn, K.; Weigend, F.; Treutler, O.; Ahlrichs, R. *Theoretical Chemistry Accounts* **1997**, *97*, 119–124.

(84) Weigend, F.; Ahlrichs, R. *Physical Chemistry Chemical Physics* **2005**, *7*, 3297–3305.

(85) Andrae, D.; Haeussermann, U.; Dolg, M.; Stoll, H.; Preuss, H. *Theoretica chimica acta* **1990**, *77*, 123–141.

(86) Grimme, S.; Ehrlich, S.; Goerigk, L. *Journal of computational chemistry* **2011**, *32*, 1456–1465.

(87) Johansson, M. P.; Lechtken, A.; Schooss, D.; Kappes, M. M.; Furche, F. *Physical Review A—Atomic, Molecular, and Optical Physics* **2008**, *77*, 053202.

(88) Kelting, R.; Baldes, A.; Schwarz, U.; Rapps, T.; Schooss, D.; Weis, P.; Neiss, C.; Weigend, F.; Kappes, M. M. *The Journal of Chemical Physics* **2012**, *136*.

(89) Weigend, F.; Baldes, A. *The Journal of chemical physics* **2010**, *133*.

(90) Gojare, S.; Bumüller, D.; Kohaut, S.; Kraft, M.; Heiz, U.; Kappes, M. M.; Fink, K.; Schooss, D. *ChemPhysChem* **2024**, e202400649.

(91) Reed, A. E.; Weinstock, R. B.; Weinhold, F. *The Journal of chemical physics* **1985**, *83*, 735–746.

(92) Wiberg, K. B. *Tetrahedron* **1968**, *24*, 1083–1096.

(93) Schleyer, P. v. R.; Maerker, C.; Dransfeld, A.; Jiao, H.; van Eikema Hommes, N. J. *Journal of the American Chemical Society* **1996**, *118*, 6317–6318.

(94) Huang, W.; Ji, M.; Dong, C.-D.; Gu, X.; Wang, L.-M.; Gong, X. G.; Wang, L.-S. *Acs Nano* **2008**, *2*, 897–904.

(95) Moreno, N.; Ferraro, F.; Flórez, E.; Hadad, C.; Restrepo, A. *The Journal of Physical Chemistry A* **2016**, *120*, 1698–1705.

(96) Shi, Q.; Sun, R. *Computational and Theoretical Chemistry* **2017**, *1106*, 43–49.

(97) Hammer, B.; Nørskov, J. K. *Surface science* **1995**, *343*, 211–220.

(98) De Heer, W. A. *Reviews of Modern Physics* **1993**, *65*, 611.

(99) Cricchio, D.; Fiordilino, E.; Persico, F. *Physical Review A—Atomic, Molecular, and Optical Physics* **2012**, *86*, 013201.

(100) Zhang, X.; Cui, Y.; Hong, L. *Journal of Computational and Theoretical Nanoscience* **2009**, *6*, 640–643.

(101) Boldyrev, A. I.; Wang, L.-S. *Chemical reviews* **2005**, *105*, 3716–3757.

(102) Lyubovsky, M.; Pfefferle, L. *Catalysis Today* **1999**, *47*, 29–44.

(103) Minahan, D. M.; Hoflund, G. B.; Epling, W. S.; Schoenfeld, D. W. *Journal of catalysis* **1997**, *168*, 393–399.

(104) Moreno, M.; Wang, F.; Malac, M.; Kasama, T.; Gigola, C. E.; Costilla, I.; Sánchez, M. *Journal of Applied Physics* **2009**, *105*.

(105) Jung, S. Y.; Lee, S. J.; Park, J. J.; Lee, S. C.; Jun, H. K.; Lee, T. J.; Ryu, C. K.; Kim, J. C. *Separation and purification technology* **2008**, *63*, 297–302.

(106) Li, Q.; Sui, Z.; Zhou, X.; Chen, D. *Applied Catalysis A: General* **2011**, *398*, 18–26.

(107) Morterra, C.; Magnacca, G. *Catalysis Today* **1996**, *27*, 497–532.

(108) Ahn, J.; Rabalais, J. *Surface Science* **1997**, *388*, 121–131.

(109) Puchin, V.; Gale, J.; Shluger, A.; Kotomin, E.; Günster, J.; Brause, M.; Kempter, V. *Surface science* **1997**, *370*, 190–200.

(110) Manassidis, I.; Gillan, M. J. *Journal of the American Ceramic Society* **1994**, *77*, 335–338.

(111) Blonski, S.; Garofalini, S. *Surface Science* **1993**, *295*, 263–274.

(112) Ranea, V. A.; Schneider, W. F.; Carmichael, I. *Surface science* **2008**, *602*, 268–275.

(113) McHale, J.; Auroux, A.; Perrotta, A.; Navrotsky, A. *Science* **1997**, *277*, 788–791.

(114) Hass, K.; Schneider, W.; Curioni, A.; Andreoni, W. *The Journal of Physical Chemistry B* **2000**, *104*, 5527–5540.

(115) Rohmann, C.; Metson, J.; Idriss, H. *Physical Chemistry Chemical Physics* **2014**, *16*, 14287–14297.

(116) Alavi, S.; Sorescu, D. C.; Thompson, D. L. *The Journal of Physical Chemistry B* **2003**, *107*, 186–195.

(117) Casarin, M.; Falcomer, D.; Glisenti, A.; Vittadini, A. *Inorganic chemistry* **2003**, *42*, 436–445.

(118) Shapovalov, V.; Truong, T. N. *The Journal of Physical Chemistry B* **2000**, *104*, 9859–9863.

(119) Borck, Ø.; Schröder, E. *Journal of Physics: Condensed Matter* **2005**, *18*, 1.

(120) Chiavassa, D. L.; Barrandeguy, J.; Bonivardi, A. L.; Baltanás, M. A. *Catalysis Today* **2008**, *133*, 780–786.

(121) Yu, K.-P.; Yu, W.-Y.; Kuo, M.-C.; Liou, Y.-C.; Chien, S.-H. *Applied Catalysis B: Environmental* **2008**, *84*, 112–118.

(122) Freund, H.-J.; Roberts, M. W. *Surface Science Reports* **1996**, *25*, 225–273.

(123) Baltrusaitis, J.; Jensen, J. H.; Grassian, V. H. *The Journal of Physical Chemistry B* **2006**, *110*, 12005–12016.

(124) Liu, S.; Zhou, Z.; Chen, J.; Fu, Y.; Cai, C. *Applied Surface Science* **2023**, *611*, 155645.

(125) Alioui, O.; Gueddida, S.; Benguerba, Y.; Lebègue, S.; Badawi, M. *Applied Surface Science* **2023**, *610*, 155474.

(126) Ghosh, T. K.; Nair, N. N. *ChemCatChem* **2013**, *5*, 1811–1821.

(127) Liu, J.; Bunes, B. R.; Zang, L.; Wang, C. *Environmental Chemistry Letters* **2018**, *16*, 477–505.

(128) Tan, K.; Dixit, M.; Dean, J.; Mpourmpakis, G. *Industrial & Engineering Chemistry Research* **2019**, *58*, 20236–20246.

(129) Sensoy, M. G.; Ustunel, H.; Toffoli, D. *Applied Surface Science* **2020**, *499*, 143968.

(130) Lee, J.; Jang, E. J.; Oh, D. G.; Szanyi, J.; Kwak, J. H. *Journal of catalysis* **2020**, *385*, 204–212.

(131) Lou, Y.; Liu, J. *Industrial & Engineering Chemistry Research* **2017**, *56*, 6916–6925.

(132) Zhang, L.; Ren, Y.; Liu, W.; Wang, A.; Zhang, T. *National Science Review* **2018**, *5*, 653–672.

(133) Yan, H.; Cheng, H.; Yi, H.; Lin, Y.; Yao, T.; Wang, C.; Li, J.; Wei, S.; Lu, J. *Journal of the American chemical society* **2015**, *137*, 10484–10487.

(134) Qiao, B.; Liang, J.-X.; Wang, A.; Xu, C.-Q.; Li, J.; Zhang, T.; Liu, J. J. *Nano Research* **2015**, *8*, 2913–2924.

(135) Wang, X.; Zhou, H.; Zhang, X.; Jia, J.; Wu, H. *Applied Surface Science* **2018**, *433*, 60–65.

(136) Pašti, I. A.; Johansson, B.; Skorodumova, N. V. *Physical Chemistry Chemical Physics* **2018**, *20*, 6337–6346.

(137) Neyman, K.; Inntam, C.; Nasluzov, V.; Kosarev, R.; Rösch, N. *Applied Physics A* **2004**, *78*, 823–828.

(138) Rivanenkov, V. V.; Nasluzov, V. A.; Shor, A. M.; Neyman, K. M.; Rösch, N. *Surface science* **2003**, *525*, 173–183.

(139) Yourdshahyan, Y.; Cooper, V. R.; Kolpak, A. M.; Rappe, A. M. In *Physical Chemistry of Interfaces and Nanomaterials II*, 2003; Vol. 5223, pp 223–231.

(140) Nasluzov, V. A.; Rivanenkov, V. V.; Shor, A. M.; Neyman, K. M.; Rösch, N. *Chemical physics letters* **2003**, *374*, 487–495.

(141) He, X.; He, Q.; Deng, Y.; Peng, M.; Chen, H.; Zhang, Y.; Yao, S.; Zhang, M.; Xiao, D.; Ma, D., et al. *Nature communications* **2019**, *10*, 3663.

(142) Nakaya, Y.; Hirayama, J.; Yamazoe, S.; Shimizu, K.-i.; Furukawa, S. *Nature communications* **2020**, *11*, 2838.

(143) Zhang, N.; Ye, C.; Yan, H.; Li, L.; He, H.; Wang, D.; Li, Y. *Nano Research* **2020**, *13*, 3165–3182.

(144) Chen, L.-N.; Hou, K.-P.; Liu, Y.-S.; Qi, Z.-Y.; Zheng, Q.; Lu, Y.-H.; Chen, J.-Y.; Chen, J.-L.; Pao, C.-W.; Wang, S.-B., et al. *Journal of the American Chemical Society* **2019**, *141*, 17995–17999.

(145) Zhang, Z.; He, G.; Li, Y.; Zhang, C.; Ma, J.; He, H. *Environmental Science & Technology* **2022**, *56*, 10916–10924.

(146) Heiden, S.; Usvyat, D.; Saalfrank, P. *The Journal of Physical Chemistry C* **2019**, *123*, 6675–6684.

(147) Chen, J.; Sharapa, D.; Plessow, P. N. *Phys. Rev. Res.* **2022**, *4*, 013232.

(148) Fink, K. *Physical Chemistry Chemical Physics* **2006**, *8*, 1482–1489.

(149) Adamo, C.; Barone, V. *The Journal of chemical physics* **1999**, *110*, 6158–6170.

(150) Caldeweyher, E.; Ehlert, S.; Hansen, A.; Neugebauer, H.; Spicher, S.; Bannwarth, C.; Grimme, S. *The Journal of chemical physics* **2019**, *150*.

(151) Willard R. Wadt, P. J. H. *J. Chem. Phys.* **1985**, *82*, 284–298.

(152) Boys, S. F.; Bernardi, F. *Molecular physics* **1970**, *19*, 553–566.

(153) Huber, K.-P. *Molecular spectra and molecular structure* **1979**, *4*, 146–291.

(154) Gojare, S.; Chen, S.; Chen, J.; Yu, Z.; Vázquez Quesada, J.; Pleßow, P. N.; Fink, K.; Wang, Y. *ChemPhysChem* **2025**, *26*, e202401134.

(155) Grabowski, S. J., *Understanding hydrogen bonds: theoretical and experimental views*; Royal Society of Chemistry: 2020.

(156) Gojare, S.; Chen, S.; Chen, J.; Yu, Z.; Vazquez Quesada, J.; Pleßow, P.; Fink, K.; Wang, Y. *ChemPhysChem* **2025**, *n/a*, e202401134.

(157) Dononelli, W.; Klüner, T. *International Journal of Quantum Chemistry* **2021**, *121*, e26428.

(158) Pan, Y.; Liu, C.-j.; Ge, Q. *Langmuir* **2008**, *24*, 12410–12419.

(159) Eng, P. J.; Trainor, T. P.; Brown Jr, G. E.; Waychunas, G. A.; Newville, M.; Sutton, S. R.; Rivers, M. L. *Science* **2000**, *288*, 1029–1033.

(160) Deskins, N. A.; Mei, D.; Dupuis, M. *Surface science* **2009**, *603*, 2793–2807.

(161) Gao, H. *Applied Surface Science* **2016**, *379*, 347–357.

(162) Corral Valero, M.; Raybaud, P.; Sautet, P. *The Journal of Physical Chemistry B* **2006**, *110*, 1759–1767.

(163) Wang, J.; Wang, C.; Chen, X.; Liu, X.; Li, Y.; Shan, W.; He, H. *Applied Catalysis B: Environment and Energy* **2024**, *357*, 124342.

(164) Li, J.; Zhang, R.; Wang, B. *Applied surface science* **2013**, *270*, 728–736.

(165) Blyholder, G. *The Journal of Physical Chemistry* **1964**, *68*, 2772–2777.

(166) Morfin, F.; Dessal, C.; Sangnier, A.; Chizallet, C.; Piccolo, L. *ACS Catalysis* **2024**, *14*, 9628–9639.

(167) Anderson, J. A.; Rochester, C. H. *Journal of the Chemical Society, Faraday Transactions* **1991**, *87*, 1479–1483.

(168) Qiao, B.; Wang, A.; Yang, X.; Allard, L. F.; Jiang, Z.; Cui, Y.; Liu, J.; Li, J.; Zhang, T. *Nature chemistry* **2011**, *3*, 634–641.

(169) Gomes, J. R.; Illas, F.; Hernández, N. C.; Sanz, J. F.; Wander, A.; Harrison, N. M. *The Journal of chemical physics* **2002**, *116*, 1684–1691.

(170) Gomes, J. R.; Illas, F.; Hernández, N. C.; Márquez, A.; Sanz, J. *Physical Review B* **2002**, *65*, 125414.

Acronyms and Abbreviations

2C-DFT Two-component Density Functional Theory

BE Binding energy

BSSE Basis set superposition error

CN Coordination number

CT Charge transfer

DFT Density Functional Theory

DKH Douglass-Kroll-Hess

DOS Density of states

ECP Effective core potential

FWHM Full width half maximum

GGA Generalized gradient approximation

HF Hartree-Fock theory

HOMO Highest Occupied Molecular Orbital

IRRAS Infrared reflection absorption spectroscopy

KS Kohn Sham

LDA Local density approximation

LSDA Local spin density approximation

LUMO Lowest Occupied Molecular Orbital

MEP Minimum energy path

MO Molecular orbital

MP2 Møller-Plesset Perturbation theory

MSI Metal support interaction

NEB Nudged elastic band method

NICS Nuclear Independent Chemical Shift

pbp pentagonal bipyramid

PCF Point charge field

QC Quantum cluster

SAC Single atom catalyst

SO Spin-orbit

SOC Spin-orbit coupling

TIED Trapped ion electron diffraction

XC Exchange correlation

XPS X-ray photoelectron spectroscopy

ZORA Zeroth-order regular approximation

Permissions to Print

This work contains material adapted from work previously published in scientific journals. Permissions for reuse or reprint of the relevant content has been requested to the copyright owner.

- Chapter 3.2: Partially adapted from *$Pt_{12}H_{24}^{-}$:A Cuboctahedral Platinum Hydride Cluster Cage* Siddhi Gojare, Dennis Bumüller, Stephan Kohaut, Manuel Kraft, Ulrich Heiz,Manfred M. Kappes, Karin Fink, and Detlef Schooss, *ChemPhysChem* **25**, e202400649, (2024). The Authors. Wiley Online Library.
- Chapter 4.1: Partially adapted from *Adsorption of CO on αAl_2O_3 (0001): A combined experimental and computational study* Siddhi Gojare, Shuang Chen, Jiachen Chen, Zairan Yu, Juana Vazquez Quesada, Philipp N. Pleßow, Karin Fink, and Yuemin Wang, *ChemPhysChem* 26. 10, e202401134, (2025). Wiley Online Library.

List of Publications

- *$Pt_{12}H_{24}^-$:A Cuboctahedral Platinum Hydride Cluster Cage*, Siddhi Gojare, Dennis Bumüller, Stephan Kohaut, Manuel Kraft, Ulrich Heiz,Manfred M. Kappes, Karin Fink, and Detlef Schooss, *ChemPhysChem*, **25**(23), e202400649, (2024)
- *Adsorption of CO on α-Al_2O_3(0001): A combined experimental and computational study*, Siddhi Gojare, Shuang Chen, Jiachen Chen, Zairan Yu, Juana Vazquez Quesada, Philipp N. Pleßow, Karin Fink, and Yuemin Wang, *ChemPhysChem*, **26**(10), e202401134, (2025)
- *The Structures of Platinum Cluster Hydrides $Pt_nD_{2n}^-$*, Dennis Bumüller, Siddhi Gojare, Stephan Kohaut, Manuel Kraft, Manfred M.Kappes, Karin Fink, and Detlef Schooss, -In preparation
- *Adsorption of CO_2 on α-Al_2O_3(0001): A combined experimental and computational study*- In preparation

Acknowledgments

It has been a wonderful three years of research. It would not be possible without the immense support of numerous people to whom I would like to express my gratitude.

First of all, I would like to thank my supervisor and mentor, Prof. Karin Fink, for allowing me to complete my doctoral thesis in her group. I have always found the atmosphere in Prof. Fink's group very conducive to my scientific work. She has always been supportive all through my PhD journey and also in life as a whole. Her knowledge, motivation, encouragement, and passion for science have always been an inspiration to me. Thank you for being patient while I made a lot of mistakes. Special thanks to my co-supervisor Prof. Felix Studt for giving fruitful advices as a mentor and for the useful discussions.

I express my gratitude to Dr.Juana Vázquez Quesada for her support, scientific contribution, and feedback during my doctoral journey. She has always been a fun office mate and an inspiration for me.

I am grateful for being a part of Prof. Klopper's group and discuss various scientific topics in group seminars. Many thanks to all the former and present group members from Campus North and south for the fruitful discussions, and fun time together. I would like to thank Christian Pachl, Constantin Weeber, and Dr.Juana Vázquez Quesada for proofreading my thesis.

I would like to thank my collaborators Dr. Detlef Schooss, Dr. Yuemin Wang, and Dr. Philipp Plessow and their group members from KIT for bringing interesting scientific projects and bringing in new insights. I enjoyed the discussion of every scientific aspect of all the topics with the members.

I am thankful for the financial support provided by SFB 1441-TrackAct for my scientific work. I am also grateful for being an associate of GRK 2450 which allowed me to attend various personal development courses. They were quite helpful to me. Also, the scientific discussions taking place at every annual meetup were quite helpful for me.

Lastly, I would like to thank my parents and all my family members for always being supportive in all my life decisions. They have always been my inspiration and a role model. Special thanks to my in-laws who have always been caring, and encouraging. Last but not least, my husband who has seen all my ups and downs. Without his patience and support, I would not have completed this thesis.

Declaration

I, Siddhi Gojare declare that I have developed and written the enclosed thesis completely by myself. I have used the Deepl tool to translate the abstract into German. I have marked all the parts of the thesis that I have included from referenced literature, either in their original wording or paraphrasing their contents. I have followed the by-laws to implement scientific integrity at KIT.